THE UNIVERSITY of ADELAIDE

Nondestructive Testing and Structural Health Monitoring Techniques for Damage Detection of Cement-based Materials

Tingyuan Yin

A thesis submitted in fulfilment of the requirement for the degree of Doctor of Philosophy

School of Civil, Environmental & Mining Engineering
The University of Adelaide
Australia

July 2022

Table of Contents

Declaration

I, Tingyuan Yin, certify that this work contains no material which has been accepted for the award of any other degree or diploma in my name, in any university or other tertiary institution and, to the best of my knowledge and belief, contains no material previously published or written by another person, except where due reference has been made in the text. In addition, I certify that no part of this work will, in the future, be used in a submission in my name, for any other degree or diploma in any university or other tertiary institution without the prior approval of the University of Adelaide and where applicable, any partner institution responsible for the joint-award of this degree.

I acknowledge that the copyright of published works contained within this thesis resides with the copyright holder(s) of those works.

I also give permission for the digital version of my thesis to be made available on the web, via the University's digital research repository, the Library Search and also through web search engines, unless permission has been granted by the University to restrict access for a period of time.

Date: 06 July 2022

Acknowledgments

To my dear Motherland

I would like to thank Prof. Alex Ching-Tai Ng and Prof. Andrei Georgievich Kotousov, who are my supervisor and co-supervisor, respectively, for their mentoring. Particularly, I want to show my deepest appreciation to Alex, who gave me great encouragement and support during a special difficult period in my life.

Gratefulness is also given to my colleagues. They are Carmen Yeung, James David Vidler, James Martin Hughes, Juan Carlos Pineda Allen, Xianwen Hu, Ahmed Aseem, Jinhang Wu, Hankai Zhu, Zijie Zeng, Jiang Chang, Min Gao, Yuqiao Cao, and Tianyi Wang. They helped me with my experimental and theoretical work.

I would also like to express my gratitude to technicians, Jon Ayoub, Simon Golding, Gary Bowman, Ian Ogier, Brenton Howie, Mark Peacock, Tom Wilson, Thomas Stanef, and Philip Schmidt. They are a group of talented and hard-working people who are experts in IT, carpentry, electronics, and civil engineering. Without their help, I would not have completed my PhD project in a smooth way.

In addition, I'm happy to join the PGL committee to be the HDR representative to contribute to the HDR community and to organize morning tea and annual conference to provide opportunities for HDR and academics to communicate more. Thank Prof. Nigel Cook and Associate Prof. Giang Nguyen, who gave me good advice and strong support every time when I worked for PGL.

I also would like to show my thanks to my friends. They are Sirui Chen, Yimin Fan, Feng tang, Xiaoyang Yin, Juan Chen, Yueming Tong, Ziqi Zhang and Yang Liu.

Special mention goes to a special member, my son, Cat Cement. Before I had Cement, I had never known how happy to have a handsome, smart, and cute cat. I would like to thank my beloved family, my father, my mother, and my grandmother. In particular, my grandfather, Mr. Guoxiong Yin, is the most gentle and patient grandpa in the world in my heart. When I was growing up, whenever I encountered difficulties, I would think of the warm time with my grandpa, which helped me come over the tough time. He has gone, but I miss him every moment, every day. I know he will eventually come into my dream and tell me that he is proud of me.

Finally, I acknowledge the support I have received for my research through the provision of China Scholarship Council (CSC) scholarship.

List of Publications

Journal Articles

1. **Yin, T**., Ng, C.T., and Kotousov, A., 2021. Damage detection of ultra-high-performance fibre-reinforced concrete using a harmonic wave modulation technique. *Construction and Building Materials*, *313*, p.125306.
2. **Yin, T**., Ng, C.T., Vidler, J., Ho, V.D. and Kotousov, A., 2022. Amplitude-Modulation Vibro-Acoustic Technique for Damage Evaluation. *Structural Health Monitoring*, p.14759217221106209.
3. **Yin, T**., Ng, C.T., Vidler, J., Ho, V.D. and Kotousov, A., Characterization of Thermal Damage in Graphene Mortar Materials Using High-order Sideband Generation of Amplitude-modulation Vibro-acoustic Technique. *Mechanical Systems and Signal Processing*. Accepted.

The following papers have arisen from this research but are not included as main chapters of the thesis.

Conference Proceedings

4. **Yin, T**., Ng, C.T. and Kotousov, A., 2021, January. Thermal damage detection and monitoring of pristine graphene mortar materials using a cross-modulation vibro-acoustic technique. In *ACAM10: 10th Australasian Congress on Applied Mechanics: 10th Australasian Congress on Applied Mechanics* (pp. 177-183). Engineers Australia.

Journal Articles

5. **Yin, T.,** Sepulveda, B., Ng, C.T., Visintin, P., and Kotousov, A., In-situ nonlinear ultrasonic technique for monitoring damage in ultra-high performance fibre reinforce concrete (UHPFRC) during direct tensile test. To be submitted.
6. Hu, X., **Yin, T.**, Zhu, H., Ng, C.T. and Kotousov, A., 2022. Structural health monitoring of partially immersed metallic plates using nonlinear guided wave mixing. *Construction and Building Materials*, 346, p.128381.
7. Ng, C.T., Yeung, C., **Yin, T.**, Chen L., 2022. Stress evaluation of tubular structures using torsional guided wave mixing. Special Issue in *Smart Structures and Systems*, Vol.30, No.6, p.639-648.
8. Ng, C.T., Yeung, C., **Yin, T.**, He, Y. and Chen, L., 2022. Investigation of nonlinear torsional guided wave mixing in pipes buried in soil. *Engineering Structures*, 273, p.115089.

Abstract

This thesis contains theoretical and experimental studies of non-destructive testing (NDT) and structural health monitoring (SHM) techniques for damage detection of cement-based materials. New nonlinear vibro-acoustic techniques are proposed in the study for the purposes of 1) to overcome application restriction of vibro-acoustic technique (e.g., limited frequency range of signal emitter and high power consumption for long-term monitoring), and 2) to develop a better understanding of amplitude-modulated signals propagating through medium with material nonlinearity and contact nonlinearity, and 3) to establish feasible nonlinear parameter to quantitatively assess different levels of damage in cement-based materials.

In Chapter 1, an overview of the existing vibro-acoustic technique for damage detection on cement-based materials is provided to shed light on the significance of this work. Chapter 2 introduces the previous research on SHM and NDT technique and theoretical models with material nonlinearity and contact nonlinearity.

In Chapter 3, the cross-modulated vibro-acoustic (CMVA) technique is proposed to detect damages caused by flexural tests in ultra-high-performance fibre-reinforced concrete (UHP-FRC) material. This study is a preliminary exploration of applying amplitude-modulated signals to the vibro-acoustic technique. A theoretical model is established to describe amplitude-modulated low-frequency pump wave and high-frequency probe wave propagating through the medium with concentrated crack, which can be seen as the source of contact nonlinearity.

In Chapter 4, three amplitude-modulated approaches: 1) the pure amplitude-modulated (PAM) method, 2) the suppressive amplitude-modulated (SAM) method and 3) the transmitted amplitude-modulated (TAM) method, are utilized in the low-frequency excitation in the vibro-

acoustic (VA) technique to track the evolution of thermal damage in pristine graphene (PRG) mortar. Furthermore, the nonlinear parameters of these three approaches are built through building a theoretical model with material nonlinearity, where analytical solutions of nonlinear displacement of waves are obtained by solving the wave equation with second-order nonlinear terms. It is the first time that three amplitude-modulated vibro-acoustic approaches are proposed and compared from the aspects of sideband generation, power consumption, and sensitivity to damages.

In Chapter 5, the application of amplitude-modulated vibro-acoustic technique is extended to distinguish the different dosages of PRG mortar. Additionally, by solving the wave equation with second- and third-order nonlinear terms, it can be found that second- and third-order terms and higher-order perturbation assumptions are necessary to obtain more comprehensive analytical solutions of displacement of waves with three frequencies. To conclude from the study in Chapter 3 to 5, the amplitude-modulated vibro-acoustic technique can overcome the limitations of the conventional vibro-acoustic technique and be more practical, efficient, and power-saving. In addition, the proposed vibro-acoustic approaches are sensitive to the damages, particularly in the early damage state.

Chapter 6 summarizes the major contribution of this thesis and suggestions for future works.

List of Abbreviations and Variables

The following table describes the significance of various abbreviations and variables used throughout the thesis.

Abbreviation	Meaning	Page
AMVA	amplitude-modulation vibro-acoustic	21
ASR	alkali-silica reaction	15
CMVA	cross-modulated vibro-acoustic	4
FANSIRAS	flipped accumulative nonlinear single impact acoustic spectroscopy	17
FFT	fast Fourier transform	53
FSS	sideband spectrogram	20
HF	high-frequency	1
IM	impact-modulation	2
LF	low-frequency	1
LRS	linear response subtraction	20
MPE	multiscale permutation entropy	20
NDT	non-destructive testing	1
NIRAS	nonlinear impact resonance acoustic spectroscopy	15
OPC	ordinary portland cement	90
PAM	pure amplitude-modulated	21
RF	resonant frequency	35
PR	point receiver	8
PRG	pristine graphene	4
PS	point source	8
SAM	suppressive amplitude-modulated	4
SD	synchronous demodulation	20
SHM	structural health monitoring	1

SNR	signal-to-noise ratio	20
SPC	sideband peak count	20
TAM	transmitted amplitude-modulated	21
TR	time reversal	20
UHP-FRC	ultra-high-performance fibre-reinforced concrete	4
UPV	ultrasonic pulse velocity	7
VA	vibro-acoustic	5
VM	vibro-modulation	2

Variables	**Meaning**	**Page**
f	frequency	14
Δf	frequency resolution	51
f_l	fundamental longitudinal frequency	56
f_L	low frequency	2
f_{L1}	low frequency used in AMVA technique ($f_{L1} < f_{L2}$)	40
f_{L2}	low frequency used in AMVA technique ($f_{L1} < f_{L2}$)	40
f_H	high frequency	2
f_s	sampling frequency	51
t	time	10
u_i	displacement of particle	10
u_2	secondary displacement field	87
u_3	third-order displacement field	135
U_{Inc}	displacement of incident waves	12
u_I	displacement of incident waves	41
U_{Tra}	displacement of transmitted wave	12
u_T	displacement of transmitted wave	41

U_{Ref}	displacement of reflective wave	12
u_R	displacement of reflective wave	41
u_1^P	primary field of pam	87
u_1^S	primary field of sam	87
u_1^T	primary field of tam	87
x_i	cartesian coordinate	10
ρ_0	constant mass density in the undeformed material state	10
C_{ijkl}	second-order elastic stiffness	10
C_{ijklmn}	third-order elastic stiffness	10
$C_{ijklmnpq}$	fourth-order elastic stiffness	10
F	external force	12
d	relative displacement of crack	12
d_0	initial crack	12
$\boldsymbol{T}$	external stress	12
T	traction stress	12
T_0	initial traction stress	12
σ	stress	12
σ_b	stress of uhp-frc specimen in flexural test	48
σ_w	stress of incident waves	12
$\boldsymbol{n}$	normal unit vector	12
K_1	first-order stiffness	12
K_2	second-order stiffness	12
ξ	variable	137
$\xi(t)$	dynamic opening displacement of crack	12
α	nonlinear parameter	86
α_P	nonlinear parameter of PAM method	89
α_S	nonlinear parameter of SAM method	90

α_T	nonlinear parameter of TAM method	90
β	second-order nonlinear parameter	15
β'	nonlinear parameter after heating treatments	159
β^0	nonlinear parameter at intact state	159
$\beta^{(2)}$	nonlinear parameter based on the second-order effect	138
$\beta^{(2+3)}$	nonlinear parameter based on the second-order and third-order effect	138
γ	third-order nonlinear parameter	15
D_α	nonlinear parameter	35
A	amplitude of wave	42
$\mathrm{A_D}$	amplitude of dominant pump frequency	98
A_H	amplitude of HF probe wave	53
A_{L2}	amplitude of LF at f_{L2} of pump wave	53
A_s	amplitude of sideband	53
$A_s^{(\omega_H \pm \omega_{L1})}$	amplitude of sidebands at $(\omega_H \pm \omega_{L1})$	139
$A_s^{(\omega_H \pm 2\omega_{L1})}$	amplitude of sidebands at $(\omega_H \pm 2\omega_{L1})$	139
$A_s^{(\omega_H \pm \omega_{L2})}$	amplitude of sidebands at $(\omega_H \pm \omega_{L2})$	138
$A_s^{(\omega_H \pm 2\omega_{L2})}$	amplitude of sidebands at $(\omega_H \pm 2\omega_{L2})$	139
$A_s^{(\omega_H \pm \omega_{L2} \pm \omega_{L1})}$	amplitude of sidebands at $(\omega_H \pm \omega_{L2} \pm \omega_{L1})$	138
$A_s^{(\omega_H \pm 2\omega_{L2} \pm \omega_{L1})}$	amplitude of sidebands at $(\omega_H \pm 2\omega_{L2} \pm \omega_{L1})$	139
$A_s^{(\omega_H \pm 2\omega_{L2} \pm 2\omega_{L1})}$	amplitude of sidebands at $(\omega_H \pm 2\omega_{L2} \pm 2\omega_{L1})$	139
ω	angular frequency	42
ω_{H}	angular frequency of f_H	87
ω_{L1}	angular frequency of f_{L1}	87
ω_{L2}	angular frequency of f_{L2}	87
c	velocity of wave	42
c_L	velocity of longitudinal wave	100

P_{max}	maximum load of flexural test	48
b	width of specimen	48
h	height of specimen	48
a_0	notch depth	48
L	span length	48
$L^{'}$	length of specimen	56
N	number of data points	51
E_d	dynamic elastic modulus	56
$E_d^{'}$	dynamic elastic modulus after heating treatments	159
E_d^0	dynamic elastic modulus at intact state	159
M	mass	56
ϕ	phase	86
ϕ_{L1}	phase of low frequency at f_{L1}	86
ϕ_{L2}	phase of low frequency at f_{L2}	86
I	dimensionless index	112
γ	dimensionless index	159
$\psi^{'}$	parameter after thermal treatments	112
ψ_0	parameter at the intact state	112
ϵ	a small parameter	168

Chapter 1 Introduction

1. Overview

Cement-based materials (e.g., concrete and mortar) have been widely used in infrastructure because of their exceptional durability and mechanical properties. However, material limitations, design and construction practices, and severe exposure conditions can cause cement-based materials to deteriorate, which may result in aesthetic, functional, or structural problems. Furthermore, maintenance of the infrastructures takes immerse expenses and intense work. Cement-based materials can deteriorate for a variety of reasons, and damage in infrastructures made by cement-based materials is often the result of a combination of factors. In addition, damages in cement-based materials accumulate progressively under in-service loading and conditions once the infrastructures are in use. Hence, there is a powerful incentive for research to develop cost-effective, accurate, and reliable technologies for monitoring structures made by cement-based materials to enable substantial cost savings while ensuring structural safety.

Conventional non-destructive testing (NDT) and structural health monitoring (SHM) techniques are limited to detecting damage on the macro-scale. They are incapable of evaluating early-stage damage which is below the macro-scale, while material failure is imminent when macro-scale damages are detected. Vibro-acoustic technique is one of the promising NDT and SHM techniques that can detect macro-scale as well as micro-scale damages. In vibro-acoustic technique, a continuous high-frequency (HF) wave is used as the probe wave, whereas the pump wave involves application of a continuous low-frequency (LF) wave. The probe wave and the pump wave are emitted simultaneously into the monitored structures, as illustrated in Fig.1-1. When the monitored structures are intact, the spectrum of the response signal exhibits only two frequency components, i.e., frequencies of the LF probe

wave (f_L) and HF pump wave (f_H), as shown in Fig.1-1 (a). While in the damaged structure, some extra frequency components reveal in the response spectrum, which are presented as sidebands at $f_H \pm nf_L$ (n=1,2,…) as shown in Fig.1-1 (b). Fig.1-1 (c) illustrates how the signal in the time domain transfer into the frequency domain, in which sidebands are aroused due to the nonlinearity caused by defect or damage.

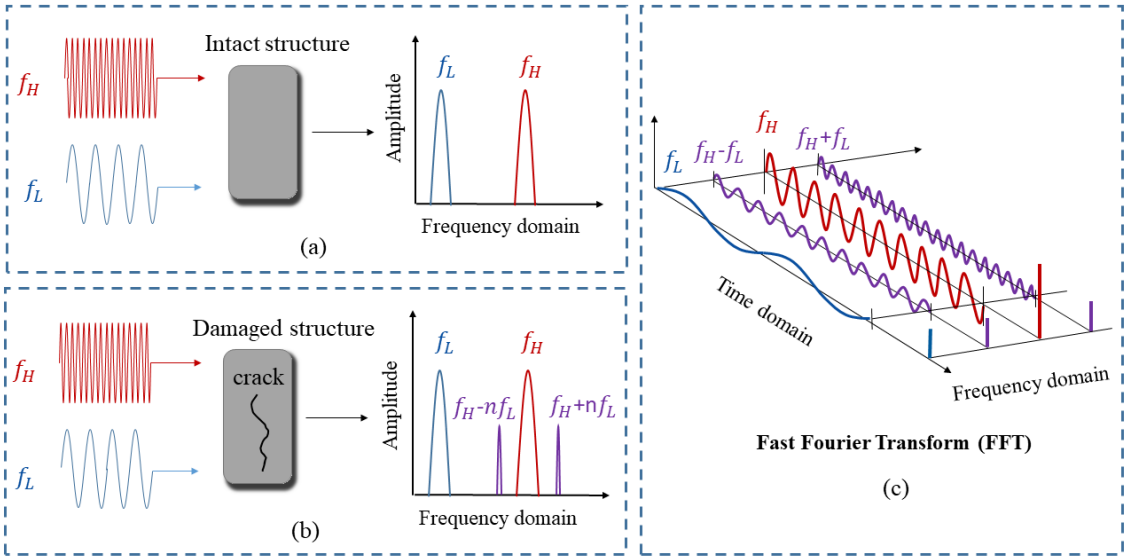

Fig.1-1 Schematic of the vibro-acoustic technique

There are two major methods in vibro-acoustic technique, namely impact-modulation (IM) and vibro-modulation (VM) method [1]. IM method employs impact excitation of structural modes, in which the specimen is struck with a small impactor, whereas VM method uses forced harmonic vibration generally emitted through an electro-mechanical driving unit. However, even though vibro-acoustic technique has been proved to be an effective and sensitive technique for damage assessment on cement-based materials, there are still some deficiencies in real applications [2-10]. For IM method, the source of LF excitation is the response from structural vibration modes, while the monitored structures always have several vibration modes, and it makes the identification of sidebands becomes difficult because multiple sidebands are frequently mixed together. In addition, the force of striking by the

impactor is small, and hence, the sidebands are sometimes masked by the noise or aliasing effect. In VM method, the frequency selection of LF pump wave is the key to achieving successful application of vibro-acoustic technique. When the frequency of LF pump wave is low or ultra-low, it causes a large burden to the electro-mechanical driving unit, and it is extraordinarily energy-consuming, particularly for long-time structural monitoring. Furthermore, some electro-mechanical driving units, such as electromagnetic shakers, are limited to emitting ultra-low frequency signals; otherwise, the electromagnetic shakers have to be larger to transmit LF signal. Therefore, it is necessary to develop a vibro-acoustic technique that is more accurate, sensitive, and cost-effective to overcome the aforementioned deficiencies.

2. Aims and Objectives

The thesis aims at developing a vibro-acoustic technique to overcome the deficiencies of inaccurate identification of sidebands, energy-consuming, and limited frequency range of electro-mechanical driving units to achieve better applications of vibro-acoustic technique in the damage detection of cement-based materials. Furthermore, nonlinear parameters are established by proposing: i) a continuous model describing the pump wave and probe wave propagating in the cement-based material, which is homogenous and isotropy but has material nonlinearity, and ii) a non-continuous model depicting the pump wave and probe wave go through contacting rough surfaces of the proposed vibro-acoustic technique. Therefore, the nonlinear parameters of the proposed vibro-acoustic technique are capable of characterizing damages caused by material nonlinearity or contact nonlinearity, and hence, its application for various damage types is promising.

The detailed objectives of this thesis are:

i) To develop the vibro-acoustic technique by investigating the properties of pump wave and probe wave and to determine the operational details of the proposed vibro-acoustic technique;

ii) To propose a continuous model for waves of proposed vibro-acoustic technique propagating in homogeneous and isotropic elastic material, and to establish the nonlinear parameter related to the sidebands and fundamental waves. This nonlinear parameter describes damages caused by material nonlinearity (e.g., thermal damages, free-thaw deterioration, and alkali-aggregate reactivity).

iii) To propose a non-continuous model for the waves of the proposed vibro-acoustic technique propagating through contacting rough surfaces, and to establish a nonlinear parameter to characterize damages caused by contact nonlinearity (e.g., cracks of overload and impact)

iv) To apply the proposed vibro-acoustic technique to evaluate different types of damage in cement-based materials by using the nonlinear parameters, and to investigate the accuracy, feasibility, and sensitivity of the proposed methods.

3. Preview of the thesis

Chapter 1 provides an overview of the existing vibro-acoustic technique for damage detection on cement-based materials to shed light on the significance of this work. *Chapter 2* presents the previous research on the nonlinear vibro-acoustic technique. The *following three chapters* are the manuscripts either published or submitted as journal papers. *Chapter 3* proposed a cross-modulated vibro-acoustic (CMVA) technique to detect damages induced by flexural tests in ultra-high-performance fibre-reinforced concrete (UHP-FRC) materials. In *Chapter 4*, three amplitude-modulated approaches, the pure amplitude-modulated (PAM), the suppressive amplitude-modulated (SAM), and the transmitted amplitude-modulated (TAM) method, were

used in the low-frequency excitation in the proposed vibro-acoustic (VA) technique to track the evolution of thermal damage in pristine graphene (PRG) mortar. Chapter 5 defined the nonlinear parameter considering higher-order effects to distinguish the different dosages of PRG mortar. Finally, *Chapter 6* summarizes the major contribution of this thesis and suggestions for future works.

References

1. Donskoy, D.M. and A.M. Sutin, *Vibro-acoustic modulation nondestructive evaluation technique.* Journal of intelligent material systems and structures, 1998. **9**(9): p. 765-771.
2. Zaitsev, V. and P. Sas, *Nonlinear response of a weakly damaged metal sample: a dissipative modulation mechanism of vibro-acoustic interaction.* Journal of Vibration and Control, 2000. **6**(6): p. 803-822.
3. Shorter, P.J. and R.S. Langley, *Vibro-acoustic analysis of complex systems.* Journal of Sound and Vibration, 2005. **288**(3): p. 669-699.
4. Duffour, P., M. Morbidini, and P. Cawley, *A study of the vibro-acoustic modulation technique for the detection of cracks in metals.* The Journal of the Acoustical Society of America, 2006. **119**(3): p. 1463-1475.
5. Zaitsev, V., et al., *Novel nonlinear-modulation acoustic technique for crack detection.* Ndt & e international, 2006. **39**(3): p. 184-194.
6. Aymerich, F. and W. Staszewski, *Experimental study of impact-damage detection in composite laminates using a cross-modulation vibro-acoustic technique.* Structural Health Monitoring, 2010. **9**(6): p. 541-553.

7. Klepka, A., et al., *Nonlinear acoustics for fatigue crack detection–experimental investigations of vibro-acoustic wave modulations.* Structural Health Monitoring, 2012. **11**(2): p. 197-211.
8. Klepka, A., et al., *Impact damage detection in laminated composites by non-linear vibro-acoustic wave modulations.* Composites Part B: Engineering, 2014. **65**: p. 99-108.
9. Pieczonka, L., et al., *Damage imaging in composites using nonlinear vibro-acoustic wave modulations.* Structural Control and Health Monitoring, 2018. **25**(2): p. e2063.
10. Li, N., F. Wang, and G. Song, *New entropy-based vibro-acoustic modulation method for metal fatigue crack detection: An exploratory study.* Measurement, 2020. **150**: p. 107075.

Chapter 2 Literature Review

1. Linear acoustic/ultrasonic nondestructive testing and structural health monitoring

It will be useful to review some widely used acoustic/ultrasonic techniques for nondestructive testing (NDT) and structural health monitoring (SHM). It can generally be divided into linear and nonlinear techniques [1]. The linear NDT and SHM techniques detect linear parameters of defects and damages responsible for wave transmission and reflection, e.g., wave velocity and magnitude attenuation.

Wave velocity, one of the important parameters for linear acoustic/ultrasonic NDT and SHM techniques, is the velocity at which a disturbance propagates in the materials [2]. The widely used general waves are longitudinal bulk waves and shear bulk waves. When there are some macro-scale defects or flaws, the wave is hindered by these discontinuities; thus, wave velocity becomes slower than it is in the intact medium. Cho investigated spectral analysis of surface waves to evaluate the compressive strength of high-strength concrete slabs through a correlation with the surface wave velocities [3]. Aggelis *et al.* proposed a combination of NDT techniques for detecting and characterizing subsurface damage in concrete. In the combined NDT technique, ultrasonic pulse velocity (UPV) was carried out to characterize the depth of cracks [4]. Zoubir *et al.* developed a methodology for NDT of the built heritage made of concrete using UPV technology [5].

However, wave velocity is an elastic wave parameter that is only sensitive to macroscopic damages. Particularly, the sensitivity of measurement of wave velocity highly depends on the wavelength. The wavelength has to be smaller than the size of the damages; hence the wave velocity is sensitive enough to characterize these damages. However, the

frequency should be high enough to achieve a small wavelength, while the propagation of HF waves in highly dissipative cement-based materials causes great energy attenuation.

Wave attenuation, is another significant parameter for linear acoustic/ultrasonic NDT and SHM techniques. The absorption mechanisms, such as internal friction and internal scatter/reflection, are the main reason for wave attenuation. When there are defects and damages in the medium, the effects of scatter/reflection are improved since scatter/reflection of the waveform at interfaces between the discontinuities can reduce wave magnitudes [6]. Landis, E.N. *et al.* carried out a study based on a point source/point receiver (PS/PR) ultrasonic test system to quantify the attenuation of ultrasonic waves in the concrete and hence characterize the degree of inhomogeneity in the material [7]. Treiber, M. *et al.* researched to explore the influence of sand aggregate on the ultrasonic attenuation towards a full simulation of more realistic structures in real concrete materials [8]. Yim, H.J. *et al.* proposed an experimental technique to quantitatively measure the wave attenuation for NDT. Meanwhile, the relevancy of the attenuation measurements for damage evaluation of cement-based material was established [9].

Nonetheless, there are several ways in which the amplitude of ultrasonic waveform can be reduced (e.g., ultrasonic beam spreading and electronic processing), which can affect the accuracy of the results. In addition, the nature of concrete as a highly attenuated mixture makes it somewhat ill-suited as a conductor of HF waves. However, HF waves with small wavelengths can identify minor structural damages, whereas LF waves are unable.

2. Distributed and localized nonlinearity

As discussed in the previous section, for widely employed wave propagation-based NDT and SHM techniques, linearity of the wave field is assumed. Therefore, the interactions between

waves and structures (e.g., scatter and reflection) are used to correlate specific signal features with potential macroscopic damages.

Recently, nonlinear properties have attracted significant attention, mainly relying on the nonlinear wave field. The nonlinear systems break the superposition principle, thus resulting in more complicated phenomena. Extra frequency components are generated as the result of the energy redistribution when waves propagate in the nonlinear systems. Different from the linear measurements (e.g., wave velocity and magnitude reduction), the nonlinear features are significantly sensitive to microscopic damage. Tiny structural changes can arouse considerable nonlinear features, particularly at the early stage when the linear measurements cannot detect those micro-scale damages [10-12].

There are two distinct damage related nonlinearities in a nonlinear system: i) distributed nonlinearity and ii) localized nonlinearity. The source of distributed nonlinearity mainly comes from material deterioration in the global sense (e.g., freeze-thaw deterioration and high-temperature conditions). From the theoretical viewpoint, the distributed nonlinearity affects the governing equation and, consequently, the iteration equations of the model that describes the wave propagating in the continuous medium [13]. Additionally, the localized nonlinearity is usually related to cracks, in which the model is usually based on weakly contacting interfaces. The localized nonlinearity is generated mainly due to overload, impact, and restrain to volume changes. Furthermore, in the theoretical model, the localized nonlinear wave interactions are reflected through additional or modified equations, and higher-order stiffness is considered [14, 15].

2.1 Distributed nonlinearity of classical nonlinear elasticity

This section presents the theoretical model describing wave propagation in the medium containing distributed nonlinearity. The governing equations of wave propagation are recapped following Ogden *et al.* [16]. It assumes that a Cartesian coordinate x_i is affixed, and the coordinate x_i is also used to present the material particle that is located at x_i in the undeformed state. At time t, the displacement of particle x_i from its initial location is denoted as $u_i = u_i(x, t)$. The equations for incremental motions due to finite-amplitude wave propagation, as well as the incremental constitutive equation for a homogeneously deformed medium can be written as:

$$\frac{\partial^2 u_k}{\partial x_j \partial x_l}\left[C_{ijkl} + M_{ijklmn}\frac{\partial u_m}{\partial x_n} + M_{ijklmnpq}\frac{\partial u_m}{\partial x_n}\frac{\partial u_p}{\partial x_q}\right] = \rho_0 \frac{\partial^2 u_i}{\partial t^2} \tag{2-1}$$

where ρ_0 is the constant mass density in the undeformed material state, and repeated indices denote summation.

$$M_{ijklmn} = C_{ijklmn} + \delta_{km}C_{ijnl} + 2\delta_{im}C_{njkl} \tag{2-2a}$$

$$M_{ijklmnpq} = C_{ijklmnpq} + \frac{3}{2}\delta_{mp}C_{ijklqn} + \frac{3}{2}\delta_{pk}C_{ijqlmn} + 3\delta_{ip}C_{qjklmn} + 3\delta_{ip}\delta_{km}C_{qjnl} \tag{2-2b}$$

where C_{ijkl}, C_{ijklmn} and $C_{ijklmnpq}$ are the second-, third-, and fourth-order elastic stiffness, respectively.

Eq. (2-1) is referred to as the elastodynamic wave equation for nonlinear elastic solids with higher-order nonlinearity, and can be decoupled as,

$$\rho_0 \ddot{u}_i^1 - C_{ijkl}u_{k,jl}^1 = 0 \tag{2-3a}$$

$$\rho_0 \ddot{u}_i^2 - C_{ijkl}u_{k,jl}^2 = f_i \tag{2-3b}$$

$$\rho_0 \ddot{u}_i^3 - C_{ijkl}u_{k,jl}^3 = g_i \tag{2-3c}$$

Terms of order greater than $\boldsymbol{u^3}$ are neglected. Hence, the total solution is $\boldsymbol{u = u^1 + u^2 + u^3}$ where $\boldsymbol{u^1 \gg u^2 \gg u^3}$. The nonhomogeneous terms in Eq. (2-3) are,

$$f_i = M_{ijklmn} u^1_{k,jl} u^1_{m,n} \tag{2-4a}$$

$$g_i = M_{ijklmn}(u^1_{k,jl} u^2_{m,n} + u^2_{k,jl} u^1_{m,n}) + \frac{1}{2} M_{ijklmnpq} u^1_{k,jl} u^1_{m,n} u^1_{p,q} \tag{2-4b}$$

In addition, $\boldsymbol{u^2}$ is driven by $\boldsymbol{u^1}$ while $\boldsymbol{u^3}$ is driven by an interaction of $\boldsymbol{u^1}$ and $\boldsymbol{u^2}$. The solution of $\boldsymbol{u^1}$ is the traditional linear elastodynamic wave equation. In the vibro-acoustic technique, the solution of $\boldsymbol{u^1}$ is the input pump wave and probe wave. Therefore, the nonlinear parameter related to the fundamental input signal and sidebands can be derived for the damage assessment.

2.2 Localized nonlinearity of classical contact models

Localized nonlinearity comes from the discontinuity of solid bodies. When two rough surfaces contact each other under compressive loading (e.g., compressive phase of pump wave), the supporting asperities undergo further flattening while other asperities keep coming into contact. This increases contact areas and reduces the gap distance between rough surfaces [17-19]. The schematic of the load-gap distance relationship of contacting rough surfaces is shown in Fig.2-1.

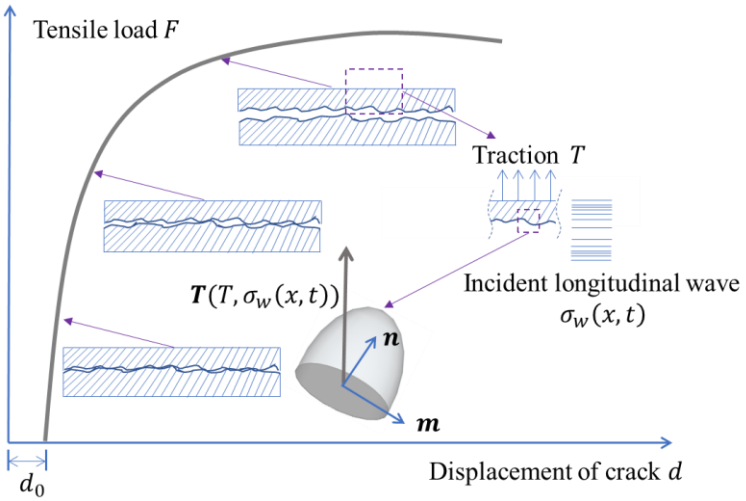

Fig. 2-1 The schematic of the load-gap relationship between two contacting rough surfaces

In the model of two contacting rough surfaces with localized nonlinearity, the mechanical response of contacting rough surfaces can be expressed as the function between the external force F and the relative displacement of crack d. In addition, the external stress $\boldsymbol{T}$ is combined stress of the traction stress T and the incident waves $\sigma_w(x,t)$. Hence, the nominal normal stress σ in the normal direction can be written as,

$$\sigma = \boldsymbol{T} \cdot \boldsymbol{n} = \sigma[d(t)] \tag{2-5}$$

where $\boldsymbol{n}$ is the normal unit vector, and σ is the function of $d(t)$.

At the initial state, the initial stress is $T_0 = -\sigma(d_0)$, which is related to the initial crack d_0 at static equilibrium. In the nonlinear spring-type interface model, the stress can be expressed as,

$$\sigma = -T_0 + K_1\xi(t) - K_2\xi(t)^2 \tag{2-6}$$

where $\xi(t) = d(t) - d_0$ is changes of displacement of crack. K is the stiffness, which is nonlinear and can be expanded as follows,

$$K_1 = \frac{\partial\sigma}{\partial d}(d_0, 0) \tag{2-7a}$$

$$K_2 = \frac{1}{2}\frac{\partial^2\sigma}{\partial d}(d_0, 0) \tag{2-7b}$$

The incident waves U_{Inc} of vibro-acoustic technique propagate through the rough interface, and then it separates into two components which are transmitted component U_{Tra} in propagating direction and reflective component U_{Ref} in the opposite direction. If there is no energy dissipation, it can be expressed as,

$$U(x,t) = \begin{cases} U_{Inc}(x-ct) + U_{Ref}(x+ct), & x < 0 \\ U_{Tra}(x-ct), & x > 0 \end{cases} \tag{2-8}$$

Additionally, the boundary conditions between two rough surfaces is,

$$\sigma(+0,t) = \sigma(-0,t) = -[T_0 + \tilde{p}(t)] \tag{2-9}$$

where "+" indicates the side of the interface in propagating direction while "−" presents the side of the interface opposite to the propagating direction. Furthermore, $\tilde{p}(t)$ is the dynamic contacting stress due to the incident waves.

The dynamic opening displacement of crack can be written as,

$$\xi(t) = U(+0, t) - U(-0, t) \tag{2-10}$$

Combining Eq. (2-6), (2-8), and (2-10) with the function of the incident probe and pump waves, the solution of the reflected wave and transmitted wave after propagating through the rough interfaces will be obtained. Therefore, the nonlinear parameter in this modal with localized nonlinearity can be defined by the relationship between fundamental waves and sidebands.

3. Nonlinear acoustic/ultrasonic nondestructive testing and structural health monitoring

Nonlinear acoustic/ultrasonic techniques are effective and sensitive for microscale damage detection, in contrast to linear acoustic/ultrasonic techniques, which are only useful for identifying macroscale damages [20]. The linear acoustic techniques usually use signals below 20 kHz, while the nonlinear ultrasonic techniques utilize signals in the ultrasonic range above 20 kHz. The nonlinear approaches are generally based on the frequency variation as the result of the wave-damage interactions. More specifically, the damage-induced nonlinearity mentioned in Section 2.2 can result in the creation of accompanying harmonics [10, 21], sidebands between different frequencies [22, 23], and shifts of resonant frequencies due to various driving inputs [24, 25]. These nonlinear features can be observed in the course of structural changes generations much sooner than any linear features (e.g., wave velocity and

attenuation) can be identified. Hence, the nonlinear features of nonlinear acoustic/ultrasonic techniques are more practical, particularly in the early-damage state.

3.1 Finite amplitude ultrasonic technique

The finite amplitude ultrasonic technique is one of the nonlinear approaches, in which the harmonics are used for damage assessment. When the input signal with frequency f propagates through the source of nonlinearity, it is distorted, which leads to the generation of higher-order harmonics at $2f$, $3f$, etc. The phenomenon of higher-order harmonics was first observed in liquids by optical and acoustic filter methods, and then this behavior of finite amplitude waves was found in solids in the 1960s by Breazeale and Thompson [26]. Afterward, the finite amplitude ultrasonic technique using the nonlinear distortion of higher-order harmonics was investigated for damage detection in mental materials. Fatigue is one of the most common degradation mechanisms in metals. Previous studies revealed that fatigue damage was initially generated in the form of dislocation structures, such as veins and persistent slip bands (PSBs), the latter of which accumulated at grain boundaries to produce strain localization and then led to microcracks [27]. These dislocations are difficult to be identified by the conventional linear techniques, which rely on the linear macroscopic properties while it can cause large changes in nonlinear properties that are manifested as higher-order harmonics. Therefore, finite-amplitude ultrasonic technique can be used to quantify the presence and the density of dislocation in metals, particularly for the evolution and accumulation of the dislocation at the early-damage state [27-33]. Furthermore, the nonlinear finite-amplitude ultrasonic technique has also been demonstrated can also be used for hardening [34], thermal aging [35-37], and corrosion [38, 39] damage detection in metallic materials.

Afterward, the finite amplitude ultrasonic technique has been applied to non-metal materials, particularly cement-based materials. Shah and Ribakov conducted experiments on concrete specimens, which were cast with *different water-cement ratios under compression* in several steps up to the ultimate load bearing capacity through the finite amplitude ultrasonic technique [40]. Kim *et al*. proposed an air-coupled method for the application of finite amplitude ultrasonic technique using Rayleigh surface waves to quantify microstructural changes caused by the effect of *shrinkage reducing admixtures* [41, 42] and *alkali-silica reaction (ASR)* [43]. They also developed and implemented a finite amplitude ultrasonic technique to characterize the effect of *carbonation* on concrete. The sensitivity of the nonlinear parameter β was verified by comparing it with the measured Rayleigh wave velocity [44]. Furthermore, Kim *et al*. conducted in situ measurements for real-time monitoring of *load-induced* damages in concrete using the second harmonic generation finite amplitude technique with a non-contact detection method [45]. Mingjie *et al*. investigated second-order nonlinear parameter β and third-order nonlinear parameter γ for *artificial induced damage* detection on concrete materials through finite amplitude ultrasonic technique [46]. Arumaikani et al. focused on the detection of *corrosion damage* in reinforced concrete elements through the nonlinear ultrasonic technique. One of the nonlinear ultrasonic techniques was finite amplitude ultrasonic technique. It was found that as the corrosion progressed and cracks appeared on the surface of the concrete, β was quite efficient compared to measurements of other techniques [47].

The previous studies show that the nonlinear finite-amplitude ultrasonic technique can characterize different structural changes in cement-based materials, including load-induced damages, shrinkage, ASR reaction, carbonation, and corrosion damages. The nonlinear finite-amplitude ultrasonic technique has a good ability to distinguish microstructural changes while

they are difficult to be identified through the conventional linear technique, particularly at the early damage state.

The nonlinear finite-amplitude ultrasonic technique employs a monochromatic pulse as the input signal. The sensitivity of the finite amplitude ultrasonic technique significantly relies on the frequency or wavelength of the input signal. When the wavelength of the input signal is small (or the frequency is high) enough compared with the size of structural changes, then it can obtain the information on the microscale. While the wavelength is large, the information on damages and defects is easily omitted because the nonlinearity due to the microscale changes is negligible. However, cement-based material is one of the energy dissipated materials, in which the wave has large attenuation during the propagating, particularly for HF waves.

3.2 Frequency shift technique

The frequency shift technique utilizes the nonlinear phenomenon that the presence of a nonlinear source is manifested by a shift in the resonant frequency as the amplitude of the driving input changes [48]. Cement-based materials are known to behave in a nonlinear and hysteretic fashion, particularly at higher mechanical energy levels. The frequency shift technique relies on the hysteretic fashion that causes a significant softening of material with increasing vibrational strain energy. Therefore, when the forces of vibration increase, the resonant frequency shifts are more intense, and the amplitudes of frequencies become smaller, as shown in Fig.2-2.

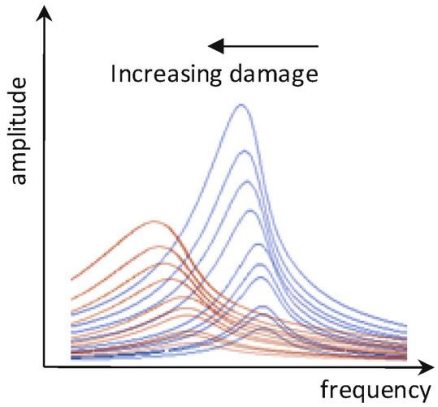

Fig. 2-2 The expected evolution of the resonant spectrums with increasing damage. The frequency shift of red lines is larger than the frequency shift of purple lines, which indicates that the damages presented in red are larger than the damages in purple. [25]

Research conducted by Jun et al. [49] and Krzysztof *et al*. [50] reported that the nonlinear impact resonance acoustic spectroscopy (NIRAS) technique could be applied to characterize progressive *ASR damages*. Additionally, Some studies demonstrated that the NIRAS technique could be successfully applied for detecting *thermal damages* [51] and *external sulfate attack* [52] in concrete.

Afterward, advances in the NIRAS technique have led to the single impact event approach, which relies on a signal processing perspective. In contrast, previous NIRAS techniques have to obtain a group of impact signals with varying input force amplitudes. Eiras *et al*. proposed a nonclassical NIRAS technique, which used windows with different lengths to process a single impact signal to assess the concrete subjected to *freezing-thawing cycles* [53]. Carrión proposed a new flipped accumulative nonlinear single impact acoustic spectroscopy (FANSIRAS) technique. This study investigated the application of the FANSIRAS technique to identify *thermally damaged* concrete [54].

However, in real field applications, it is difficult to obtain the resonant response of structures made of cement-based materials because they are generally in large size with an ultra-low resonant response, even of a few to dozens of Hertz. Furthermore, data processing of

frequency shift technique, especially for the single impact event approach, requires the resonant response to have sufficient cycles. Because in the single impact event approach, the windows with varying lengths or the windows with the same length but different positions have been applied to the data processing, and hence adequate cycles which can promise enough information are included by the various windows to attain the significant frequency shift in the spectrum.

3.3 vibro-acoustic technique

In vibro-acoustic technique, when two input waves at frequency f_H and f_L encounter the nonlinear sources, sideband components are generated at frequencies $f_H \pm n \cdot f_L$ (n = 1,2,3 ...), where f_H is HF wave and f_L is LF wave. There are generally two alternative LF wave sources: (i) the impact method and (ii) the forced method. In the impact method, the structure is struck with an impactor, and the LF wave is the resonant frequency of the structure, while the forced method employs an electro-mechanical driving unit to vibrate the structure by the harmonics [55]. The weak LF wave can provide an intensive, high-amplitude field in order to perturb material defects, and the HF wave is used to monitor structural changes [56].

However, the application of the impact method has some limitations: (i) the resonant frequency of the structure is not isolated but multiple, which makes identification of sidebands difficult. In addition, the sidebands of the impact method are easily masked by the aliasing effect or noise level. (ii) The structures made of cement-based materials are usually in large sizes, of which the resonant frequency is in the low or ultralow range. Thus, the sidebands $f_H \pm n \cdot f_L$ are quite close to the frequency f_H of probe wave, which are easily masked with f_H when processing data. Furthermore, in the forced method, the frequency of input signals should be carefully selected because the generation of nonlinear modulation also depends on the choice

of the input frequencies. Particularly, emitting low and ultra-low frequency pump wave for long-term monitoring greatly burdens the electro-mechanical driving unit.

Though the finite amplitude ultrasonic technique and frequency shift technique mentioned above is able to detect micro- and macroscale damages from the early to ultimate stage, the vibro-acoustic technique has the following advantages: (i) the modulation effect is not easy to affect by the other unwanted nonlinearity (e.g., transducer, amplifier, and coupling conditions); (ii) in LF signal can provide intensive perturbed field which has weak energy attenuation while the HF signal has adequately small wavelength to scan the tiny structural changes which promise the sensitivity of this technique. Therefore, researchers have a powerful impetus to develop the vibro-acoustic technique to achieve more robustness, applicability, and energy-saving.

4. Non-conventional vibro acoustic technique

There are two trends in vibro-acoustic technique: (i) to utilize practical strategies such as using a noncontact transducer [57, 58] or laser-based measurement [59, 60], and (ii) to focus on enhancing the signal processing by employing sweeping signal [61] or using sideband peak count method [62]. The improvement of signal processing attracts considerable attention because the related investigations lead to more sensitive, effective, and practical without updating instruments. The following sections discuss new developments in vibro-acoustic techniques with new signal processing approaches.

4.1 Applications on non-cement-based materials

To address the issue of variations of structural resonant response due to different environments and boundary conditions, Nathanael and Douglas proposed a vibro-acoustic modulation technique utilizing a swept probing signal to detect a *steel beam with fatigue cracks* [61]. Hoon *et al.*[62] and Lim *et al.* [63] proposed a signal process approach of vibro-acoustic modulation technique, which combined linear response subtraction (LRS) and synchronous demodulation (SD), for crack detection of actual *fatigue cracks* grown in a *metallic plate* and *complex fitting-lug specimens*. In addition, the first sideband spectrogram (FSS) was employed by using the sweeping pump and probe waves. Peipei et al. developed the vibro-acoustic technique using only one broadband pulse signal as the driving input generated through a laser beam. Furthermore, the nonlinear feature of sideband peak count (SPC) is extracted from the spectral plot to measure the degree of *fatigue damage in an aluminum plate* [64]. Lim et al. investigated a completed non-contact fatigue crack visualization method based on the nonlinear vibro-acoustic modulation technique to successfully visualize *micro- and macro-cracks in an aluminum plate* [65]. Furui and Gangbing applied the linear swept pump and probe wave to replace prior single harmonic waves to the vibro-acoustic technique for *bolt early looseness* monitoring. Meanwhile, the time reversal (TR) method was used to overcome signal energy dissipation and low signal-to-noise ratio (SNR) [66]. Ning et al. proposed a new entropy-based damage index using the multiscale permutation entropy (MPE) of vibro-acoustic technique to monitor fatigue crack width. In this study, both LF and HF excitations were linear swept sine waves [67]. It can be found that most developed vibro-acoustic modulation techniques have been studied to apply to metallic and composite materials. However, the merit of the vibro-acoustic technique that LF excitation can be used to intensively perturb cracks and defects as well as to achieve low energy attenuation was not revealed in non-cement-based materials.

Therefore, the research to investigate the applications of new vibro-acoustic modulation techniques to cement-based materials are critical.

4.2 Applications on cement-based materials

Cement-based material is a kind of combined material, of which the properties are quite complicated. In addition, cement-based material has a large energy attenuation when acoustic/ultrasonic waves propagate through the medium; however, the structures made of cement-based material are usually large in size, making the attenuation effect more significant for the NDT & SHM. Compared to the other techniques, such as finite-amplitude ultrasonic and nonlinear frequency shift techniques, the vibro-acoustic is more suitable for damage assessment and monitoring. Many studies have focused on the developed vibro-acoustic technique to detect various damages in cement-based material. Wu *et al.* developed a nonlinear vibro-acoustic modulation technique using non-contact piezoelectric sensors to detect the concrete crack due to thermal treatments [68, 69]. Pranav *et al.* extended the application of the vibro-acoustic technique for diagnosing ASR damage in concrete structures, particularly to achieve damage localization [70]. Yin *et al.* developed a cross-modulated vibro-acoustic technique to detect damages induced by flexural loading in UHP-FRC material, which is more energy-efficient than the conventional vibro-acoustic technique [71]. Yin et al. proposed an amplitude-modulation vibro-acoustic (AMVA) technique, including the pure amplitude-modulated (PAM), the suppressive amplitude-modulated (SAM), and the VM (TAM) method, to track the evolution of thermal damage in pristine graphene mortar. The results show that the proposed AMVA techniques are sensitive and feasible to serve as the tool for damage detection in cement-based material [72]. However, the studies to investigate the development of vibro-acoustic techniques for damage characterization on cement-based materials are still inadequate in the literature.

5. Summary and research gaps

From the literature review, it can be found that the centre of interest in NDT and SHM techniques has been shifted from linear to nonlinear approaches in order to achieve more sensitivity, feasibility, and less energy consumption. As mentioned above, when using the monochromatic signal, the high-frequency signal has large energy dissipation when propagating in cement-based material, while the LF signal is not sensitive enough since the wavelength is larger than the size of the microscale defects and damages. One of the most attractive NDT and SHM techniques is the vibro-acoustic technique, which takes advantage of combining the LF excitation and HF wave. The LF excitation can afford an intensive field to perturb damages while the HF wave is used to scan the damages; therefore, more abundant information on damages is obtained for further analysis. However, the classical IM vibro-acoustic technique utilizing the resonant response as the source of LF excitation is affected by the multiple structural responses, making identifying sidebands difficult. Furthermore, the sidebands sometimes are masked by the noise level or aliasing effect. From the aspect of the classical VM vibro-acoustic technique, in which the LF signal is emitted through the electro-forced unit and generally be a single frequency harmonic. The selection of the frequency of LF signal is a crucial procedure for the successful application. When the frequency of the pump wave is higher, the sidebands distribute in a wide range in the frequency spectrum. The receiving instrument requires a broadband receiving range, such as the laser vibrometer or broadband transducer, which increases the testing cost. While using the lower pump wave brings a large burden to the electro-forced unit to emit a low/ultralow signal, particularly for long-term SHM. Therefore, this study focuses on the investigation to develop vibro-acoustic for more applicable, sensitive, and energy-saving for NDT and SHM in cement-based material. In particular:

- To enhance the practicability of vibro-acoustic technique:

(1.1) to investigate the possibility of applying amplitude-modulated waves in the vibro-acoustic technique;

(2) to explore the proper methods for combing amplitude-modulated LF pump wave and HF probe wave;

(3) to investigate the sensitivity and feasibility of the proposed vibro-acoustic technique, which uses amplitude-modulated waves to detect various damages in cement-based materials;

(4) to compare the power consumption of the proposed vibro-acoustic technique and the conventional vibro-acoustic technique.

- To define the proper nonlinear parameters of the proposed vibro-acoustic technique:

  (1) to establish a theoretical model with material nonlinearity, where amplitude-modulated LF wave and HF wave propagate through, and a nonlinear parameter is going to build based on this model;

  (2) to establish a theoretical model with material nonlinearity, where amplitude-modulated LF wave and HF wave propagate through, and a nonlinear parameter is going to build based on this model;

  (3) to induce second-order and third-order nonlinear terms in the wave equation, for there are at least three frequency components in the proposed vibro-acoustic technique, and the sum- and difference-frequency interactions are more comprehensive.

References

1. Pfleiderer, K., I. Solodov, and G. Busse, *New opportunities in acoustic NDT using frequency conversion by nonlinear defects.* Emerging Technologies in NDT, 2008: p. 89.
2. McCann, D. and M. Forde, *Review of NDT methods in the assessment of concrete and masonry structures.* Ndt & E International, 2001. **34**(2): p. 71-84.
3. Cho, Y.S., *NDT response of spectral analysis of surface wave method to multi-layer thin high-strength concrete structures.* Ultrasonics, 2002. **40**(1-8): p. 227-230.
4. Aggelis, D., et al., *NDT approach for characterization of subsurface cracks in concrete.* Construction and Building Materials, 2011. **25**(7): p. 3089-3097.
5. Sbartaï, Z.-M., et al., *Combining NDT techniques for improved evaluation of concrete properties.* Cement and Concrete Composites, 2012. **34**(6): p. 725-733.
6. Rose, J.L., *Ultrasonic guided waves in solid media*. 2014: Cambridge university press.
7. Landis, E.N. and S.P. Shah, *Frequency-dependent stress wave attenuation in cement-based materials.* Journal of Engineering Mechanics, 1995. **121**(6): p. 737-743.
8. Treiber, M., et al., *Effects of sand aggregate on ultrasonic attenuation in cement-based materials.* Materials and structures, 2010. **43**(1): p. 1-11.
9. Yim, H.J., H.-G. Kwak, and J.H. Kim, *Wave attenuation measurement technique for nondestructive evaluation of concrete.* Nondestructive Testing and Evaluation, 2012. **27**(1): p. 81-94.
10. Chen, J., et al., *Characterization of thermal damage in sandstone using the second harmonic generation of standing waves.* International Journal of Rock Mechanics and Mining Sciences, 2017. **91**: p. 81-89.
11. Dwivedi, S.K., M. Vishwakarma, and A. Soni, *Advances and researches on non destructive testing: A review.* Materials Today: Proceedings, 2018. **5**(2): p. 3690-3698.

12. Kim, J.-Y., et al., *Use of a non-collinear wave mixing technique to image internal microscale damage in concrete.* Journal of Applied Physics, 2022. **131**(14): p. 145102.
13. Vidler, J., A. Kotousov, and C.-T. Ng, *Effective elastic properties of a weakly nonlinear particulate composite.* International Journal of Non-Linear Mechanics, 2022: p. 103949.
14. Biwa, S., S. Nakajima, and N. Ohno, *On the acoustic nonlinearity of solid-solid contact with pressure-dependent interface stiffness.* J. Appl. Mech., 2004. **71**(4): p. 508-515.
15. Hériveaux, Y., et al., *Analytical modeling of the interaction of an ultrasonic wave with a rough bone-implant interface.* Ultrasonics, 2020. **108**: p. 106223.
16. Ogden, R.W., *Incremental statics and dynamics of pre-stressed elastic materials*, in *Waves in nonlinear pre-stressed materials*. 2007, Springer. p. 1-26.
17. Baik, J.-M. and R.B. Thompson, *Ultrasonic scattering from imperfect interfaces: a quasi-static model.* Journal of Nondestructive Evaluation, 1984. **4**(3): p. 177-196.
18. Baltazar, A., et al., *Inverse ultrasonic determination of imperfect interfaces and bulk properties of a layer between two solids.* The Journal of the Acoustical Society of America, 2003. **114**(3): p. 1424-1434.
19. Biwa, S., *Second-harmonic generation at contacting interfaces*, in *Nonlinear Ultrasonic and Vibro-Acoustical Techniques for Nondestructive Evaluation*. 2019, Springer. p. 263-299.
20. Jhang, K.-Y., *Nonlinear ultrasonic techniques for nondestructive assessment of micro damage in material: a review.* International journal of precision engineering and manufacturing, 2009. **10**(1): p. 123-135.
21. Chen, J., J. Ren, and T. Yin, *Nondestructive evaluation of notched cracks in mortars by nonlinear ultrasonic technique.* Nondestructive Testing and Evaluation, 2016. **31**(2): p. 109-121.

22. Chen, J., et al., *Characterization of concentrated and distributed cracks in concrete using a harmonic wave modulation technique.* Materials and Structures, 2018. **51**(1): p. 1-10.

23. Pieczonka, L., et al., *Impact damage detection in light composite sandwich panels using piezo-based nonlinear vibro-acoustic modulations.* Smart Materials and Structures, 2014. **23**(10): p. 105021.

24. Chen, J., et al., *Assessment of sulfate attack and freeze–thaw cycle damage of cement-based materials by a nonlinear acoustic technique.* Materials and Structures, 2017. **50**(2): p. 1-10.

25. Eiras, J., et al., *Cement-based material characterization using nonlinear single-impact resonant acoustic spectroscopy (NSIRAS)*, in *Nonlinear Ultrasonic and Vibro-Acoustical Techniques for Nondestructive Evaluation*. 2019, Springer. p. 487-508.

26. Breazeale, M. and D. Thompson, *Finite-amplitude ultrasonic waves in aluminum.* Applied Physics Letters, 1963. **3**(5): p. 77-78.

27. Kim, J.-Y., et al., *Experimental characterization of fatigue damage in a nickel-base superalloy using nonlinear ultrasonic waves.* The Journal of the Acoustical Society of America, 2006. **120**(3): p. 1266-1273.

28. Cantrell, J.H. and W.T. Yost, *Acoustic harmonic generation from fatigue-induced dislocation dipoles.* Philosophical magazine A, 1994. **69**(2): p. 315-326.

29. Barnard, D., G. Dace, and O. Buck, *Acoustic harmonic generation due to thermal embrittlement of Inconel 718.* Journal of Nondestructive Evaluation, 1997. **16**(2): p. 67-75.

30. Hurley, D.C., et al., *Nonlinear ultrasonic parameter in quenched martensitic steels.* Journal of Applied Physics, 1998. **83**(9): p. 4584-4588.

31. Frouin, J., et al. *In-situ monitoring of acoustic linear and nonlinear behavior of titanium alloys during cycling loading*. in *Nondestructive Evaluation of Aging Materials and Composites III*. 1999. SPIE.

32. Cantrell, J.H. and W.T. Yost, *Nonlinear ultrasonic characterization of fatigue microstructures.* International Journal of fatigue, 2001. **23**: p. 487-490.

33. Cantrell, J.H., *Quantitative assessment of fatigue damage accumulation in wavy slip metals from acoustic harmonic generation.* Philosophical Magazine, 2006. **86**(11): p. 1539-1554.

34. Hurley, D.C., D. Balzar, and P. Purtscher, *Nonlinear ultrasonic assessment of precipitation hardening in ASTM A710 steel.* Journal of Materials Research, 2000. **15**(9): p. 2036-2042.

35. Choi, Y., et al., *Application of non-linear acoustic effect for evaluation of degradation of 2.25 Cr-1Mo steel.* Journal of the Korean Society for Nondestructive Testing, 2002. **22**(2): p. 170-176.

36. Park, I.-K., H.-M. Kim, and K.-Y. Jhang. *Nondestructive Evaluation of Degraded 2.25 Cr-1Mo Steel and Estimation of Nonlinear Acoustic Effect using Bispectral Analysis*. in *ASME Pressure Vessels and Piping Conference*. 2003.

37. Metya, A., et al., *Higher harmonic analysis of ultrasonic signal for ageing behaviour study of C-250 grade maraging steel.* Ndt & E International, 2008. **41**(6): p. 484-489.

38. Zeitvogel, D.T., et al., *Characterization of stress corrosion cracking in carbon steel using nonlinear Rayleigh surface waves.* Ndt & E International, 2014. **62**: p. 144-152.

39. Ding, X., et al., *Experimental investigation of the surface corrosion damage in plates based on nonlinear Lamb wave methods.* Ndt & E International, 2021. **121**: p. 102466.

40. Shah, A. and Y. Ribakov, *Non-linear ultrasonic evaluation of damaged concrete based on higher order harmonic generation.* Materials & Design, 2009. **30**(10): p. 4095-4102.

41. Kim, G., et al., *Air-coupled detection of nonlinear Rayleigh surface waves in concrete—Application to microcracking detection.* Ndt & E International, 2014. **67**: p. 64-70.

42. Kim, G., et al., *Drying shrinkage in concrete assessed by nonlinear ultrasound.* Cement and Concrete Research, 2017. **92**: p. 16-20.

43. Kim, G., et al., *Measuring alkali-silica reaction (ASR) microscale damage in large-scale concrete slabs using nonlinear Rayleigh surface waves.* Journal of Nondestructive Evaluation, 2017. **36**(2): p. 1-6.

44. Kim, G., et al., *Quantitative evaluation of carbonation in concrete using nonlinear ultrasound.* Materials and Structures, 2016. **49**(1): p. 399-409.

45. Kim, G., et al., *In situ nonlinear ultrasonic technique for monitoring microcracking in concrete subjected to creep and cyclic loading.* Ultrasonics, 2018. **88**: p. 64-71.

46. Zhao, M., et al., *Nonlinear ultrasonic test of concrete cubes with induced crack.* Ultrasonics, 2019. **97**: p. 1-10.

47. Arumaikani, T., S. Sasmal, and T. Kundu, *Detection of initiation of corrosion induced damage in concrete structures using nonlinear ultrasonic techniques.* The Journal of the Acoustical Society of America, 2022. **151**(2): p. 1341-1352.

48. Sohn, H., et al., *Noncontact nonlinear ultrasonic wave modulation for fatigue crack and delamination detection,* in *Nonlinear Ultrasonic and Vibro-Acoustical Techniques for Nondestructive Evaluation*. 2019, Springer. p. 661-697.

49. Chen, J., et al., *Rapid evaluation of alkali–silica reactivity of aggregates using a nonlinear resonance spectroscopy technique.* Cement and Concrete Research, 2010. **40**(6): p. 914-923.

50. Leśnicki, K.J., et al., *Characterization of ASR damage in concrete using nonlinear impact resonance acoustic spectroscopy technique.* NDT & E International, 2011. **44**(8): p. 721-727.

51. Payan, C., et al., *Quantitative linear and nonlinear resonance inspection techniques and analysis for material characterization: Application to concrete thermal damage.* The Journal of the Acoustical Society of America, 2014. **136**(2): p. 537-546.

52. Genovés, V., et al., *Preliminary study on short-term sulphate attack evaluation by non-linear impact resonance acoustic spectroscopy technique.* Construction and Building Materials, 2015. **78**: p. 295-302.

53. Eiras, J., et al., *Non-classical nonlinear feature extraction from standard resonance vibration data for damage detection.* The Journal of the Acoustical Society of America, 2014. **135**(2): p. EL82-EL87.

54. Carrión, A., et al., *Effects of slow dynamics and conditioning on non-linear hysteretic material assessment using impact resonance acoustic spectroscopy.* Mechanical Systems and Signal Processing, 2021. **150**: p. 107273.

55. Donskoy, D.M. and A.M. Sutin, *Vibro-acoustic modulation nondestructive evaluation technique.* Journal of intelligent material systems and structures, 1998. **9**(9): p. 765-771.

56. Klepka, A., et al., *Structural damage detection based on nonlinear acoustics: application examples*, in *Nonlinear Ultrasonic and Vibro-Acoustical Techniques for Nondestructive Evaluation*. 2019, Springer. p. 139-174.

57. Ballad, E., et al., *Nonlinear modulation technique for NDE with air-coupled ultrasound.* Ultrasonics, 2004. **42**(1-9): p. 1031-1036.

58. Kažys, R., et al., *Air-coupled ultrasonic investigation of multi-layered composite materials.* Ultrasonics, 2006. **44**: p. e819-e822.

59. Kim, H., et al., *A noncontact NDE method using a laser generated focused-Lamb wave with enhanced defect-detection ability and spatial resolution.* Ndt & E International, 2006. **39**(4): p. 312-319.

60. An, Y.-K., B. Park, and H. Sohn, *Complete noncontact laser ultrasonic imaging for automated crack visualization in a plate.* Smart Materials and Structures, 2013. **22**(2): p. 025022.

61. Yoder, N.C. and D.E. Adams, *Vibro-acoustic modulation utilizing a swept probing signal for robust crack detection.* Structural Health Monitoring, 2010. **9**(3): p. 257-267.

62. Sohn, H., et al., *Nonlinear ultrasonic wave modulation for online fatigue crack detection.* Journal of Sound and Vibration, 2014. **333**(5): p. 1473-1484.

63. Lim, H.J., et al., *Reference-free fatigue crack detection using nonlinear ultrasonic modulation under various temperature and loading conditions.* Mechanical Systems and Signal Processing, 2014. **45**(2): p. 468-478.

64. Liu, P., et al., *Noncontact detection of fatigue cracks by laser nonlinear wave modulation spectroscopy (LNWMS).* NDT & E International, 2014. **66**: p. 106-116.

65. Lim, H.J., et al., *Noncontact fatigue crack visualization using nonlinear ultrasonic modulation.* Ndt & E International, 2015. **73**: p. 8-14.

66. Wang, F. and G. Song, *Bolt early looseness monitoring using modified vibro-acoustic modulation by time-reversal.* Mechanical Systems and Signal Processing, 2019. **130**: p. 349-360.

67. Li, N., F. Wang, and G. Song, *New entropy-based vibro-acoustic modulation method for metal fatigue crack detection: An exploratory study.* Measurement, 2020. **150**: p. 107075.

68. Wu, Y. and J. Chen. *Non-contact assessment of thermal damage of concrete using a nonlinear wave modulation technique*. in *Nondestructive Characterization and Monitoring of Advanced Materials, Aerospace, Civil Infrastructure, and Transportation XIII*. 2019. SPIE.

69. Chen, J., Y. Wu, and C. Yang, *Damage assessment of concrete using a non-contact nonlinear wave modulation technique.* NDT & E International, 2019. **106**: p. 1-9.

70. Karve, P., et al., *Vibro-acoustic modulation and data fusion for localizing alkali–silica reaction–induced damage in concrete.* Structural Health Monitoring, 2020. **19**(6): p. 1905-1923.

71. Yin, T., C.-T. Ng, and A. Kotousov, *Damage detection of ultra-high-performance fibre-reinforced concrete using a harmonic wave modulation technique.* Construction and Building Materials, 2021. **313**: p. 125306.

72. Yin, T., et al., *Amplitude-Modulation Vibro-Acoustic Technique for Damage Evaluation.* Structural Health Monitoring, 2022: p. 14759217221106209.

Chapter 3

Damage detection of ultra-high-performance fibre-reinforced concrete using a harmonic wave modulation technique

This chapter is based on the following published paper:

Yin, T., Ng, C.T., and Kotousov, A., 2021. Damage detection of ultra-high-performance fibre-reinforced concrete using a harmonic wave modulation technique. Construction and Building Materials, 313, p.125306.

Statement of Authorship

Title of Paper	Damage detection of ultra-high-performance fibre-reinforced concrete using a harmonic wave modulation technique
Publication Status	☑ Published ☐ Accepted for Publication ☐ Submitted for Publication ☐ Unpublished and Unsubmitted w ork w ritten in manuscript style
Publication Details	Yin, Tingyuan, Ching-Tai Ng, and Andrei Kotousov. "Damage detection of ultra-high-performance fibre-reinforced concrete using a harmonic wave modulation technique." Construction and Building Materials 313 (2021): 125306.

Principal Author

Name of Principal Author (Candidate)	Tingyuan Yin		
Contribution to the Paper	Conceptualization, Methodology, Writing – original draft, Data curation		
Overall percentage (%)	80%		
Certification:	This paper reports on original research I conducted during the period of my Higher Degree by Research candidature and is not subject to any obligations or contractual agreements with a third party that would constrain its inclusion in this thesis. I am the primary author of this paper.		
Signature		Date	22/09/2022

Co-Author Contributions

By signing the Statement of Authorship, each author certifies that:

i. the candidate's stated contribution to the publication is accurate (as detailed above);

ii. permission is granted for the candidate in include the publication in the thesis; and

iii. the sum of all co-author contributions is equal to 100% less the candidate's stated contribution.

Name of Co-Author	Ching-Tai Ng		
Contribution to the Paper	Conceptualization, Supervision, Writing – review & editing		
Signature		Date	23/09/2022

Name of Co-Author	Andrei Kotousov		
Contribution to the Paper	Conceptualization, Supervision, Writing – review & editing		
Signature		Date	23/09/2022

Please cut and paste additional co-author panels here as required.

Damage detection of ultra-high-performance fibre-reinforced concrete using a harmonic wave modulation technique

Tingyuan Yin[1], Ching-Tai Ng[1,*], Andrei Kotousov[2]

[1] School of Civil, Environmental & Mining Engineering, The University of Adelaide, SA 5005, Australia

[2] School of Mechanical Engineering, The University of Adelaide, SA 5005, Australia

Abstract

In this paper, a damage detection technique, named cross-modulated vibro-acoustic (CMVA) technique, is proposed to detect damages induced by flexural loading in ultra-high-performance fibre-reinforced concrete (UHP-FRC) material. Different from conventional vibro-acoustic methods, the pump wave of the proposed CMVA technique is modulated by two low-frequency waves to address limitations of pump wave generator on excitation frequency. The proposed technique has lower power consumption and high sensitivity to micro-damages. In this study, a mechanical model of contact nonlinearity at interfaces is developed to establish the nonlinear parameter D_α for the proposed CMVA technique in describing various flexural damage levels. The conventional resonant frequency (RF) test based on ASTM C215-02, is conducted to compare with the results of the proposed CMVA technique. This study presents the application of the proposed CMVA technique to monitor the damage evolution the UHP-FRC structure. The experimental results show that the sensitivity of D_α to early-stage damages and material degradation is much higher than the conventional measurement of RF test. Therefore, the CMVA technique is an accurate and reliable technique to monitor progressive damages in structures.

* Corresponding author: alex.ng@adelaide.edu.au

Keywords: cross-modulation, damage detection, nonlinear features, ultrasonic, ultra-high-performance concrete, harmonic wave modulation

1. Introduction

Concrete is one of the most commonly used materials in civil infrastructures and buildings throughout the world. To improve its strength, toughness and durability of concrete, researchers have developed different approaches to enhance its engineering properties so that its usages in construction can be further extended. Fibre-reinforced concrete is one of the potential materials to meet the high demands of modern civil engineering construction. The buildings and infrastructures made by this material can be subjected to extreme loads or conditions, e.g. earthquakes, strong winds and fires, or long-term attacks, e.g. freeze-thaw deterioration, chemical erosion and alkali-aggregate reaction [1, 2] and damage or aging may happen on the structures. Therefore, non-destructive evaluation (NDE) techniques for detecting and evaluating damages after short-term overloads and structural health monitoring (SHM) techniques for monitoring accumulated damages under long-term attacks are of great importance in civil engineering structures.

Acoustic and ultrasonic techniques have been applied to ensure the safety and integrity of concrete in the literature because of their simple operation procedure, less labour cost and relative low-priced instrumentation compared to other advanced NDT techniques. Linear features of acoustic and ultrasonic techniques, such as velocity [3-6] and amplitude attenuation [7, 8] of the acoustic and ultrasonic waves, have been widely used to assess various damages in concrete. However, it has been demonstrated that these linear features of acoustic and ultrasonic techniques are not sensitive enough to provide early-stage detection of damage for concrete structures. It is because these techniques are based on linear constitutive relationship, by which it assumes damage in medium only affect elastic modulus. But the effect of the decrease in elastic modulus is insensitive even when macro-crack is evident.

1.1 Vibro-acoustic techniques

Recently, acoustic and ultrasonic techniques based on nonlinear features, such as higher harmonics, frequency shift and sidebands, have attracted significant research interests in the area of NDE and SHM [9-12]. It has been demonstrated that these nonlinear features are attractive for damage detection because they are not only susceptible to the formation of macro-cracks but also the initiation of micro-cracks at the early damage stage [13-16]. Acoustic and ultrasonic signals exhibit nonlinear features when the waves travel in a nonlinear medium. The growth of discontinuity in the materials is reflected by the increase of amplitudes of the nonlinear components. Kim *et al*. [17], Chen *et al*. [18]. and Mohseni *et al*. [19, 20] investigated higher harmonic generation performance due to the discontinuity of materials for damage detection. Besides, Leśnicki *et al*. [21], Chen *et al*. [22] and Carrión *et al*. [23] employed the impact excitation as the source of the signal and analysed resonance frequency shift to characterize alkali-silica reaction damage, sulphate attack and freeze-thaw cycle damage, and thermal damage, respectively. The other application of nonlinear feature to characterize damage is sideband. Many theoretical and experimental studies focused on sideband have been carried out in the literature, but they mainly focused on conventional vibro-acoustic technique.

There are two primary vibro-acoustic technique approaches the impact-modulation (IM) method and the vibro-modulation (VM) method. The IM method uses impact excitation to induce resonance vibration modes of structures, while the VM method uses harmonic excitation in the damage detection [24]. Chen *et al*. [25-27] investigated the evolution of concrete damage caused by mechanical load and chemical attack using the IM and the VM method. Also, they developed a non-contact VM method to assess thermal damage of cement-based materials. However, accurate determination of sideband frequencies through the IM method is difficult for concrete or concrete-related materials because the resonance modes of structures are usually not well separated. The sidebands of resonance frequencies are easily masked by noise or the

aliasing effect in signal processing. Furthermore, in the VM method, low-frequency signals are generally generated by electromagnetic shaker, and it causes a considerable burden for exciter to generate significant energy excitation at low-frequency. Also, the large oscillation caused by low-frequency signals will affect coupling conditions between transducers and structures.

1.2 Cross-modulated vibro-acoustic techniques

Zaitsev *et al*. carried out an experiment on a glass rod with thermally produced cracks to demonstrate the high sensitivity of the CMVA technique [28]. Tournat *et al*. conducted a series of experimental studies in a granular medium composed of glass beads to observe the cross-modulation effect. The results showed that sidebands are much more sensitive to weak perturbations of the medium [29]. In the study of Aymerich and Staszewski, the CMVA technique was applied to detect impact damage in composite laminates [30]. Trojniar *et al*. investigated fatigue cracks in the aluminium plate using the CMVA technique [31]. However, studies focused on the application of the CMVA technique on cement-based material have been very limited in the literature. The cement-based material is a more complex composite material compared with the glass and metal materials, and usually used in the larger-size structures. Therefore, the phenomena in the cement-based material utilizing the CMVA technique is different from the glass and metal materials. In the papers investigated CMVA techniques aforementioned, only one lower frequency is transferred from the pump wave to the carrier wave, and nonlinear parameter is only related to this transferred lower frequency and carrier frequency.

This study proposes and extends a cross-modulated vibro-acoustic (CMVA) technique to solve IM and VM limitation. Similar to the conventional VM method, CMVA technique relies on the interactions between a high-frequency carrier wave and a low-frequency harmonic vibration in the medium. Sidebands can be observed when the medium is discontinuous. The

difference between the CMVA technique and the conventional VM method is the low-frequency harmonic excitation. The VM method employs a single-frequency continuous sine wave as the low-frequency excitation signal, whereas in the CMVA technique, the low-frequency excitation signal is modulated by two excitation frequencies (f_{L1} and f_{L2}, f_{L1} is the resonance frequency and $f_{L1} < f_{L2}$). By employing modulated low-frequency pump signal, the proposed CMVA technique has the following advantages:

- Address the instrumental bottleneck frequency range, particularly for the ultra-low and/or low frequency. For full-scale structures, especially for civil engineering structures, the resonance frequencies are relatively low (in the order of Hertz). A modulated low-frequency pump signal, which contains not only resonance frequency (f_{L1}) but also a higher frequency excitation (f_{L2}), is used to induce such low-frequency resonance of these structures. Hence, actuators only need to transmit signal at f_{L2} instead of ultra-low or low frequency f_{L1}, meanwhile the sidebands related to f_{L1} can still be induced and measured.

- The required power of the actuator in generating a large enough magnitude of modulated pump signal is significantly less than that of using a single resonance frequency signal. This means the CMVA technique is more energy-efficient and practical in an actual application in civil engineering structures.

- Minimise attenuation of wave propagation while maintaining the sensitivity to micro-damages. The modulated pump signal at low frequency (f_{L1} and f_{L2}) could reduce the energy attenuation. But the wavelength at low frequency is large, and hence, it is insensitive to micro-damages. Although the high-frequency signal with a smaller wavelength can characterize small defects and cracks, the wave attenuates rapidly in the propagation. The CMVA technique combines a carrier signal at high-frequency (f_H) and

a modulated low-frequency pump wave (f_{L1} and f_{L2}) to enhance the applicability and sensitivity for NDT and SHM of civil engineering structures.

One of objectives of this paper is to quantitatively assess the accumulation damage in ultra-high-performance fibre-reinforced concrete (UHP-FRC) materials using the improved CMVA technique. Particularly, this study is expected to demonstrate both frequencies of pump wave (f_{L1} and f_{L2}) are transferred to the carrier wave (f_H) when there are cracks in the cement-based material. The other objective is to develop the theoretical framework and derive the equations for the improved CMVA technique. In addition, a nonlinear parameter D_α is then defined to provide the relationship between the amplitudes of sidebands and amplitudes of other frequency components, which allow evaluation of the damage. To validate and evaluate the performance of the improved CMVA technique, the results are compared with a conventional damage evaluation technique based on ASTM C215-02 [32]. The experimental results demonstrate that the nonlinear parameter is closely related to the damage and can be used as a sensitive and reliable indicator to detect and monitor structural damage in UHP-FRC.

2. Proposed methodology

Assuming that there is a gap distance d_0 due to initial defects or flexural loading between two rough surfaces, three incident longitudinal waves normally propagate to the interface, at which they separate into transmitted waves and reflected waves as shown in Fig.3-1. The displacement field between two rough interfaces caused by the wave interaction can be written as,

$$u(x,t) = \begin{cases} u_I(x-ct) + u_R(x+ct), & x < 0 \\ u_T(x-ct), & x > 0 \end{cases} \tag{3-1}$$

where c is the incident longitudinal wave speed, x is taken along the wave propagation direction. $u_I(x-ct)$, $u_R(x+ct)$ and $u_T(x-ct)$ are displacement of incident wave, reflected wave and transmitted wave, respectively.

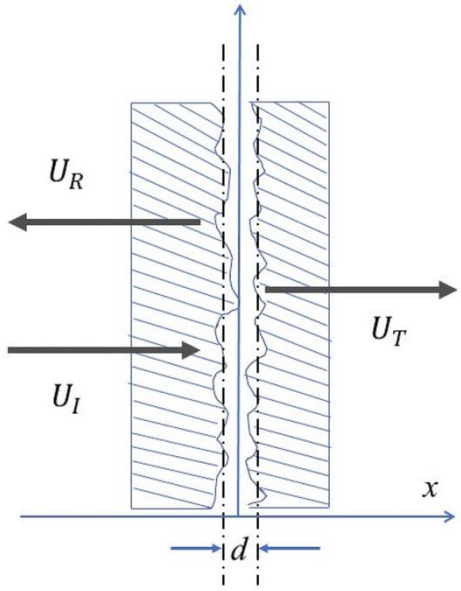

Fig.3-1 Longitudinal waves propagate through two rough interfaces

The incident wave leads to a dynamic opening-closing displacement on the rough interface and applying $u_I = A_1 cos[(\omega_1/c)(x-ct)] + A_2 cos[(\omega_2/c)(x-ct)] + A_3 cos[(\omega_3/c)(x-ct)]$, where A is the amplitude of wave and ω is the angular frequency, we have

$$\frac{d\xi(t)}{dt} = 2\sum_{i=1}^{3} A_i \omega_i sin\omega_i t - \frac{2K_1}{\rho c}\xi(t) + \frac{2K_2}{\rho c}\xi(t)^2 \tag{3-2}$$

where $(t) = \Delta d$, K_1 and K_2 are the first and second-order terms of stiffness, respectively. ρ is the density of the medium, and c is the velocity of the wave propagating in the medium. By solving Eq.(3-3), the linear solution $\xi_1(t)$ is found,

$$\xi_1(t) = \sum_{i=1}^{3} \frac{2A_i c\rho\omega_i}{\sqrt{4k_1^2 + c^2\rho^2{\omega_i}^2}} sin(\omega_i t - \theta_i) \tag{3-3}$$

$$cos\theta_i = \frac{2k_1}{\sqrt{4k_1^2 + c^2\rho^2{\omega_i}^2}}, \qquad sin\theta_i = \frac{c\rho\omega_i}{\sqrt{4k_1^2 + c^2\rho^2{\omega_i}^2}} \tag{3-4}$$

Thus we have nonlinear solution $\xi_2(t)$ including DC component, second-order harmonics and sidebands, respectively as follows:

(1) DC component: this part does not contain any trigonometric functions.

$$2\frac{K_2}{K_1}\sum_{i=1}^{3} \frac{A_i^2 c^2\rho^2{\omega_i}^2}{4k_1^2 + c^2\rho^2{\omega_i}^2} \tag{3-5a}$$

(2) Second order harmonics:

$$\sum_{i=1}^{3} \frac{2k_2 A_i^2 c^2\rho^2{\omega_i}^2}{\sqrt{k_1^2 + c^2\rho^2{\omega_i}^2}(4k_1^2 + c^2\rho^2{\omega_i}^2)} cos(2\omega_i t - 2\theta_i - \xi_i) \tag{3-5b}$$

$$cos\xi_i = \frac{k_1}{\sqrt{k_1^2 + c^2\rho^2{\omega_i}^2}}, \qquad sin\xi_i = \frac{c\rho\omega_i}{\sqrt{k_1^2 + c^2\rho^2{\omega_i}^2}} \tag{3-5c}$$

(3) Difference-sidebands: They are difference-sidebands with difference frequencies of $(\omega_1 - \omega_2)$, $(\omega_1 - \omega_3)$ and $(\omega_2 - \omega_3)$.

$$\frac{-8k_2 A_1 A_2 c^2\rho^2\omega_1\omega_2}{\sqrt{4k_1^2+c^2\rho^2{\omega_1}^2}\sqrt{4k_1^2+c^2\rho^2{\omega_2}^2}\sqrt{4k_1^2+c^2\rho^2(\omega_1-\omega_2)^2}} cos[(\omega_1 - \omega_2)t - (\theta_1 - \theta_2) - \delta_1] -$$

$$\frac{8k_2 A_1 A_3 c^2\rho^2\omega_1\omega_3}{\sqrt{4k_1^2+c^2\rho^2{\omega_1}^2}\sqrt{4k_1^2+c^2\rho^2{\omega_3}^2}\sqrt{4k_1^2+c^2\rho^2(\omega_1-\omega_3)^2}} cos[(\omega_1 - \omega_3)t - (\theta_1 - \theta_3) - \delta_2] - \tag{3-5d}$$

$$\frac{8k_2 A_2 A_3 c^2\rho^2\omega_2\omega_3}{\sqrt{4k_1^2+c^2\rho^2{\omega_2}^2}\sqrt{4k_1^2+c^2\rho^2{\omega_3}^2}\sqrt{4k_1^2+c^2\rho^2(\omega_2-\omega_3)^2}} cos[(\omega_2 - \omega_3)t - (\theta_2 - \theta_3) - \delta_3]$$

$$cos\delta_1 = \frac{2k_1}{\sqrt{4k_1^2 + c^2\rho^2(\omega_1 - \omega_2)^2}}, \qquad sin\delta_1 = \frac{c\rho(\omega_1 - \omega_2)}{\sqrt{4k_1^2 + c^2\rho^2(\omega_1 - \omega_2)^2}} \tag{3-5e}$$

$$cos\delta_2 = \frac{2k_1}{\sqrt{4k_1^2 + c^2\rho^2(\omega_1 - \omega_3)^2}}, \qquad sin\delta_2 = \frac{c\rho(\omega_1 - \omega_3)}{\sqrt{4k_1^2 + c^2\rho^2(\omega_1 - \omega_3)^2}}$$

$$cos\delta_3 = \frac{2k_1}{\sqrt{4k_1^2 + c^2\rho^2(\omega_2 - \omega_3)^2}}, \qquad sin\delta_3 = \frac{c\rho(\omega_2 - \omega_3)}{\sqrt{4k_1^2 + c^2\rho^2(\omega_2 - \omega_3)^2}}$$

(4) Sum-sidebands: They are sum-sidebands with sum frequencies of $(\omega_1 + \omega_2)$, $(\omega_1 + \omega_3)$ and $(\omega_2 + \omega_3)$.

$$\frac{8k_2A_1A_2c^2\rho^2\omega_1\omega_2}{\sqrt{4k_1^2+c^2\rho^2{\omega_1}^2}\sqrt{4k_1^2+c^2\rho^2{\omega_2}^2}\sqrt{4k_1^2+c^2\rho^2(\omega_1+\omega_2)^2}} sin[(\omega_1 + \omega_2)t - (\theta_1 + \theta_2) + \delta_4] +$$

$$\frac{8k_2A_1A_3c^2\rho^2\omega_1\omega_3}{\sqrt{4k_1^2+c^2\rho^2{\omega_1}^2}\sqrt{4k_1^2+c^2\rho^2{\omega_3}^2}\sqrt{4k_1^2+c^2\rho^2(\omega_1+\omega_3)^2}} sin[(\omega_1 + \omega_3)t - (\theta_1 + \theta_3) + \delta_5] + \quad (3\text{-}5f)$$

$$\frac{8k_2A_2A_3c^2\rho^2\omega_2\omega_3}{\sqrt{4k_1^2+c^2\rho^2{\omega_2}^2}\sqrt{4k_1^2+c^2\rho^2{\omega_3}^2}\sqrt{4k_1^2+c^2\rho^2(\omega_2+\omega_3)^2}} sin[(\omega_2 + \omega_3)t - (\theta_2 + \theta_3) + \delta_6]$$

$$cos\delta_4 = \frac{c\rho(\omega_1 + \omega_2)}{\sqrt{4k_1^2 + c^2\rho^2(\omega_1 + \omega_2)^2}}, \qquad sin\delta_4 = \frac{2k_1}{\sqrt{4k_1^2 + c^2\rho^2(\omega_1 + \omega_2)^2}}$$

$$cos\delta_5 = \frac{c\rho(\omega_1 + \omega_3)}{\sqrt{4k_1^2 + c^2\rho^2(\omega_1 + \omega_3)^2}}, \qquad sin\delta_5 = \frac{2k_1}{\sqrt{4k_1^2 + c^2\rho^2(\omega_1 + \omega_3)^2}} \quad (3\text{-}5g)$$

$$cos\delta_6 = \frac{c\rho(\omega_2 + \omega_3)}{\sqrt{4k_1^2 + c^2\rho^2(\omega_2 + \omega_3)^2}}, \qquad sin\delta_6 = \frac{2k_1}{\sqrt{4k_1^2 + c^2\rho^2(\omega_2 + \omega_3)^2}}$$

Combining DC component, second-order harmonics and sidebands of Eq.(3-5) to obtain expression of $\xi_2(t)$, and then from Eq.(3-6) the transmitted wave is found,

$$u_T(\psi) = \frac{K_2}{K_1}\sum_{i=1}^{3}\frac{A_i^2c^2\rho^2{\omega_i}^2}{4k_1^2+c^2\rho^2{\omega_i}^2} + \sum_{i=1}^{3}\frac{A_ic\rho\omega_i}{\sqrt{4k_1^2+c^2\rho^2{\omega_i}^2}} cos(\omega_i\psi - \theta_i) +$$

$$\sum_{i=1}^{3}\frac{2k_2A_i^2c^2\rho^2{\omega_i}^2}{\sqrt{k_1^2+c^2\rho^2{\omega_i}^2}(4k_1^2+c^2\rho^2{\omega_i}^2)} cos(2\omega_i\psi - 2\theta_i - \xi_i) - \quad (3\text{-}6)$$

$$\frac{8k_2A_1A_2c^2\rho^2\omega_1\omega_2}{\sqrt{4k_1^2+c^2\rho^2{\omega_1}^2}\sqrt{4k_1^2+c^2\rho^2{\omega_2}^2}\sqrt{4k_1^2+c^2\rho^2(\omega_1-\omega_2)^2}} cos[(\omega_1 - \omega_2)\psi - (\theta_1 - \theta_2) - \delta_1] -$$

$$\frac{8k_2A_1A_3c^2\rho^2\omega_1\omega_3}{\sqrt{4k_1^2+c^2\rho^2{\omega_1}^2}\sqrt{4k_1^2+c^2\rho^2{\omega_3}^2}\sqrt{4k_1^2+c^2\rho^2(\omega_1-\omega_3)^2}}cos[(\omega_1-\omega_3)\psi-(\theta_1-\theta_3)-\delta_2]-$$

$$\frac{8k_2A_2A_3c^2\rho^2\omega_2\omega_3}{\sqrt{4k_1^2+c^2\rho^2{\omega_2}^2}\sqrt{4k_1^2+c^2\rho^2{\omega_3}^2}\sqrt{4k_1^2+c^2\rho^2(\omega_2-\omega_3)^2}}cos[(\omega_2-\omega_3)\psi-(\theta_2-\theta_3)-\delta_3]+$$

$$\frac{8k_2A_1A_2c^2\rho^2\omega_1\omega_2}{\sqrt{4k_1^2+c^2\rho^2{\omega_1}^2}\sqrt{4k_1^2+c^2\rho^2{\omega_2}^2}\sqrt{4k_1^2+c^2\rho^2(\omega_1+\omega_2)^2}}sin[(\omega_1+\omega_2)\psi-(\theta_1+\theta_2)+\delta_4]+$$

$$\frac{8k_2A_1A_3c^2\rho^2\omega_1\omega_3}{\sqrt{4k_1^2+c^2\rho^2{\omega_1}^2}\sqrt{4k_1^2+c^2\rho^2{\omega_3}^2}\sqrt{4k_1^2+c^2\rho^2(\omega_1+\omega_3)^2}}sin[(\omega_1+\omega_3)\psi-(\theta_1+\theta_3)+\delta_5]+$$

$$\frac{8k_2A_2A_3c^2\rho^2\omega_2\omega_3}{\sqrt{4k_1^2+c^2\rho^2{\omega_2}^2}\sqrt{4k_1^2+c^2\rho^2{\omega_3}^2}\sqrt{4k_1^2+c^2\rho^2(\omega_2+\omega_3)^2}}sin[(\omega_2+\omega_3)\psi-(\theta_2+\theta_3)+\delta_6]$$

where $\psi = x - ct$. The acoustic distortion of sidebands in the transmitted wave is taken as the measurements in this study [33].

Cross-modulation effect takes place when two waves, namely low-frequency pump wave and high-frequency carrier wave, propagate in damage medium. In order to have clear labels to easily figure out the high frequency and low frequencies, the f_H represents high-frequency f_1 of the carrier wave. f_2 and f_3 of the low-frequency pump wave are transferred into f_{L1} and f_{L2} ($f_{L1} < f_{L2}$), respectively. In damage medium, sidebands occur at the frequencies of $f_H \pm nf_{L1}$, $f_H \pm nf_{L2}$ and $f_1 \pm nf_{L2} \pm nf_{L1}$ (where n = 1,2,3 …) as shown in Fig.3-2. In this study, interactions between f_{L1} and f_{L2} are omitted. Because f_{L1} and f_{L2} are not both frequencies of pump wave in which wavelengths are much larger than the size of flaws; hence interaction between these two frequencies do not contain much more information about defects and cracks. Sidebands at $f_H \pm nf_{L1}$ are not included in the nonlinear parameter for the reason that sidebands at $f_H \pm nf_{L1}$ from these experimental results are close to f_H to be easily masked by carrier wave component. With the damage accumulation, part of energy shifts to sidebands to make their amplitudes increase, and hence, the amplitude of sidebands can be

measured as a damaged indicator. A nonlinear parameter D_α can obtained from the relationship in Eq. (3-7):

$$D_\alpha \sim \frac{\sum A_{H\pm L2} + \sum A_{H\pm L2\pm L1}}{A_H A_{L2}} \tag{3-7}$$

where $\sum A_{H\pm L2}$ and $\sum A_{H\pm L2\pm L1}$ are the sum of sideband amplitude at frequencies of $f_H \pm nf_{L2}$ and $f_H \pm nf_{L2} \pm nf_{L1}$, respectively. A_H and A_{L2} is the spectral amplitude of carried wave and dominant pump frequency, respectively. f_{L2} is usually observed in experiments to be dominant pump frequency.

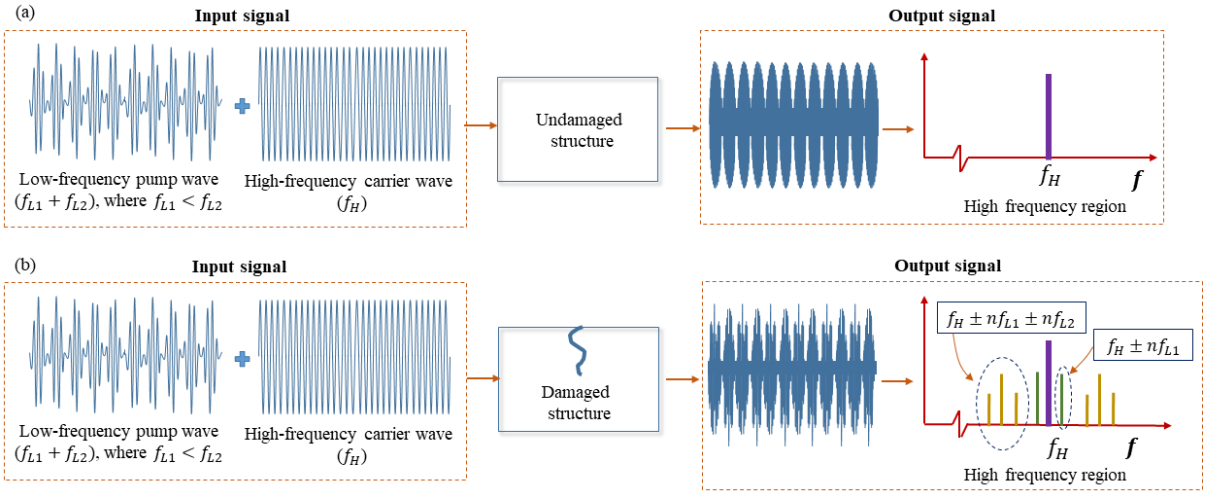

Fig.3-2 Schematic diagram of the CMVA technique: (a) undamaged structure, (b) damaged structure

3. Specimen preparation and damage generation

3.1 Specimens

The UHP-FRC was prepared using the sulphate resisting cement, silica fume, sand and steel fibre. The 28-day compressive strength of sulphate resisting cement is 60MPa. The bulk density of the uncondensed silica fume is 635kg/m^3 and silicon dioxide (SiO_2) content is over 89.6%. They were used as mineral admixture. Natural washed river sand, with the maximum nominal particle size of 4mm was used as fine aggregate. A polycarboxylic ether based superplasticizer

was added into the mix to achieve a better workability for UHP-FRC. Straight and hooked steel fibres with the aspect ratio of 0.65 were added into mix as micro and macro fibre. The detailed properties of these two types of fibre are listed in Table 3-1. The proportions of the various ingredients of UHP-FRC in this study are shown in Table 3-2. Four UHP-FRC specimens (100mm×100mm×500mm) were cured in a standard curing environment (23°C and 95% relative humidity) for 90 days after demolding, and they were labelled as A1, A2, B1 and B2, respectively.

Table 3-1 Properties of fibres

Type of fibre	Diameter (mm)	Length (mm)	Aspect ratio	Tensile strength (MPa)	Young's modulus (GPa)
Micro fibres: Straight	0.20	13	0.65	2850	210
Hook end Dramix 3D-65/35 BG	0.55	35	0.65	1345	210

Table 3-2 Mix proportion of the UHP-FRC specimens

Ingredients	Type	Weight ratio
Cement	Sulphate resisting	1.000
Silica Fume	Uncondensed	0.266
Sand	Natural washed river sand	1.000
Water	-	0.165
Superplasticizer	Polycarboxylic ether based	0.038
Micro fibre	Micro fibres: Straight	0.155
Macro fibre	Hook end Dramix 3D-65/35 BG	0.052

3.2 Three-point flexural test

There are two groups of specimens in this study. The first group of UHP-FRC specimens (labelled as A-series) was loaded directly without pre-treatment. The specimen A1 and A2 were the same. For the other group of UHP-FRC specimens (labelled as B-series), a notch was artificially created at mid-length of specimens before flexural test. The sizes of the notches in specimens B1 and B2 are 7mm×2mm, and 7mm×4mm (width×depth), respectively. The universal testing machine was used and the loading rate was 0.4mm/min. The testing machine was stopped when the loading applied on the specimens reached 30kN. The specimens were then taken out for evaluation using the proposed CMVA technique and standard dynamic

elastic modulus test. This loading process was repeated three times. After three loading cycles, the specimen was loaded beyond 30kN until it reaches its ultimate flexural strength. Different levels of damage were induced the UHP-FRC specimens in these loading processes. From the intact state to final loading state, there are five states designated as intact state, state 1, state 2, state 3 and state 4, respectively. A camera with microscope control mode and LED light was used as crack detector to record the surface cracks created on these UHP-FRC specimens. The growth of cracks is shown in Fig.3-3.

The flexural strength of UHP-FRC specimen is obtain by Eq. (3-8) [34].

$$\sigma_b = \frac{3P_{max}L}{2b(h-a_0)^2} \tag{3-8}$$

where P_{max} is the maximum load; b and h are width and height of specimens, respectively. a_0 is notch depth, and L is the span length. It should be noted that specimens marked A- presents the specimen without notch whereas the B- specimens were introduced notches. In order to better explore the effect of notch with different depth, B1 and B2 refer to specimen with notch depth of 2mm and 4mm, respectively. Additionally, the flexural strength of UHP-FRC specimens were showed in Table 3-3.

Table 3-3 Flexural strength of UHP-FRC specimens

Specimen	L (mm)	b (mm)	h (mm)	a_0 (mm)	P_{max} (kN)	σ_b (MPa)
A1	360	100	100	-	49.88	26.94
A2				-	34.28	21.46
B1				2	38.16	23.44
B2				4	40.01	18.51

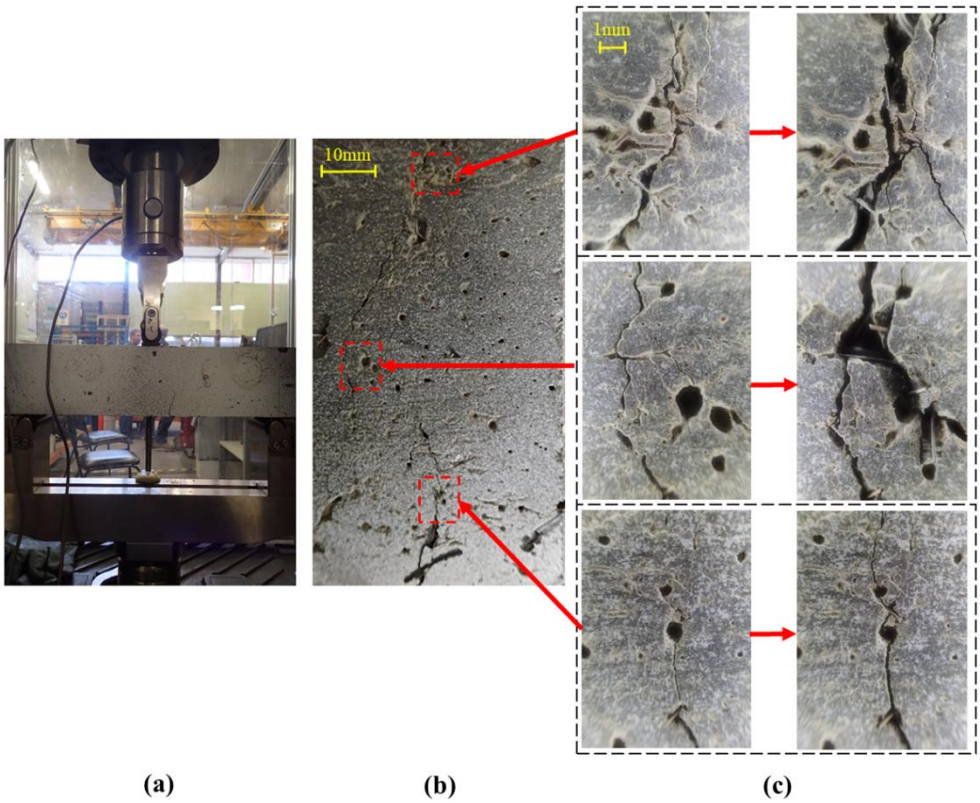

Fig.3-3 Cracks of specimen B2 under different levels of loadings, (a) flexural test in progress; (b) bottom surface of the specimen; (c) growth of cracks from state 3 (on the left side) to state 4 (on the right side)

4. Experimental procedure and signal processing

4.1 Selection of modulated pump wave frequencies in CMVA technique

To maximize the interaction between vibro-acoustic wave and cracks, experimental modal analysis was performed to obtain the resonant frequencies of UHP-FRC. Then f_{L1} and f_{L2} were selected from resonant response in frequency domain according to the amplitudes.

Although frequency responses slightly shifted when the damage was accumulated, these two selected frequencies were still applied throughout entire evaluation using CMVA technique. Firstly, modulation effect was not obvious at early states, particularly at intact state, therefore these frequencies were selected at intact state to ensure adequate modulated interaction by exciting structural response with large enough magnitude. Secondly, modulation effect was evident by observing the increasing amplitude of sidebands at later damage states.

Although the selected frequencies were not structural resonance frequencies, which have frequency shifts caused by the damage, excitation of structural response was still sufficient. The selected frequencies were the same for all CMVA tests for the purpose of controlling experimental variables and allow comparison of the results. In addition, it is laborious to obtain exact structural resonances from field measurements, so the arbitrary frequency selection is more practical for real applications. These two selected frequencies indirectly demonstrate that arbitrary frequency selection can ensure the CMVA technique have a good performance.

It should be noted that the locations of struck and accelerometer in this test is different from the standard resonant frequency test in Section 4.3. In this test to find the two frequencies of the pump wave of the CMVA technique, the location of the accelerometer was the same as receiving transducer used in CMVA experiments. The location of the struck was also at the same position as the electromagnetic vibration exciter set-up in the CMVA experiments.

The frequency response of specimen A1 is shown in Fig.3-4. There are four vibration modes at 243.1Hz, 428.8Hz, 821.2Hz and 1007Hz, respectively. In this study, 240Hz and 1000Hz were selected as frequencies of modulated pump wave for the following reasons:

- It has better control of the resonance vibration. When the electromagnetic vibration shaker emits signal with frequency exactly the same with structural resonance response, intensive vibration is in structures. However, intensive vibration affects robustness of contact condition between transducers and specimens. Therefore, the frequency responses with appropriate amplitude are chosen in this study. The amplitudes at 243.1Hz and 1007Hz are close to 0.018 and they are more suitable compared to the large amplitudes at 428.8Hz and 821.2Hz.
- The difference between f_{L1} and f_{L2} should be large enough, otherwise, sidebands are masked by each other. Therefore, 243.1Hz and 1007Hz were chosen in this study

because the difference between 243.1Hz and 1007Hz is larger than the difference between any other two frequency responses.

- It is effective to reduce the resolution requirement. The frequency resolution is defined as $\Delta f = f_s/N$, where f_s is sampling frequency and N is number of data points. If selected frequencies are kept on one decimal place, then Δf should also be accurate to one decimal point by decreasing sampling frequency. Thus, instruments with high-resolution are required and it is possible to prevent further application of CMVA technique. Hence 243.1Hz and 1007Hz are simplified into 240Hz and 1000Hz, respectively.

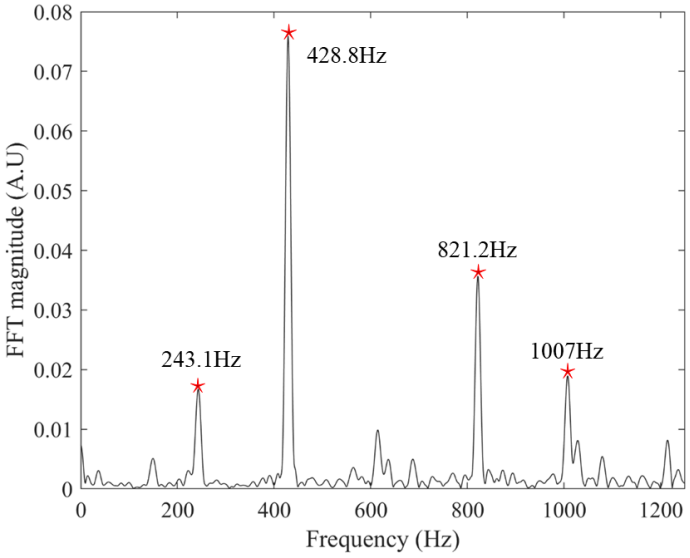

Fig.3-4 Frequency response for specimen A1

4.2 Set-up of the CMVA technique

The experimental set-up of the proposed CMVA technique is shown in Fig.3-5. A modulated continuous sinusoidal signal with frequency of 1kHz and 240Hz was first generated by signal generator and used as low-frequency pump wave. It was then fed into a power amplifier before feeding into electromagnetic vibration exciter. To suppress attenuation of ultrasonic wave

propagating in UHP-FRC, 50kHz was selected as frequency of carrier wave. Thus, a continuous sinusoidal signal at 50kHz was generated by a function generator and then transmitted into a emitting transducer. The peak-to-peak voltage of the pump wave remains the same during the experiments while the peak-to-peak voltage of the carried wave was progressive increasing with a steady rate. A total of ten voltage levels were used to calculate one nonlinear parameter, and this procedure was repeated three times to avoid measurement errors in the experiment. Pump wave and carrier wave propagate in UHP-FRC specimens and were captured by the receiving transducer. The signal modulated by pump wave and carried wave was recorded by digitizer for further signal processing and analysis. Two transducers were coupled with UHP-FRC specimens using vacuum grease to ensure a smooth and robust contact between the transducers and specimens. Additionally, the electromagnetic exciter and emitting transducer were located at a distance of 50 mm and 70 mm from one end of the specimens, respectively. While the other receiving transducer was located at 50 mm from the other side of the specimens.

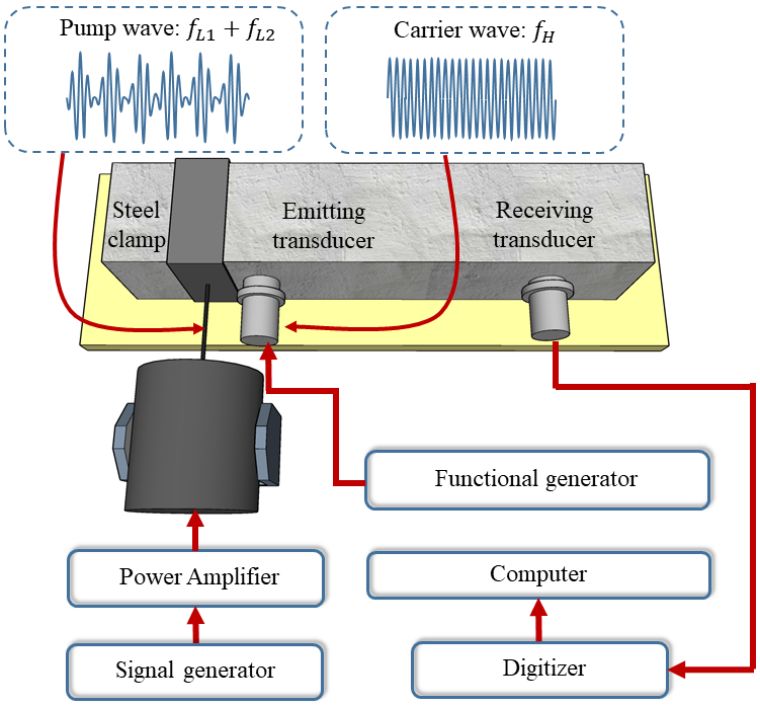

Fig.3-5 Experimental set-up of CMVA technique

4.3 The dynamic Young's modulus of elasticity E_d

To further characterize the damage levels of the UHP-FRC specimens and compare the results of the proposed CMVA technique with the conventional dynamic elastic modulus tests using the impact resonance method shown in ASTM C215-02. Ten measurements of longitudinal resonant frequency were obtained at each damage stage for each specimen and the averaged values were calculated.

4.4 Extraction of nonlinear parameter

The measured time domain signal and frequency spectrum of specimen A2 are shown in Fig.3-6. Fast Fourier transform (FFT) was used to transform the signal from time domain into frequency domain. Fig.3-6 shows that sidebands mainly appear at frequencies of (50kHz ± n×1kHz) and 50kHz ± (n×1kHz ± m×0.24kHz), and the prominent amplitudes were obtained in first and second order sidebands (n=1, 2, and m=1). Some other higher order sidebands were omitted when calculating nonlinear parameters of the CMVA technique in this study, including the sidebands at (50kHz ± m×0.24kHz) because they are too close to the main high-frequency component at 50kHz, which can be easily masked. Finally, the sidebands at 47.76kHz, 48kHz, 48.24kHz, 48.76kHz, 49kHz, 49.24kHz, 50.76kHz, 51kHz, 51.24kHz, 51.76kHz, 52kHz and 52.24kHz were used in the calculation of $\sum A_s$.

According to Eq.(3-8), nonlinear parameter D_α is defined as the slope of data points ($\sum A_s$, $A_H A_{L2}$) under ten peak-to-peak voltage levels. Fig.3-7 shows a linear relationship of $\sum A_s$ and $A_H A_{L2}$ for the specimen A1 under five different damage levels, with high coefficients of determination (R^2≥0.95).

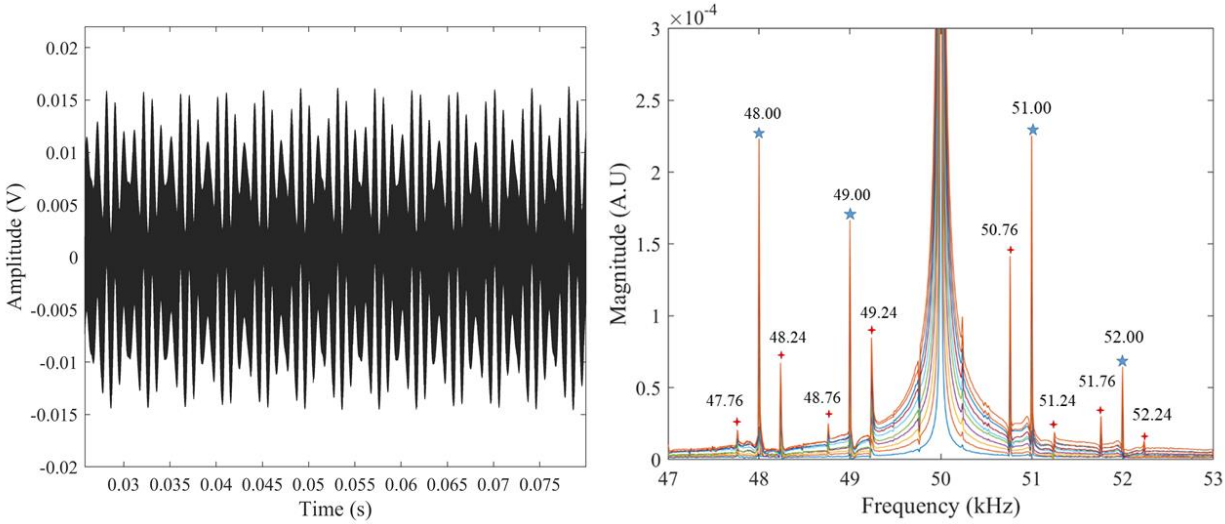

Fig.3-6 Typical signal of modulation wave: (a) time domain; (b) frequency domain

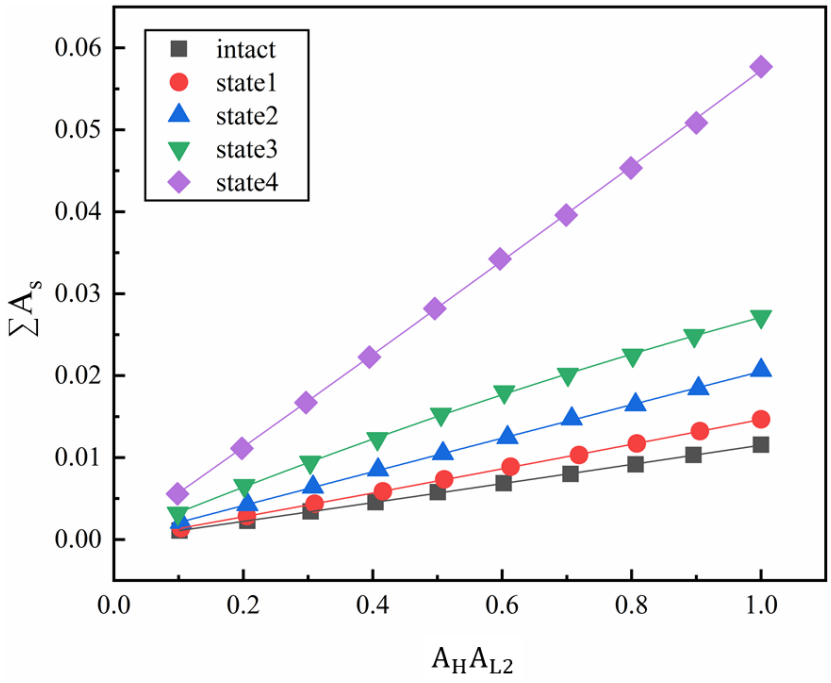

Fig.3-7 Nonlinear parameter of specimen B2 in different state (Linear relationship of $A_H A_{L2}$ and $\sum A_s$)

5. Results and discussions

5.1 Results of fundamental longitudinal resonant frequencies

The elastic modulus has been widely used as indicator in conventional techniques to characterize defects in structures. In this study, the fundamental longitudinal resonant frequencies of the four specimens at five different states were measured for calculating dynamic Young's modulus of elasticity. The results are shown in Fig.3-8, where the maximum magnitudes are normalized to allow direct comparison. The fundamental longitudinal resonant frequencies are slightly shifted toward to low frequency. The largest shift happens between state 3 to state 4 because the specimens were loaded to its ultimate damage strength instead of applying a steady loading step of 30kN. It should be noted that the frequency domain of specimen B2 is slightly different to the other three specimens because the coupling mode occurred. Besides of resonant frequency response, there was another distinguish frequency components, and these extra responses were caused by coupling mode. It sometimes happens when the structures have evident cracks. Specimen B2 has the largest depth of notch. The cracks of this specimen were obvious after loading test. This coupling mode causes a serious issue. When the damage grows with the loading cycle, more energy is transferred from the fundamental resonant mode to the coupling mode. When the damage reaches certain level, it is difficult to identify the fundamental resonant vibration mode from coupling mode based on the magnitude. Thus, the conventional dynamic elastic modulus test is not reliable and robust due to the coupling effect.

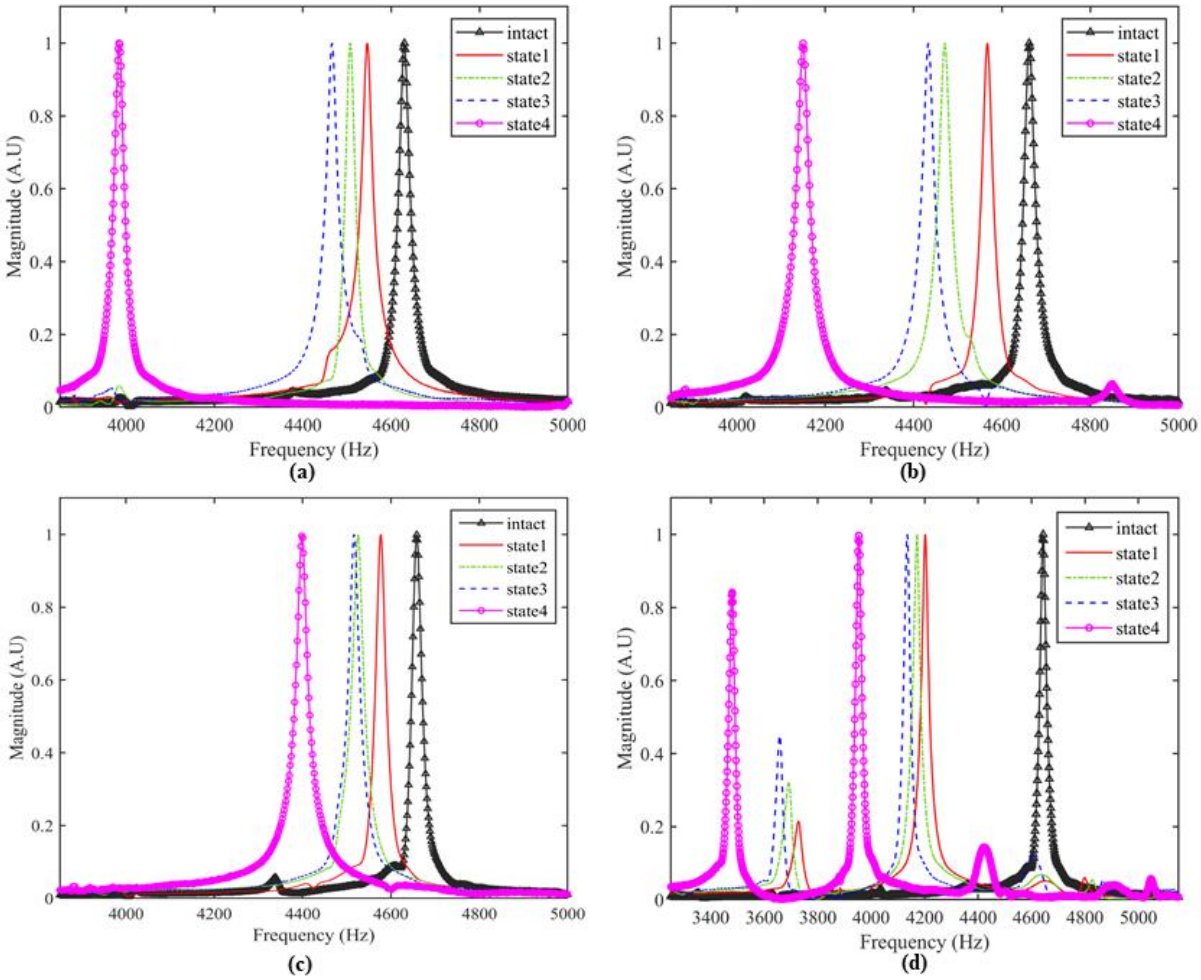

Fig.3-8 Fundamental longitudinal frequencies at different damage level: (a) specimen A1; (b) specimen A2; (c) specimen B1; (d) specimen B2

5.2 Results of dynamic elastic modulus test

After obtaining fundamental longitudinal frequency, the dynamic elastic modulus E_d can be calculated using Eq.(3-9):

$$E_d = 4\frac{L'}{bh}Mf_l^2 \tag{3-9}$$

where L', b and h are length, width and height of specimens, respectively. M is mass and f_l is fundamental longitudinal frequency.

The results of E_d for specimen A1, A2, B1 and B2 at different state are shown in Fig.3-9. The initial value of E_d for these four specimens are different at intact state. In terms of

magnitude of resonant frequency, the ranking for the value E_d from largest to smallest within the set of specimens is presented as A2, B1, A1 and B2. This order for the values of E_d differs completely when compared to the order from largest to smallest for the values of σ_b within the same set of specimens. The initial value of E_d indirectly reflects the flexural properties of specimens, therefore, it indicates that E_d is not very reliable, to some extent, to assess the mechanical properties of UHP-FRC structures according to these experimental results.

Fig.3-9(a) and 3-9(b) show the results of A-series specimens and the results of these two groups of specimens exhibit almost the same trend of decrease. For specimen A1, the relative percentage change from state 1 to state 4 is about 3.60%, 6.61%, 9.69% and 27.16%, respectively. Meanwhile, relative change ratios are 4.02%, 9.38%, 10.88% and 22.02% for the four different damage states of specimen A2, respectively. The trends of E_d of A-series specimens are only slightly decreasing, which indicates the conventional dynamic elastic modulus test is not very sensitive for crack formation and grow.

Fig.3-9(c) and 3-9(d) show the results of E_d for B-series specimens. The value of E_d for specimens B1 and B2 decrease with accumulation of damage in different states. This group of specimens have a notch at mid-span of the specimens to control the formation of the cracks, such as location and type. It is expected that the concentrated cracks initially occur at the middle of bottom surface in B-series specimens, whereas distributed small cracks appear at the locations of two supports in A-series specimens. However, the decreasing trend of the results of specimen B1 is similar to that of A-series specimens. The possible reason is that the size of notch (100mm length×7mm width×2mm depth) of specimen B1 is not large enough. Relative percentage changes for specimen B1 are 3.58%, 5.73%, 6.10% and 12.15%, respectively. The formation of crack in specimen B2 is expected where a small visual crack initially appeared in the middle of bottom surface, and gradually developed as a large dominant crack. The percentage change from intact state to state 1 of specimen B2 is about 18.08% and this is quite

large compared with the other three specimens. It is believe that this is caused by the support conditions of the specimens (see ASTM C215-02 Fig.3(b)) and the size of notch.

According to the analysis of E_d of four UHP-FRC specimens at different states, it is found that the conventional dynamic elastic modulus test is insensitive to characterize evolution of cracks. Furthermore, it is not easy to clearly identify resonant frequency when coupling modes occur. In addition, robustness and consistency of this dynamic elastic modulus test are frequently affected by support conditions and geometry of specimens.

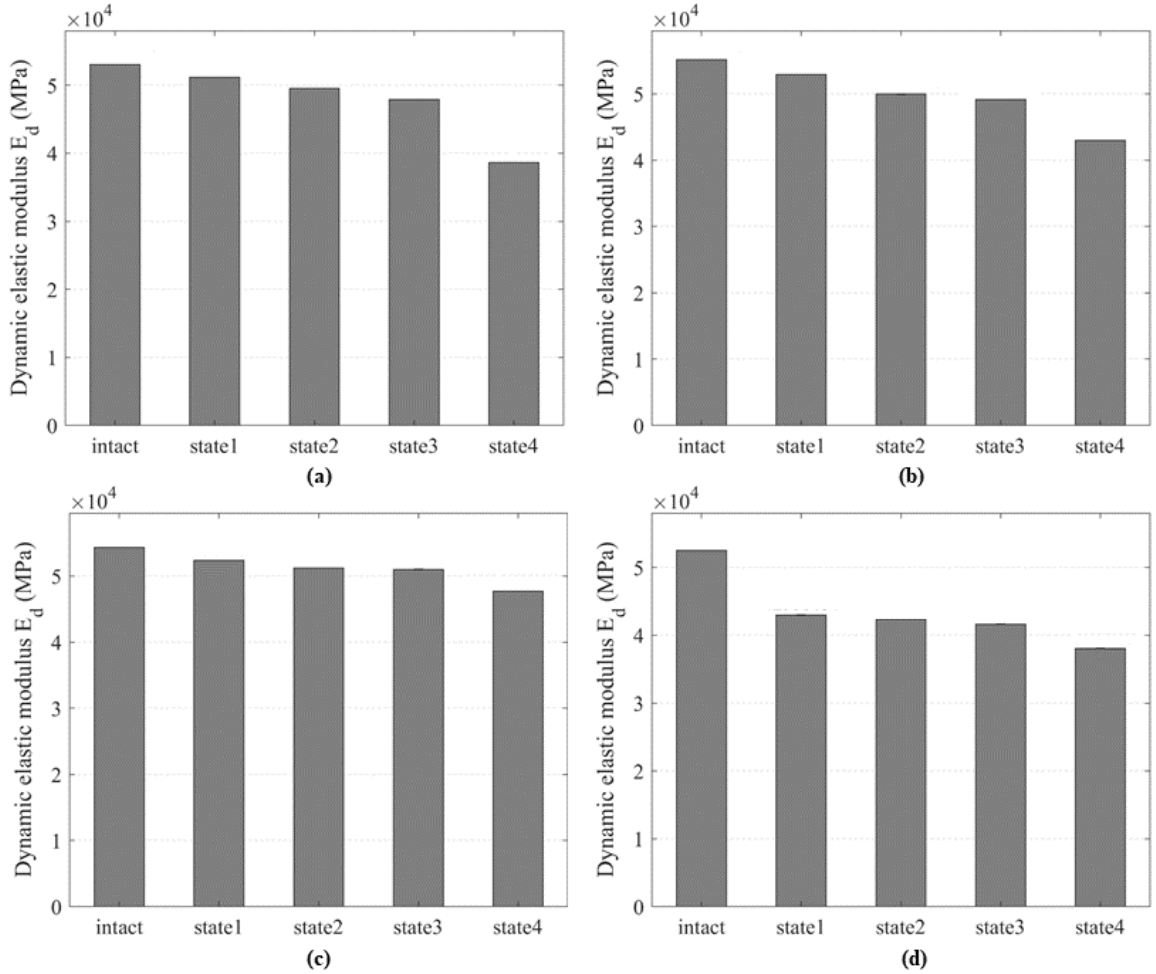

Fig.3-9 Dynamic elastic modulus: (a) specimen A1; (b) specimen A2; (c) specimen B1; (d) specimen B2.

5.3 Results of using CMVA technique

In this section, the results of using CMVA technique, 1) typical frequency domain at five different states, and 2) nonlinear parameter D_α, are presented. Fig.3-10 shows the frequency domain data of specimen B2 at state 1, state 2, state 3 and state 4, respectively. The sidebands shown in Fig.3-10(a) for state 1 mainly occur at the frequency of (50 ± n×1) kHz, i.e. 48kHz, 49kHz, 51kHz, and 52kHz. The amplitudes of these sidebands are small. At state 2, as shown in Fig.3-10(b), sidebands at frequencies (50 ± n×1)kHz still play a dominant role and the magnitudes slightly increase.

There are some other sidebands at the frequencies of 50 ± (n×1 ± m×0.24)kHz, such as 47.76kHz, 48.24kHz, 48.76kHz, 49.24kHz, 50.76kHz, 41.24kHz, 51.76kHz, 52.24kHz. In Fig.3-10(c), the magnitudes of the sidebands at (50 ± n×1)kHz and 50 ± (n×1 ± m×0.24)kHz generally increase. Fig.3-10(d) shows that, in state 4, the number and the magnitudes of the sidebands increase evidently. Some higher order sidebands, where n≥3, m≥2, occur in frequency domain and the magnitude of these sidebands increase obviously. As mentioned in Section 4.4, the sidebands at specified frequencies are considered in the calculation of nonlinear parameter. Even though some sidebands are ignored, the nonlinear parameter still has high sensitivity in characterizing different levels of damage.

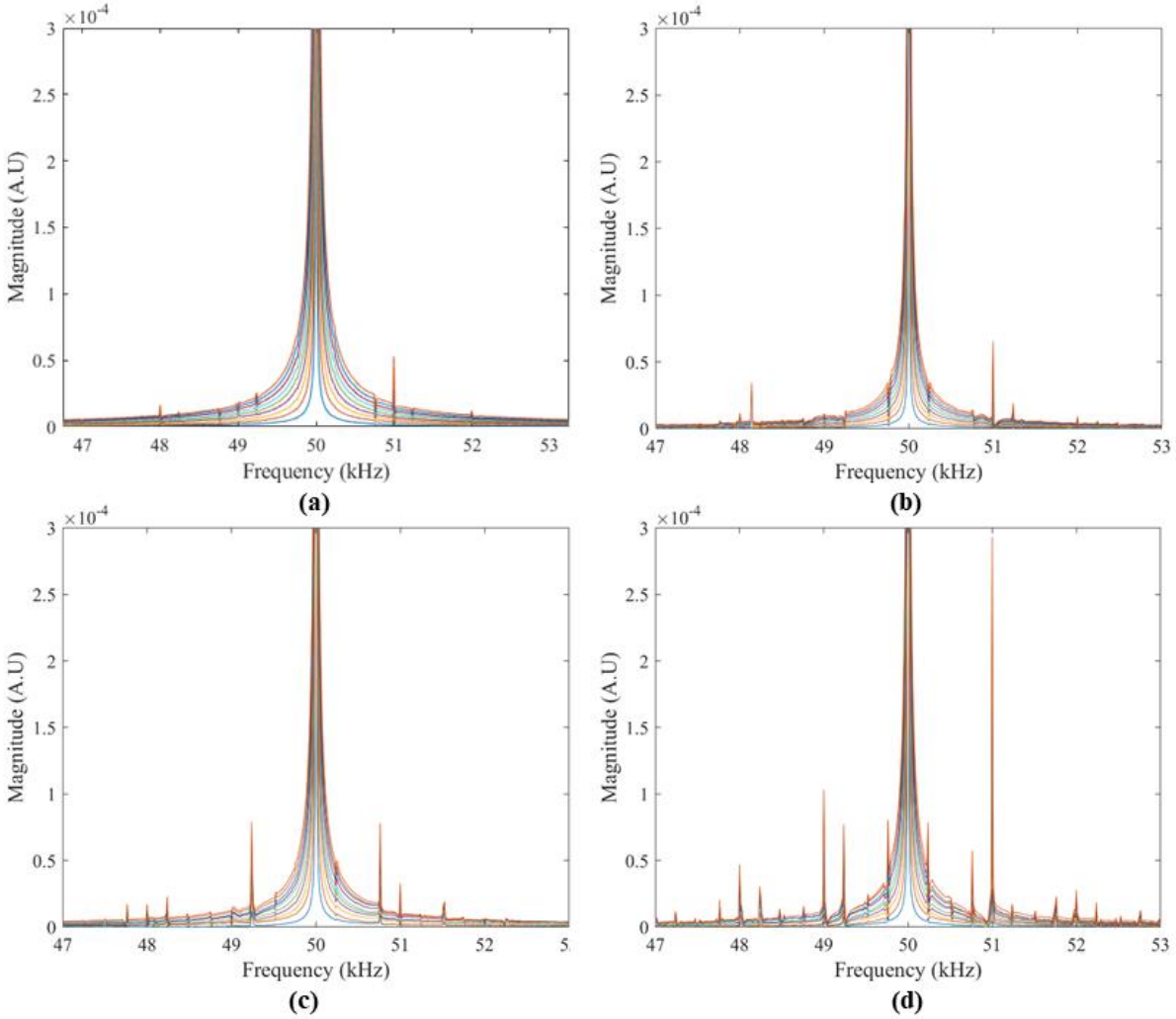

Fig.3-10 Frequency domain signal for specimen B2: (a) state1; (b) state2; (c) state3; (d) state4.

Nonlinear parameters D_α are calculated using Eq.(3-7) and presented with error bar in Fig.3-11. It is observed that nonlinear parameters of these four UHP-RFC specimens at intact state are not zero because of the inherent defects caused during casting and curing procedure. Therefore, the nonlinear parameter D_α can be used to identify not only crack-induced damage, but also material nonlinearity. Formation of inherent defects is unavoidable, and the inherent defects are slightly different even in the same batch of specimens made by the same materials and production process. These inherent defects reduce the mechanical strength of the specimens to some extent. Among the initial nonlinear parameters D_α of these four specimens, the minimum value of D_α is 0.0096 (specimen A1), followed by 0.0104 (specimen A2), 0.0106

(specimen B1), and 0.0108 (specimen B2). The order of these nonlinear parameters is similar to that of σ_b, which reveals that the nonlinear parameter D_α is a feasible calibre for qualitative assessment of initial state of materials, and provide implication of mechanical strength of the specimens.

Fig.3-11 shows that the nonlinear parameters present a rapid growth with the accumulation of damage. From intact state to state 1, the nonlinear parameter D_α increases about 50% for specimen A1 and 63% for specimen A2, whereas it increases about 25% and 28% for specimen B1 and specimen B2, respectively. In comparison with B-series specimens, A-series specimens have more growth after first loading cycle. It is because A-series specimens without pre-treatment of notch have some small distributed cracks at two supporting points at the beginning, and the contribution of distributed cracks appeared in multiple areas is more evident than single concentrated crack occurred at one position. Furthermore, it is observed that the geometric change of notch almost has no influence on the nonlinear parameter because the nonlinear parameter does not have a significant growth for B-series specimens from the intact state to the state 1. These experimental results demonstrate the excellent ability of nonlinear parameter in characterizing damage because it only reflects the internal changes of the specimens and is not affected by geometric changes, such as boundary conditions. Moreover, the initial nonlinear parameter D_α of specimen B1 is larger than that of specimen B2. This variation is reasonable because the notch of specimen B1 is small, therefore, its damage accumulation progress is similar to A-series specimens.

Based on the results, the increasing trend of nonlinear parameter D_α is obviously shown in Fig.3-11. Considering the A-series specimens, the relative change ratios of specimen A1 from state 1 to state 4 are about 50.00%, 110.42%, 212.85% and 330.56%, respectively. For specimen A2, the relative change ratios are 63.02%, 107.72%, 199.39% and 422.96% for state 1 to state 4. In the result of A-series specimens, the minimum increase of D_α is 50%, which is

larger than the maximal increase of E_d (about 27.16%) in the final state. Fig.3-11(a) and 11(b) show the nonlinear parameters D_α of B-series specimens. The increase of D_α for specimen B1 is slightly lower than that of specimen B2, and the overall increase slower compared with specimen B2. Similar trend of E_d is also observed in specimen B1, and the results are related to its damage evolution. The relative change ratios from state 1 to state 4 are still substantial for specimen B2, and they are 24.76%, 76.03%, 124.54% and 198.52%, respectively. D_α of specimen B2 has a trend of rapid growth, and relative change ratio from state 1 to state 4 is 28.00%, 86.77%, 139.69% and 410.46%, respectively.

The results of initial D_α indicate that CMVA technique is capable to characterize material nonlinearity. Furthermore, these values of nonlinear parameter D_α are consistent regardless of geometric changes caused by the notch. Compared with results of dynamic elastic modulus E_d, the nonlinear parameter D_α has high sensitivity to evolution of the cracks in UHP-FRC materials.

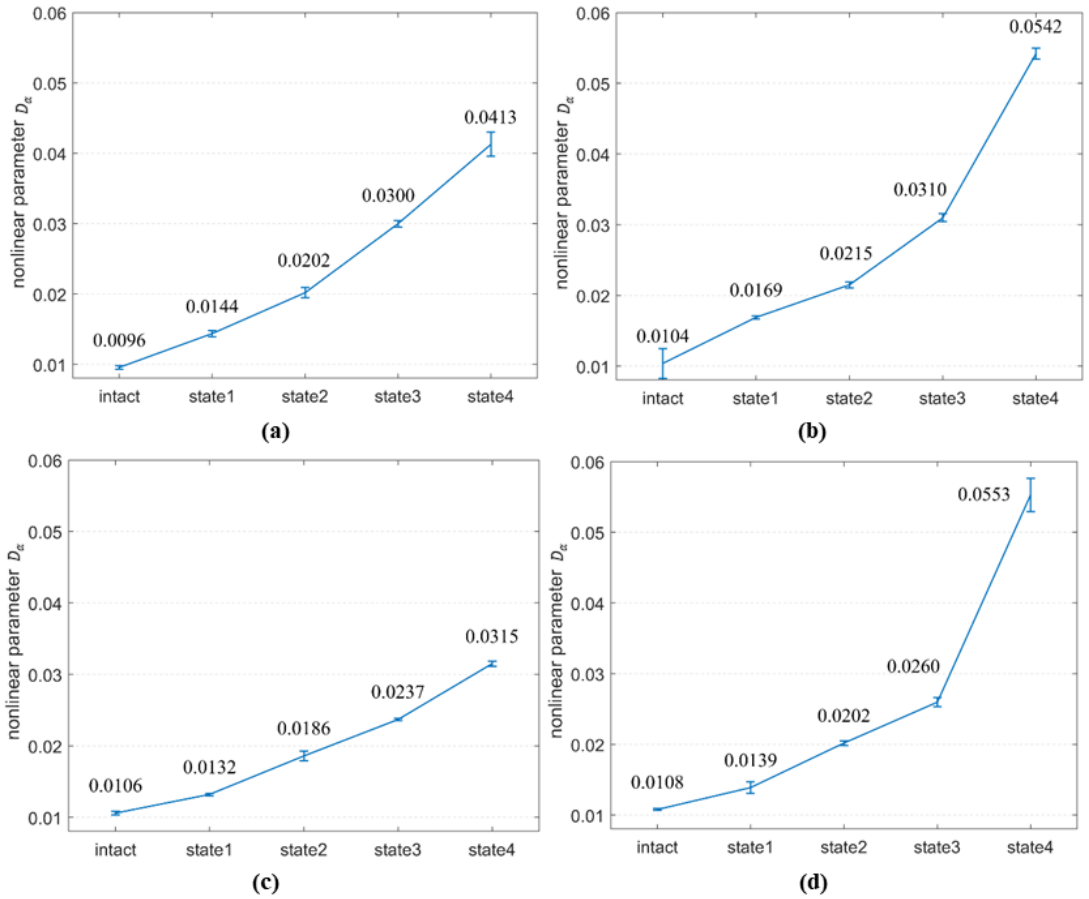

Fig.3-11 Nonlinear parameter D_α: (a) specimen A1; (b) specimen A2; (c) specimen B1; (d) specimen B2.

5.4 Comparison of nonlinear parameter and dynamic elastic modulus

Along with accumulation of damages, the nonlinear parameter D_α increases while the dynamic elastic modulus E_d decreases. In addition, the unit and order of magnitude are also different. In order to evaluate and compare the sensitivity of D_α and E_d, dimensionless indexes are defined:

$$\bar{D}_\alpha = |(D_\alpha - D_0)|/D_0 \tag{3-10}$$

$$\bar{E}_D = |(E_D - E_0)|/E_0 \tag{3-11}$$

where E_0 and D_0 correspond to the data at intact state. $\overline{D}_\alpha$ and $\overline{E}_D$ are dimensionless indexes corresponding to the D_α and E_d, respectively, as shown together in Fig.3-12.

From Fig.3-12, the variation of $\overline{D}_\alpha$ is 3.306, 4.230, 2.286 and 4.105 corresponding to A1, A2, B1 and B2, respectively, while the largest variation of $\overline{E}_D$ is not more than 0.3. Along with the accumulation of damages, the $\overline{D}_\alpha$ has shaper rise than $\overline{E}_D$. Additionally, the $\overline{D}_\alpha$ is generally one order of magnitude higher than the corresponding changes of $\overline{E}_D$. This outcomes implies that the CMVA technique has a much higher sensitivity to the damages than the conventional linear measurements.

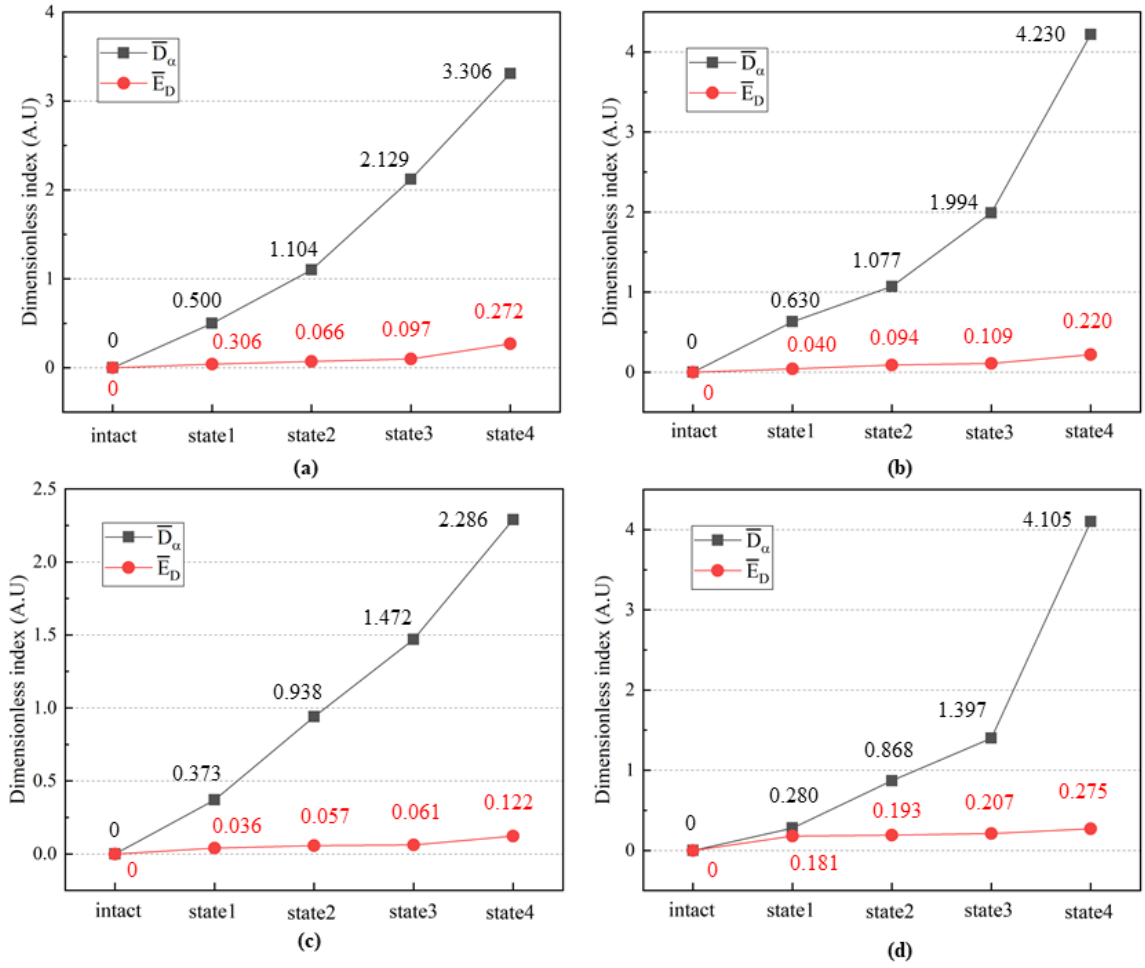

Fig.3-12 Comparison of $\overline{D}_\alpha$ and $\overline{E}_D$: (a) specimen A1; (b) specimen A2; (c) specimen B1; (d) specimen B2.

6. Conclusions

This study has developed a CMVA technique to evaluate the damage evolution in UHP-FRC materials under flexural loading using nonlinear parameter D_α. The results have shown that the CMVA technique is feasible for characterizing bending damage and evaluating the damage growth. The proposed CMVA technique is based on two independent waves, namely, low-frequency pump wave and high-frequency carrier wave. The technique has advantages of applying modulated pump wave with frequency f_{L1} and f_{L2} to arouse resonance frequency, maintaining robust contact condition between the transducers and specimens, and also avoiding the need of high-power electromagnetic shaker. The cross-modulation effect due to interaction between pump wave and carrier wave could be observed in frequency domain. The number and amplitude of sidebands increase with the accumulation of damage. In this study, the nonlinear parameter D_α has been developed and used as an indicator for evaluating bending damage. The nonlinear parameter D_α increases during the entire course of flexural test, particularly at early damage state.

The proposed CMVA technique is reliable compared to conventional ASTM technique. The results of conventional ASTM technique are usually affected by experimental conditions and manufacturing process of samples, and the resonance frequency can be masked by coupling modes. However, the measurement procedure of the proposed CMVA technique is robust to be used in field applications. The proposed CMVA technique has high sensitivity for detecting cracks in UHP-FRC materials compared to conventional ASTM technique. The nonlinear parameter D_α has a maximum relative change ratio of 422.96%, while the change of dynamic elastic modulus E_d is only about 27.48%.

In this study, the feasibility, reliability and sensitivity of the proposed CMVA technique have been validated and demonstrated. With the increasing applications of UHP-FRC

materials, the development of damage detection techniques for UHP-FRC material has attracted significant attention. This study has shown that the proposed CMVA technique is an effective method for detecting and identifying cracks in UHP-FRC materials, and can be potentially used for field applications.

Acknowledgement

This research is supported by China Scholarship Council (CSC). The authors are appreciated suggestions from Dr. Chengfeng Fang for experimental work and discussions with James Vidler for theoretical work.

References

1. Guo, Z., *Principles of reinforced concrete*. 2014: Butterworth-Heinemann.
2. Naebe, M., M.M. Abolhasani, H. Khayyam, A. Amini, and B. Fox, *Crack damage in polymers and composites: A review.* Polymer reviews, 2016. **56**(1): p. 31-69.
3. Lacouture, J.-C., P.A. Johnson, and F. Cohen-Tenoudji, *Study of critical behavior in concrete during curing by application of dynamic linear and nonlinear means.* The Journal of the Acoustical Society of America, 2003. **113**(3): p. 1325-1332.
4. Hughes, J.M., M. Mohabuth, A. Khanna, J. Vidler, A. Kotousov, and C.-T. Ng, *Damage detection with the fundamental mode of edge waves.* Structural Health Monitoring, 2021. **20**(1): p. 74-83.
5. Tsioulou, O., A. Lampropoulos, and S. Paschalis, *Combined non-destructive testing (NDT) method for the evaluation of the mechanical characteristics of ultra high performance fibre reinforced concrete (UHPFRC).* Construction and Building Materials, 2017. **131**: p. 66-77.

6. Nematzadeh, M., M. Tayebi, and H. Samadvand, *Prediction of ultrasonic pulse velocity in steel fiber-reinforced concrete containing nylon granule and natural zeolite after exposure to elevated temperatures.* Construction and Building Materials, 2021. **273**: p. 121958.

7. Treiber, M., J.-Y. Kim, J. Qu, and L.J. Jacobs, *Effects of sand aggregate on ultrasonic attenuation in cement-based materials.* Materials and structures, 2010. **43**(1): p. 1-11.

8. Torello, D., S. Thiele, K.H. Matlack, J.-Y. Kim, J. Qu, and L.J. Jacobs, *Diffraction, attenuation, and source corrections for nonlinear Rayleigh wave ultrasonic measurements.* Ultrasonics, 2015. **56**: p. 417-426.

9. Yang, Y., C.T. Ng, M. Mohabuth, and A. Kotousov, *Finite element prediction of acoustoelastic effect associated with Lamb wave propagation in pre-stressed plates.* Smart Materials and Structures, 2019. **28**(9): p. 095007.

10. Yeung, C. and C.T. Ng, *Nonlinear guided wave mixing in pipes for detection of material nonlinearity.* Journal of Sound and Vibration, 2020. **485**: p. 115541.

11. Eiras, J., T. Kundu, J. Popovics, and J. Payá, *Cement-based material characterization using nonlinear single-impact resonant acoustic spectroscopy (NSIRAS)*, in *Nonlinear Ultrasonic and Vibro-Acoustical Techniques for Nondestructive Evaluation*. 2019, Springer. p. 487-508.

12. Lim, H.J. and H. Sohn, *Online fatigue crack prognosis using nonlinear ultrasonic modulation.* Structural Health Monitoring, 2019. **18**(5-6): p. 1889-1902.

13. Kundu, T., *Nonlinear ultrasonic and vibro-acoustical techniques for nondestructive evaluation*. 2018: Springer.

14. Yang, Y., C.-T. Ng, and A. Kotousov, *Influence of crack opening and incident wave angle on second harmonic generation of Lamb waves.* Smart Materials and Structures, 2018. **27**(5): p. 055013.

15. Yang, Y., C.-T. Ng, and A. Kotousov, *Second harmonic generation of guided wave at crack-induced debonding in FRP-strengthened metallic plates.* International Journal of Structural Stability and Dynamics, 2019. **19**(01): p. 1940006.

16. Chen, J., C. Yang, and Q. Guo, *Evaluation of surface cracks of bending concrete using a fully non-contact air-coupled nonlinear ultrasonic technique.* Materials and Structures, 2018. **51**(4): p. 1-9.

17. Kim, G., G. Loreto, J.-Y. Kim, K.E. Kurtis, J.J. Wall, and L.J. Jacobs, *In situ nonlinear ultrasonic technique for monitoring microcracking in concrete subjected to creep and cyclic loading.* Ultrasonics, 2018. **88**: p. 64-71.

18. Chen, J., C. Huang, C. Yang, T. Yin, and Q. Guo, *Non-linear ultrasonic investigation of interface debonding of steel-concrete composites.* Insight-Non-Destructive Testing and Condition Monitoring, 2018. **60**(3): p. 155-160.

19. Mohseni, H. and C. Ng, *Higher harmonic generation of Rayleigh wave at debondings in FRP-retrofitted concrete structures.* Smart Materials and Structures, 2018. **27**(10): p. 105038.

20. Mohseni, H. and C.-T. Ng, *Rayleigh wave propagation and scattering characteristics at debondings in fibre-reinforced polymer-retrofitted concrete structures.* Structural Health Monitoring, 2019. **18**(1): p. 303-317.

21. Leśnicki, K.J., J.-Y. Kim, K.E. Kurtis, and L.J. Jacobs, *Assessment of alkali–silica reaction damage through quantification of concrete nonlinearity.* Materials and structures, 2013. **46**(3): p. 497-509.

22. Chen, J., R. Bharata, T. Yin, Q. Wang, H. Wang, and T. Zhang, *Assessment of sulfate attack and freeze–thaw cycle damage of cement-based materials by a nonlinear acoustic technique.* Materials and Structures, 2017. **50**(2): p. 105.

23. Carrión, A., V. Genovés, G. Pérez, J. Payá, and J. Gosálbez, *Flipped accumulative non-linear single impact resonance acoustic spectroscopy (FANSIRAS): a novel feature extraction algorithm for global damage assessment.* Journal of Sound and Vibration, 2018. **432**: p. 454-469.

24. Donskoy, D.M. and A.M. Sutin, *Vibro-acoustic modulation nondestructive evaluation technique.* Journal of intelligent material systems and structures, 1998. **9**(9): p. 765-771.

25. Chen, J., A.R. Jayapalan, J.-Y. Kim, K.E. Kurtis, and L.J. Jacobs, *Nonlinear wave modulation spectroscopy method for ultra-accelerated alkali-silica reaction assessment.* ACI Materials Journal, 2009. **106**(4): p. 340.

26. Chen, J., Y. Wu, T. Yin, N. Talebzadeh, and Q. Guo, *Characterization of concentrated and distributed cracks in concrete using a harmonic wave modulation technique.* Materials and Structures, 2018. **51**(1): p. 1-10.

27. Chen, J., Y. Wu, and C. Yang, *Damage assessment of concrete using a non-contact nonlinear wave modulation technique.* NDT & E International, 2019. **106**: p. 1-9.

28. Zaitsev, V., V. Nazarov, V. Gusev, and B. Castagnede, *Novel nonlinear-modulation acoustic technique for crack detection.* NDT & E International, 2006. **39**(3): p. 184-194.

29. Tournat, V., V.Y. Zaitsev, V. Nazarov, V. Gusev, and B. Castagnède, *Experimental study of nonlinear acoustic effects in a granular medium.* Acoustical Physics, 2005. **51**(5): p. 543-553.

30. Aymerich, F. and W. Staszewski, *Experimental study of impact-damage detection in composite laminates using a cross-modulation vibro-acoustic technique.* Structural Health Monitoring, 2010. **9**(6): p. 541-553.

31. Trojniar, T., A. Klepka, L. Pieczonka, and W. Staszewski. *Fatigue crack detection using nonlinear vibro-acoustic cross-modulations based on the Luxemburg-Gorky effect*. in *Health Monitoring of Structural and Biological Systems 2014*. 2014. International Society for Optics and Photonics.

32. International, A., *ASTM C215-02 Standard Test Method for Fundamental Transverse, Longitudinal, and Torsional Frequencies of Concrete Specimens*. 2002: West Conshohocken, PA.

33. Wang, Y., X. Zhu, H. Hao, and J. Ou, *Spectral element model updating for damage identification using clonal selection algorithm.* Advances in Structural Engineering, 2011. **14**(5): p. 837-856.

34. International, A., *ASTM C78 / C78M-18 Standard Test Method for Flexural Strength of Concrete (Using Simple Beam with Third-Point Loading)*. 2018: West Conshohocken, PA.

Chapter 4

Amplitude-Modulation Vibro-Acoustic Technique for Damage Evaluation

This chapter is based on the following published paper:

Yin, T., Ng, C.T., Vidler, J., Ho, V.D. and Kotousov, A., 2022. Amplitude-Modulation Vibro-Acoustic Technique for Damage Evaluation. Structural Health Monitoring, p.14759217221106209.

Statement of Authorship

Title of Paper	Amplitude-Modulation Vibro-Acoustic Technique for Damage Evaluation
Publication Status	☑ Published ☐ Accepted for Publication ☐ Submitted for Publication ☐ Unpublished and Unsubmitted w ork w ritten in manuscript style
Publication Details	Yin, Tingyuan, Ching Tai Ng, James Vidler, Van Dac Ho, and Andrei Kotousov. "Amplitude-Modulation Vibro-Acoustic Technique for Damage Evaluation." Structural Health Monitoring (2022): 14759217221106209.

Principal Author

Name of Principal Author (Candidate)	Tingyuan Yin		
Contribution to the Paper	Conceptualization, Methodology, Writing – original draft, Data curation		
Overall percentage (%)	80%		
Certification:	This paper reports on original research I conducted during the period of my Higher Degree by Research candidature and is not subject to any obligations or contractual agreements with a third party that would constrain its inclusion in this thesis. I am the primary author of this paper.		
Signature		Date	22/09/2022

Co-Author Contributions

By signing the Statement of Authorship, each author certifies that:

i. the candidate's stated contribution to the publication is accurate (as detailed above);

ii. permission is granted for the candidate in include the publication in the thesis; and

iii. the sum of all co-author contributions is equal to 100% less the candidate's stated contribution.

Name of Co-Author	Ching-Tai Ng		
Contribution to the Paper	Conceptualization, Supervision, Writing – review & editing		
Signature		Date	23/09/2022

Name of Co-Author	James Vidler		
Contribution to the Paper	Methodology, Validation, Formal analysis		
Signature		Date	27/09/2022

Name of Co-Author	Van Dac Ho		
Contribution to the Paper	Validation, Investigation, Resources		
Signature		Date	27/09/2022

Name of Co-Author	Andrei Kotousov		
Contribution to the Paper	Conceptualization, Supervision, Writing – review & editing		
Signature		Date	23/09/2022

Please cut and paste additional co-author panels here as required.

Amplitude-Modulation Vibro-Acoustic Technique for Damage Evaluation

Tingyuan Yin[1], Ching Tai Ng[1,*], James Vidler[2], Van Dac Ho[1], Andrei Kotousov[2]

[1] School of Civil, Environmental and Mining Engineering, The University of Adelaide, Adelaide, SA 5005, Australia

[2] School of Mechanical Engineering, The University of Adelaide, Adelaide SA 5005, Australia

Abstract

This study proposes an amplitude-modulation vibro-acoustic (AMVA) technique to track the evolution of thermal damage in pristine graphene (PRG) mortar. In the proposed amplitude-modulation technique, the pump wave is amplitude-modulated using three different methods, (i) the pure amplitude-modulated (PAM) method, (ii) the suppressive amplitude-modulated (SAM) method, and (iii) the transmitted amplitude-modulated (TAM) method. The nonlinear parameters α_P, α_S, and α_T corresponding to the PAM, SAM, and TAM methods, respectively, are theoretically established and experimentally demonstrated that the nonlinear parameters associated with the material nonlinearity, and they can be used to quantitatively characterize different damage stages of thermal damage. Meanwhile, the resonant frequency (RF) and ultrasonic pulse velocity (UPV) tests are conducted. The linear measurements, dynamic elastic modulus E_D obtained from RF test and ultrasonic pulse velocity c_L collected by UPV test, are used to compare with the nonlinear parameters. The results show that the proposed AMVA technique is more sensitive and feasible to serve as the tool for thermal damage detection in cement-based material compared with the conventional RF and UPV techniques.

* Corresponding Author: alex.ng@adelaide.edu.au

Keywords: amplitude-modulation, vibro-acoustic, thermal damage, cement-based material, nonlinear parameter

1. Introduction

1.1 Cement-based materials

Cement-based material is one of the most important and widely used construction materials nowadays because of its low price, strong compressive strength, and long durability. Therefore, they have been applied in energy storage systems [1], metallurgy industry [2], and nuclear waste containers [3], in which the cement-based structures are subjected to extreme condition, such as high temperature. A long-term high-temperature environment has adverse effect on microstructures and mechanical properties of the cement-based materials. In recent years, researchers have investigated the use of supplementary materials to improve the microstructures and mechanical properties of cement-based materials. Among those supplementary materials, graphene as a new carbon nanomaterial has attracted attention in science and engineering field [4]. Graphene and its derivatives (e.g. pristine graphene, graphene oxide, and reduced graphene oxide) have unique 2D structures with significant exposed surface areas, which are beneficial to chemical and physical interactions between the graphene and cement matrix. Different studies were carried out and indicated that the incorporation of graphene and its derivatives can enhance thermal properties of the cement-based materials and improve their durability when they are subjected to high temperatures [5-7].

Even though some properties of the cement-based materials have been improved by inducing graphene and its derivatives, micro-scale damage accumulates progressively under high in-service temperatures, and leads to structural damages or failures. Therefore, accurate and reliable technology for monitoring the cement-based structures under high temperatures is essential to ensure structural safety and enable substantial cost savings for energy, metallurgy, and nuclear industry. However, the existing technologies of non-destructive test (NDT) and structural health monitoring (SHM) are only capable for characterizing the defects and

damages at macro-scale [8, 9]. When the existing NDT and SHM techniques give alarms of the macro-scale damages, the failure of structures is imminent. Therefore, it is important to develop sensitive, accurate, and effective NDT and SHM techniques for cement-based structures suffering from high temperatures.

1.2 Nonlinear damage detection techniques

Some nonlinear damage detection techniques are based on nonlinear stress-strain relations. In contrast, most of the existing NDT and SHM technologies, e.g. resonant frequency method and ultrasonic pulse velocity (UPV) method assume linear stress-strain relationships [10]. Nonlinear damage detection technique aims at addressing the shortcomings, such as low sensitivity, of the existing linear damage detection techniques. Even slight discontinuities can produce notable nonlinear phenomena that are much more sensitive than linear phenomena [11, 12]. Nonlinear acoustics techniques have been proved to be one of the most promising approaches for assessing micro-scale defects and characterizing the early stage of material degradation [13, 14]. Due to the material nonlinearity caused by high temperatures, acoustic waves distort when propagating through imperfect mediums and generate nonlinear phenomena (e.g. higher order harmonics, frequency shift and sidebands). Higher-order harmonics appear at the integer multiplier of the input frequency. An indicator β_b derived from second-order harmonic generation (SHG) was used to describe the degradation of concrete integrity under the rising temperature composites by Yang *et al*. [15]. They indicated that the proposed SHG technique could truly reveal microscopic thermal damages.

Frequency shifts are the vibration responses elicited by repeating the standard resonant frequency test but with varying vibration excitation. The result shows that a group of responses shift toward the lower frequency in frequency domain when the amplitude of vibration excitation increases [16, 17]. Payan *et al*. showed that resonant frequency shifts happen while

excitation amplitude increases. The shifts became more evident with the accumulation of thermal damages in concrete materials [18]. When two continuous waves with different frequencies propagate through a nonlinear medium, the interactions between these two waves are sidebands. Hong *et al*. characterized the thermally damaged concrete using an impact-modulation method. The relationships between sidebands and input signals are defined as nonlinear parameters to quantitatively identify different levels of thermal defects [19].

1.3 Conventional vibro-acoustic modulation techniques

Conventional vibro-acoustic modulation technique, which is one of the nonlinear acoustic techniques, relies on sideband generation. It generally inputs two continuous waves, which are a low-frequency (LF) wave at frequency f_L and a high-frequency (HF) wave at frequency f_H, simultaneously into the monitored structures. When these two waves propagate through an undamaged structure, only HF component f_H exhibits in HF region of the spectrum. While in the damaged structure, the distortion occurs during the propagation, and sidebands reveal at $f_H \pm nf_L$ (n=1,2,3…), where nf_L is the bandwidth of sidebands.

Vibro-acoustic modulation techniques can be categorized into vibro-modulation (VM) and impact-modulation (IM) methods [20]. VM method employs forced harmonic generated by shaker to excite the structures. IM method uses impact excitation, which is usually excited by hammer, to induce nature vibration modes of structures. In the VM method, the LF forced harmonic is usually named as pump wave, and probe wave corresponds to the HF forced signal. Donskoy *et al*. conducted a series of experiments using the IM or VM method to detect and identify defects and cracks in the metal pipe structures by comparing the occurrence of sidebands in the spectra between intact and damaged states [20, 21]. Parsons and Staszewski selected the frequency of the pump wave by inputting a sweeping wave into the structure to find the structural nature response. Through using the frequency of the natural response, this

VM method has more intensive modulation between the pump wave and probe wave [22]. It is interesting that Nathanael *et al*. developed a VM method by exploring the interaction between a sweeping probing wave and a pump wave to monitor a steel beam in various operating conditions [23], and Bin *et al*. investigated two different VM method which applies sine and swept probing wave, respectively, to assess damages in aluminum alloy rods [24]. Zagrai *et al*. carried out in-situ monitoring of steel and aluminum samples using the VM method during the fatigue tests. The vibration induced by the fatigue loading was used to modulate the ultrasonic carrier wave [25]. Liu *et al*. developed a noncontact VM method to detect fatigue cracks in steel shaft specimens, in which the emitting and sensing transducers were all air-coupled [26]. Zhao *et al*. used the VM method to detect the early stage of bolt loosening and characterize the different pre-tightening torques using a nonlinear index [27]. Generally, different studies demonstrated the feasibility of the IM and VM method in detecting damages in metal structures [26, 28].

Vibro-acoustic modulation techniques were also developed for composites structures. Solodov *et al*. explored the effectiveness of a self-modulation VM method to detect damages caused by mechanical impacts, and this study demonstrated that there is a high localization around the defect in a polystyrene plate [29]. Aymerich *et al*. proposed a cross-modulation VM method, in which the pump wave is modulated by two frequencies according to the Luxemburg-Gorky effect. It was demonstrated that this method can detect damages caused by low-velocity impact in the composites plate [30]. Kim *et al*. proposed to use a large amplitude of LF vibration as the pump wave in the VM method for composite wind turbines [31]. Ooijevaar *et al*. used VM method to detect the damages in a composite skin-stiffener structure, and demonstrated the potential of VM method to characterize the presence and localization of impact damages [32].

Different studies focused on the IM and VM method characterizing the damages in cement-based material structures [33-35]. Chen *et al*. [36], Mahadevan *et al*. [37] and Karve *et al*. [38] investigated the vibro-acoustic modulation techniques, such as IM and VM method, in identifying damages caused by the alkali-silica reaction (ASR) in cement-based materials. Chen *et al*. found that the VM method is effective in evaluating the progression of concrete cracks in concentrated form and distributed form [39]. Miró *et al*. developed a VM method, in which both input pump and carrier signals were ultrasonic waves to detect different levels of corrosion at steel rebar in reinforced concrete [40].

However, the studies showed that the accurate identification of sideband location in the frequency domain through the IM method is difficult because the natural vibration modes of structures are usually not isolated and easily masked by the noise level or the aliasing effect of signal processing. Although the vibro-acoustic modulation technique is applicable to cement-based materials (e.g. cement paste, mortar or concrete), there is still a strong incentive for further study and improvement since cement-based materials are hydraulic binders mixed with aggregates and other supplements, which are more complicated than metal and composite materials. Moreover, the cement-based materials have high amplitude attenuation. Therefore, the research of developing the VM method of vibro-acoustic modulation technique is critical for improving the effectiveness, accuracy and sensitivity in damage detection on cement-based materials.

The conventional VM method takes advantage that the pump wave provides a relatively large-amplitude field to perturb the cracks and defects while the probe wave is sensitive to scan the tiny damages because of its shorter wavelength. When using a monochromatic LF wave, the wavelength vastly exceeds the size of micro-damages, and this makes the LF wave insensitive to detect the micro changes in materials [41]. While applying a monochromatic HF wave, it is widely recognized that wave propagation in the cement-based materials has

significant attenuation, particularly for the HF waves. Therefore, by combining the LF pump wave and HF probe wave, the conventional VM method addresses the drawbacks of using monochromatic HF wave or LF wave. The LF pump wave provides an intensive and high-amplitude vibration field to perturb discontinuities in the materials to maximize contact areas. The contact areas between the crack surfaces increase in compression and decrease in tension. During the strong contact effect in compression and the weak connection in tension, the HF carrier wave can scan and monitor the structural changes when it propagates through the cracks and defects.

In the conventional VM method, the frequency selection of the pump wave is a challenging issue. As illustrated in Fig.4-1, f_L presents the frequency of pump wave, and f_H is the frequency of probe wave. First, the use of lower-frequency f_{L1} causes a large burden on the impulse excitation facilities (e.g. electromagnetic shaker), particularly for long-term SHM as shown in Fig.4-1 (a). Second, when using the higher-frequency f_{L2} for the pump wave as presented in Fig.4-1 (b), the bandwidth $n \cdot f_{L2}$ is large, which makes sidebands symmetrically distribute in a broad frequency range of the spectrum. Thus, some sidebands are out of the receiving range of transducers due to their limited bandwidth.

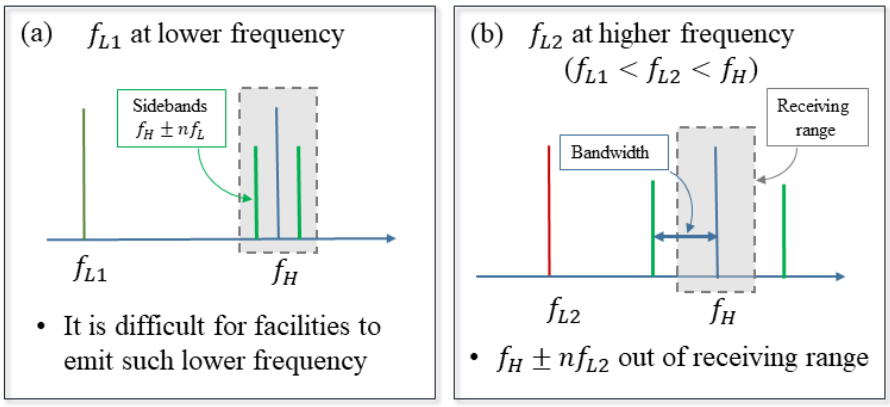

Fig.4-1 The spectrum responses of different pump wave: (a) at f_{L1} (b) at f_{L2}

To address the aforementioned limitations, this study proposed an amplitude-modulation vibro-acoustic (AMVA), which utilizes a LF amplitude-modulated pump wave and a HF probe wave. There are two major contributions in this research:

- The new AMVA technique is proposed by utilizing the amplitude-modulated pump wave instead of the pure monochromatic pump wave used in the conventional VM method to achieve energy efficiency and versatility. In this study, for the first time, three different amplitude-modulated pump waves are investigated. They are the pure amplitude-modulated (PAM) method, the suppressive amplitude-modulated (SAM) method, and the transmitted amplitude-modulated (TAM) method.
- The nonlinear parameters of the proposed PAM, SAM and TAM methods are established based on the material nonlinearity, and these parameters are correlated to the damage evolution. Meanwhile, by comparing the results of the conventional resonant frequency (RF) test and ultrasonic pulse velocity (UPV) test, the reliability and effectiveness of the nonlinear parameters are validated.

2. Proposed amplitude-modulation vibro-acoustic techniques based on material nonlinearity

In the AMVA technique, the LF pump wave is modulated by two waves with frequencies of f_{L1} and f_{L2} as shown in Fig.4-2 (a). It should be noted that Fig.4-2 is a schematic diagram, and the real signals of the PAM, SAM and TAM are shown in Section 2.3.2. The HF probe wave of f_H is shown in Fig.4-2 (b), and it is emitted simultaneously with the LF pump wave $(f_{L1} \pm f_{L2})$. When these two waves propagate through damaged stuctures, some new frequency components appear, which are sidebands at the frequencies of $f_H \pm nf_{L1}$ and $f_H \pm nf_{L1} \pm nf_{L2}$ as shown in Fig.4-2 (b). In addition, the advantages of the AMVA technique are as follow:

(i) Sensitive to the damages and have less attenuation in cement-based materials.

(ii) Compared with the single-frequency pump wave of the conventional VM method, the amplitude-modulated pump wave of the proposed AMVA is more energy efficient. This is discussed further in Section 4.3.1.

(iii) Address the limitation of the frequency range of the LF signal generator. In the proposed AMVA technique, the facility, such as an electromagnetic shaker, emits a signal at the frequency of f_{L2} and the frequency of f_{L1} is transmitted to modulate with probe wave at f_H. For instance, the emitting frequency range of the shaker is 200 Hz to 5 kHz. By using the pre-mixed pump wave modulated by $f_{L1} = 10$ Hz and $f_{L2} = 1$ kHz, the shaker actually emits the signal at 1 kHz. But the frequency of 10 Hz can be transmitted and its interaction with other frequencies can be observed in the frequency domain of the receiving signal.

(iv) The sidebands distribute evenly at a wider frequency range, and thus, they are at the effective bandwidth of the broadband transducer and narrowband transducer. Hence, the sidebands can be easily received using these transducers.

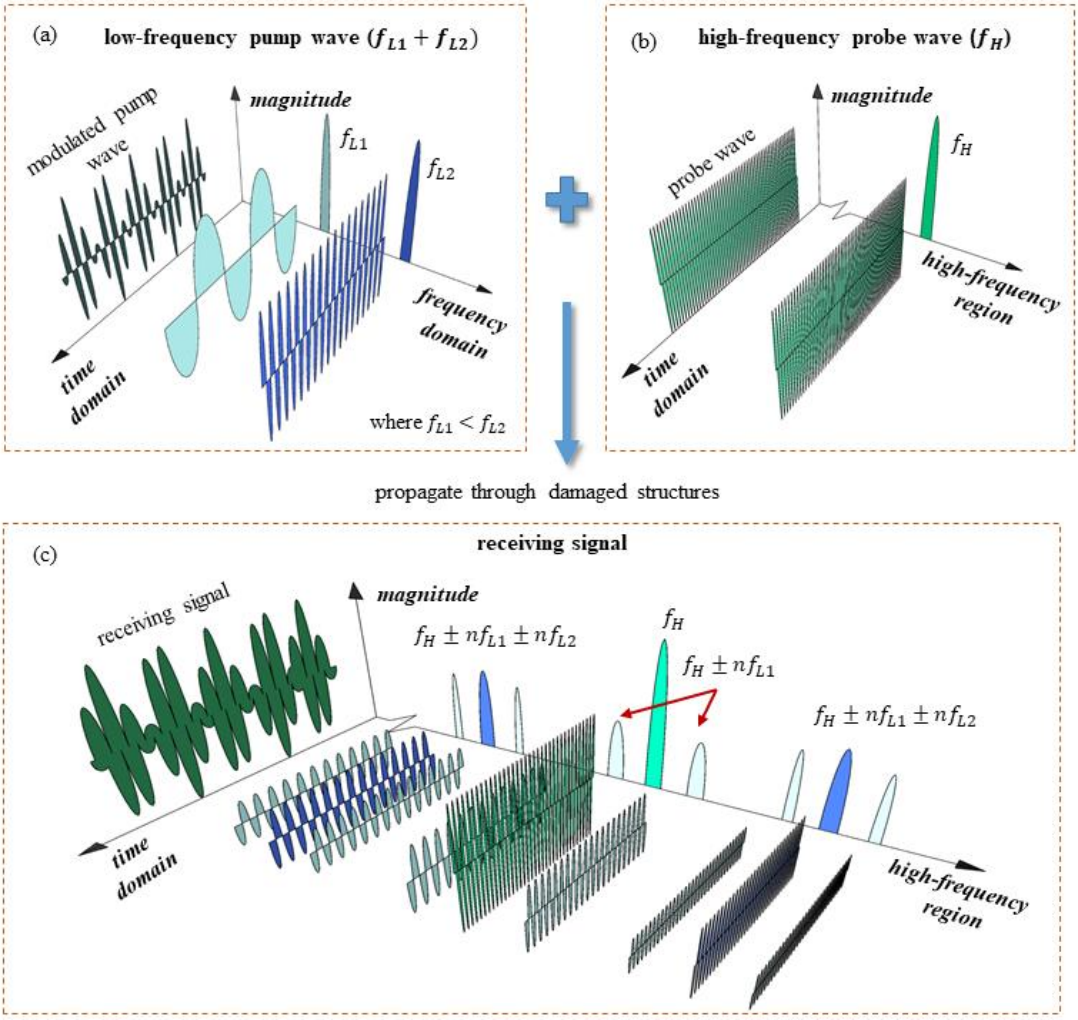

Fig.4-2 Schematic diagram of proposed amplitude-modulation vibro-acoustic technique

2.1 Nonlinear parameters of PAM, SAM and TAM methods

In this section, a theoretical model is presented to describe the interaction of frequency components of PAM, SAM and TAM methods. Meanwhile, nonlinear parameters of PAM, SAM and TAM methods are obtained through derivation of wave equation with introducing nonlinearity.

When probe wave and pump wave propagate in a damaged structure, the receiving wave contains the sidebands components due to the material nonlinearity. In this study, both emitting waves are longitudinal bulk waves, which are purely longitudinal wave mode, and hence, only longitudinal displacement exists. Using the Lagrangian coordinate x and time t, a

1D equation of motion for waves propagating in the lossless infinite medium with an introducing nonlinear parameter α is expressed as [42]:

$$\frac{\partial^2 u}{\partial t^2} - c^2 \frac{\partial^2 u}{\partial x^2} = c^2 \frac{\partial}{\partial x}[\frac{\alpha}{2}\left(\frac{\partial u}{\partial x}\right)^2 + \cdots] \tag{4-1}$$

where c is wave velocity, and u is particle displacement.

The perturbation method is applied for the following analysis, in which it is assumed that the response of a weakly nonlinear system can be made up of the linear response and nonlinear perturbation [43, 44]. Since the nonlinearity is small so the nonlinear perturbation arouse by the linear response is also small. Therefore,

Assume the wave propagates in the elastic medium. The displacement field can be written as the sum of the primary field u_1 and secondary field u_2,

$$\mathrm{u} = u_1 + u_2 \tag{4-2}$$

u_1 and u_2 satisfy $u_2 \ll u_1$. Inserting Eq.(4-2) into Eq.(4-1), one obtains the equation of motion for the primary field as follows,

$$\frac{\partial^2 u_2}{\partial t^2} - c^2 \frac{\partial^2 u_1}{\partial x^2} = 0 \tag{4-3}$$

Neglecting higher-order terms, the governing equation for u_2 is,

$$\frac{\partial^2 u_2}{\partial t^2} - c^2 \frac{\partial^2 u_2}{\partial x^2} = c^2 \frac{\partial}{\partial x}[\frac{\alpha}{2}\left(\frac{\partial u_1}{\partial x}\right)^2 + \cdots] \tag{4-4}$$

The primary filed u_1 is not affected by the nonlinearity; therefore, the solution of u_1 is the same as the incident waves

In the AMVA technique, two LF waves, $A_{L1}\cos(\omega_{L1}\tau + \phi_{L1})$ and $A_{L2}\cos(\omega_{L2}\tau + \phi_{L2})$ are pre-modulated as the pump wave, and then the HF probe wave is emitted simultaneously with the LF pump wave. A is the amplitude, ω is the angular frequency, ϕ is the phase, and $\tau = t - x/c$. It should be noted that the subscript H indicates the HF probe wave, and $L1$ and $L2$ denote two LF waves for pre-amplitude-modulation. Hence, the primary displacement field generated by the incident waves can be written as:

In the PAM method,

$$u_1^P = A_H \cos(\omega_H \tau + \phi_H) + [A_{L1} \cos(\omega_{L1} \tau + \phi_{L1}) + A_{L2} \cos(\omega_{L2} \tau + \phi_{L2})] \quad (4\text{-}5)$$

In the SAM method,

$$\begin{aligned} u_1^S &= A_H \cos(\omega_H \tau + \phi_H) + A_{L1} A_{L2} \cos(\omega_{L1} \tau + \phi_{L1}) \cos(\omega_{L2} \tau + \phi_{L2})] \\ &= A_H \cos(\omega_H \tau + \phi_H) + \frac{A_{L1} A_{L2}}{2} \cos[\,(\omega_{L2} + \omega_{L1})\tau + (\phi_{L2} + \phi_{L1})] \\ &\quad + \frac{A_{L1} A_{L2}}{2} \cos[\,(\omega_{L2} - \omega_{L1})\tau + (\phi_{L2} - \phi_{L1})] \end{aligned} \quad (4\text{-}6)$$

In the TAM method,

$$\begin{aligned} u_1^T &= A_H \cos(\omega_H \tau + \phi_H) + A_{L2} \cos(\omega_{L2} \tau + \phi_{L2})\,[1 + A_{L1} \cos(\omega_{L2} \tau + \phi_{L1})] \\ &= A_H \cos(\omega_H \tau + \phi_H) + A_{L2} \cos(\omega_{L2} \tau + \phi_{L2}) \\ &\quad + \frac{A_{L1} A_{L2}}{2} \cos[\,(\omega_{L2} + \omega_{L1})\tau + (\phi_{L2} + \phi_{L1})] \\ &\quad + \frac{A_{L1} A_{L2}}{2} \cos[\,(\omega_{L2} - \omega_{L1})\tau + (\phi_{L2} - \phi_{L1})] \end{aligned} \quad (4\text{-}7)$$

where u_1^P , u_1^S and u_1^T represent the primary field of PAM, SAM, and TAM methods, respectively. From Eq.(4-6), there are three frequency components, ω_{H} , $(\omega_{\mathrm{L2}} - \omega_{\mathrm{L1}})$ and $(\omega_{\mathrm{L2}} + \omega_{\mathrm{L1}})$ which means the frequency ω_{L2} is suppressive Different from SAM method, it is obvious that ω_{L2} is transmitted according to Eq.(4-7). The details of difference (e.g. time domain and frequency domain) of pump waves of the PAM, SAM and TAM methods were discussed in section 2.3.2.

Since the perturbation method is applied, the assumption is that the secondary field is excited by the interaction of the primary field [45]. Therefore, the secondary displacement field u_2, which is also the nonlinear response, is solved by inserting Eq.(4-5) to (4-7) into Eq(4-4), respectively.

In the PAM method,

$$
\begin{aligned}
u_2^P = {} & \frac{\alpha}{8}\left(\frac{\omega_{L1}}{c}\right)^2 A_{L1}^2 x\cos[2(\omega_{L1}\tau+\phi_{L1})] \\
& +\frac{\alpha}{8}\left(\frac{\omega_{L2}}{c}\right)^2 A_{L2}^2 x\cos[2(\omega_{L2}\tau+\phi_{L2})] \\
& +\frac{\alpha}{8}\left(\frac{\omega_{H}}{c}\right)^2 A_{H}^2 x\cos[2(\omega_{H}\tau+\phi_{H})] \\
& -\frac{\alpha}{4}A_H A_{L1}\frac{\omega_H}{c}\frac{\omega_{L1}}{c}x\cos[(\omega_H-\omega_{L1})\tau+(\phi_H-\phi_{L1})] \\
& +\frac{\alpha}{4}A_H A_{L1}\frac{\omega_H}{c}\frac{\omega_{L1}}{c}x\cos[(\omega_H+\omega_{L1})\tau+(\phi_H+\phi_{L1})] \\
& -\frac{\alpha}{4}A_H A_{L2}\frac{\omega_H}{c}\frac{\omega_{L2}}{c}x\cos[(\omega_H-\omega_{L2})\tau+(\phi_H-\phi_{L2})] \\
& +\frac{\alpha}{4}A_H A_{L2}\frac{\omega_H}{c}\frac{\omega_{L2}}{c}x\cos[(\omega_H+\omega_{L2})\tau+(\phi_H+\phi_{L2})] \\
& -\frac{\alpha}{4}A_{L1} A_{L2}\frac{\omega_{L1}}{c}\frac{\omega_{L2}}{c}x\cos[(\omega_{L1}-\omega_{L2})\tau+(\phi_{L1}-\phi_{L2})] \\
& +\frac{\alpha}{4}A_H A_{L1}\frac{\omega_H}{c}\frac{\omega_{L1}}{c}x\cos[(\omega_{L1}+\omega_{L2})\tau+(\phi_{L1}+\phi_{L2})]
\end{aligned}
\qquad (4\text{-}8)
$$

Second Harmonics

Sidebands

In the SAM method,

$$
\begin{aligned}
u_2^S = {} & \frac{\alpha}{8}(\frac{\omega_H}{c})^2 A_H^2 x\cos[2(\omega_H\tau+\phi_H)] \\
& +\frac{\alpha A_{L1}^2 A_{L2}^2}{16c^2}x(\omega_{L2}^2-\omega_{L1}^2)\cos[2(\omega_{L2}\tau+\phi_{L2})] \\
& -\frac{\alpha A_{L1}^2 A_{L2}^2}{16c^2}x(\omega_{L2}^2-\omega_{L1}^2)\cos[2(\omega_{L1}\tau+\phi_{L1})] \\
& +\frac{\alpha A_{L1}^2 A_{L2}^2}{32c^2}x(\omega_{L2}-\omega_{L1})^2\cos[2(\omega_{L2}-\omega_{L1})\tau+2(\phi_{L2}-\phi_{L1})] \\
& +\frac{\alpha A_{L1}^2 A_{L2}^2}{32c^2}x(\omega_{L2}+\omega_{L1})^2\cos[2(\omega_{L2}+\omega_{L1})\tau+2(\phi_{L2}+\phi_{L1})] \\
& +\frac{\alpha A_H A_{L1} A_{L2}}{8c^2}x\omega_H(\omega_{L2}-\omega_{L1})\cos\{[\omega_H+(\omega_{L2}-\omega_{L1})]\tau+[\phi_H+(\phi_{L2}-\phi_{L1})]\} \\
& -\frac{\alpha A_H A_{L1} A_{L2}}{8c^2}x\omega_H(\omega_{L2}-\omega_{L1})\cos\{[\omega_H-(\omega_{L2}-\omega_{L1})]\tau+[\phi_H-(\phi_{L2}-\phi_{L1})]\} \\
& +\frac{\alpha A_H A_{L1} A_{L2}}{8c^2}x\omega_H(\omega_{L2}+\omega_{L1})\cos\{[\omega_H+(\omega_{L2}+\omega_{L1})]\tau+[\phi_H+(\phi_{L2}+\phi_{L1})]\} \\
& +\frac{\alpha A_H A_{L1} A_{L2}}{8c^2}x\omega_H(\omega_{L2}+\omega_{L1})\cos\{[\omega_H-(\omega_{L2}+\omega_{L1})]\tau+[\phi_H-(\phi_{L2}+\phi_{L1})]\}
\end{aligned}
\qquad (4\text{-}9)
$$

Second Harmonics

Sidebands

In the TAM method,

$$
\begin{aligned}
u_2^T = {} & -\frac{\alpha A_{L2}^2 A_{L1}}{4c^2}\omega_{L2}^2 x\cos(\omega_{L1}\tau+\phi_{L1}) \\
& +\frac{\alpha}{8}\left(\frac{\omega_H}{c}\right)^2 A_H^2 x\cos[2(\omega_H\tau+\phi_H)]
\end{aligned}
\qquad (4\text{-}10)
$$

LF Pump Wave

$$
\begin{aligned}
&+\frac{\alpha A_{L2}^2}{16c^2}(2\omega_{L2}^2 + A_{L1}^2\omega_{L2}^2 - A_{L1}^2\omega_{L1}^2)x\cos[2(\omega_{L2}\tau + \phi_{L2})] \\
&-\frac{\alpha A_{L2}^2 A_{L1}^2}{16c^2}(\omega_{L2}^2 - \omega_{L1}^2)x\cos[2(\omega_{L1}\tau + \phi_{L1})] \\
&+\frac{\alpha A_{L2}^2 A_{L1}^2}{32c^2}(\omega_{L2} - \omega_{L1})^2 x\cos[2(\omega_{L2} - \omega_{L1})\tau + 2(\phi_{L2} - \phi_{L1})] \\
&+\frac{\alpha A_{L2}^2 A_{L1}^2}{32c^2}(\omega_{L2} + \omega_{L1})^2 x\cos[2(\omega_{L2} + \omega_{L1})\tau + 2(\phi_{L2} + \phi_{L1})] \\
&+\frac{\alpha A_{L2}^2 A_{L1}}{8c^2}\omega_{L2}(\omega_{L2} - \omega_{L1})x\cos[(2\omega_{L2} - \omega_{L1}) + (2\phi_{L2} - \phi_{L1})] \\
&+\frac{\alpha A_{L2}^2 A_{L1}}{8c^2}\omega_{L2}(\omega_{L2} + \omega_{L1})x\cos[(2\omega_{L2} + \omega_{L1}) + (2\phi_{L2} + \phi_{L1})]
\end{aligned}
$$

Second Harmonics

$$
\begin{aligned}
&+\frac{\alpha A_H A_{L2}}{4c^2}\omega_H\omega_{L2}x\cos[(\omega_H + \omega_{L2})\tau + (\phi_H + \phi_{L2})] \\
&-\frac{\alpha A_H A_{L2}}{4c^2}\omega_H\omega_{L2}x\cos[(\omega_H - \omega_{L2})\tau + (\phi_H - \phi_{L2})] \\
&+\frac{\alpha A_H A_{L1} A_{L2}}{8c^2}\omega_H(\omega_{L2} - \omega_{L1})x\cos\{[\omega_H + (\omega_{L2} - \omega_{L1})]\tau + [\phi_H + (\phi_{L2} - \phi_{L1})]\} \\
&-\frac{\alpha A_H A_{L1} A_{L2}}{8c^2}\omega_H(\omega_{L2} - \omega_{L1})x\cos\{[\omega_H - (\omega_{L2} - \omega_{L1})]\tau + [\phi_H - (\phi_{L2} - \phi_{L1})]\} \\
&+\frac{\alpha A_H A_{L1} A_{L2}}{8c^2}\omega_H(\omega_{L2} + \omega_{L1})x\cos\{[\omega_H + (\omega_{L2} + \omega_{L1})]\tau + [\phi_H + (\phi_{L2} + \phi_{L1})]\} \\
&+\frac{\alpha A_H A_{L1} A_{L2}}{8c^2}\omega_H(\omega_{L2} + \omega_{L1})x\cos\{[\omega_H - (\omega_{L2} + \omega_{L1})]\tau + [\phi_H - (\phi_{L2} + \phi_{L1})]\}
\end{aligned}
$$

Sidebands

where u_2^P, u_2^S, and u_2^T is the nonlinear solution of PAM, SAM, and TAM method, respectively.

2.2 Nonlinear parameters

In Section 2.1, the nonlinear solution of displacement u_2^P, u_2^S, and u_2^T based on material nonlinearity are derived. For better identification, the introducing material nonlinear parameter α is denoted as α_P, α_S and α_T in the PAM, SAM and TAM method, respectively.

From the solution u_2^P of PAM method in Eq. (4-8), when the propagating distance x is settled, the nonlinear parameter α_P is related to the factors below

$$\alpha_P \sim \frac{\sum A_S}{A_H A_{L1}} \; or \; \frac{\sum A_S}{A_H A_{L2}} \tag{4-11}$$

where A_S is the amplitude of the sidebands. Additionally, the nonlinear parameters, α_S of SAM method and α_T of TAM method can be written as

$$\alpha_S \; or \; \alpha_T \sim \frac{\sum A_S}{A_H A_{L1} A_{L2}} \tag{4-12}$$

3. Experiments

3.1 Specimens

For the ingredients of the specimens, the pristine graphene (PRG) made by the First Graphene Ltd in Perth, Australia, has average particle size of 23 ± 10 μm. The design mix of PRG for mortar specimens was 0.3%, which is based on previous research of exploring optimized PRG dosage for mechanical strength. The binder was ordinary Portland cement (OPC), which meets the requirements of Australian Standard 3972-2010. A natural washed river sand with a maximum nominal grain size of 2.3 mm was used as fine aggregate. To achieve better dispersion of PRG in the mixture, a superplasticizer (MasterGlenium SKY8100), which was abided the Australian Standard 1478.1-2000, was added to the PRG mortar mix. The details of the design mix of the PRG mortar specimen are shown in Table 4-1.

Table 4-1 The design mix of PRG mortar specimen

PRG (%)	PRG size (μm)	Water/cement ratio	Cement ($kg \cdot m^{-3}$)	Water ($kg \cdot m^{-3}$)	PRG ($kg \cdot m^{-3}$)	Sand ($kg \cdot m^{-3}$)	Superplasticizer ($kg \cdot m^{-3}$)
0.3	23	0.485	527	255.6	1.6	1448	1.4

To assess the inadequate dispersion of PRG, the aqueous solution was first prepared. The aqueous solution, containing the PGR, water and superplasticizer, was under sonication using Ultrasonication (UIP1000hdT) for 30 mins. Afterward, OPC and fine aggregate were sufficiently mixed for approximately 4 mins, and then the aqueous solution was gradually

added into those dry mixtures for 5 mins. All these mixtures were poured into $40\text{mm} \times 40\text{mm} \times 180\text{mm}$ molds, laid on a vibration table and was shaken for 1 min. There were three PRG mortar specimens in this batch of design mix, and they were marked as specimen 1, specimen 2 and specimen 3, respectively. After 24 hours, these specimens were demolded and cured in constant environmental conditions ($23 \pm 2℃$ and humidity $> 95\%$) until the testing age.

Before conducting the thermal damage tests, all PRG mortar specimens stayed in the ambient environment ($23 \pm 2℃$ and humidity $45 \pm 5\%$) until the weight of the specimen was no longer changed. Then an electrical muffle furnace (Elite BSF12/22A) was utilized for the heating treatments. The heating rate was set at $5℃/\text{min}$. The target temperature for sample 1, sample 2 and sample 3 was 100℃, 250℃ and 360℃, respectively. When it reached the target temperatures, the specimens suffered to the constant target temperature for approximately two hours. Afterward, these specimens were removed from the furnace and moved to the laboratory under ambient environmental conditions again until the temperature and weight of specimens stayed stable.

3.2 Conventional linear techniques following ASTM C215-19 and C597-09

3.2.1 Resonant frequency technique

Resonant frequency (RF) tests following ASTM C215-19 [46] were carried out to acquire the fundamental longitudinal frequency n' of PRG mortar bars for the purpose of calculating the dynamic elastic modulus E_D. The specimen was supported and subjected to free vibration. Through knocking the specimen, the resonant signal was captured by accelerometer (SN#578) and then fed into coupler (KISTLER type 5134B). Finally, the resonant signal was converted to a digital signal by the data acquisition unit (DAQ NI USB 6281). The measurement n' was used as a reference for the selected frequencies of the pump wave. In addition, the results of

E_D were used to compare with the nonlinear parameters obtained from PAM, SAM and TAM methods.

3.2.2 Ultrasonic pulse velocity technique

Ultrasonic pulse velocity (UPV) test following ASTM C597-09 [47] was conducted. PRG mortar specimen was laid on a sponge cushion with two broadband transducers (Ultran GC) attached to the opposite side by vacuum coupling grease. Emitting signal was a 0.35MHz Hanning windowed tone burst with five cycles generated by NI PXI-5412 signal generator. This emitting signal was amplified by Brüel & Kjær 2718 power amplifier before transmitting to the transducers. After the wave propagating from one side of the specimen to the other side, the time domain signal was recorded by NI PXI-5105, from which the time of flight was obtained by checking the peak of receiving signal after zero-time adjustment.

3.3 Proposed nonlinear amplitude-modulation vibro-acoustic techniques

3.3.1 Experimental set-up

The experimental set-up of the AMVA technique is presented in Fig.4-3. The frequencies f_{L1} and f_{L2} were selected through a group of resonant tests and were decided based on the responses of specimens. A continuous wave modulated by the waves of 0.5 kHz and 5.7 kHz was generated by the signal generator (NI PXI-5412) and used as the low-frequency pump signal. Then the pump wave was magnified 20 dB by an amplifier (Brüel & Kjær Power Amplifier 2718) before it was transmitted to an electromagnetic shaker. It should note that the pump waves for PAM, SAM, and TAM methods were pre-modulated according to the Eq.(4-5), Eq.(4-6) and Eq.(4-7), respectively. Some details (e.g. time domain and frequency domain of pump waves) are discussed in section 2.3.2. A 3D printed clamp was designed to transfer the pump waves efficiently and firmly from the shaker to the PGR specimens The clamp was

made by the polyethylene terephthalate(PETG), and was in C-shape. On the centre of each side, a hole was drilled for pin screw and threaded rod of the shaker. Once the pin screws were tightened, the thread rod of the shaker was firmly connected to the specimen while there was no contact between clamp and specimen. The details of the 3D printed clamp is shown in Fig.4-3. Meanwhile, a continuous probe wave at 50 kHz was first generated by a functional generator (Tektronix AFG 302113), and its voltage was increased by a signal amplifier (Krohn Hite model 7500). Finally, the probe wave was transmitted into the specimen by a non-metal transducer with 50 kHz central frequency. It should be noted that the peak-to-peak voltage of the pump wave remains the same during the whole experiment, whereas the peak-to-peak voltage of the probe wave was increased steadily. Both pump wave and probe wave were modulated and transmitted to the specimens. Finally, these two waves were captured by the other 50 kHz non-metal transducer at the opposite side of the PGR mortar bars, and the data was recorded by digitizer (NI PXI-5105). The peak-to-peak voltage of the pump wave remained the same during the experiments while the peak-to-peak voltage of the probe wave progressively increased at a steady rate.

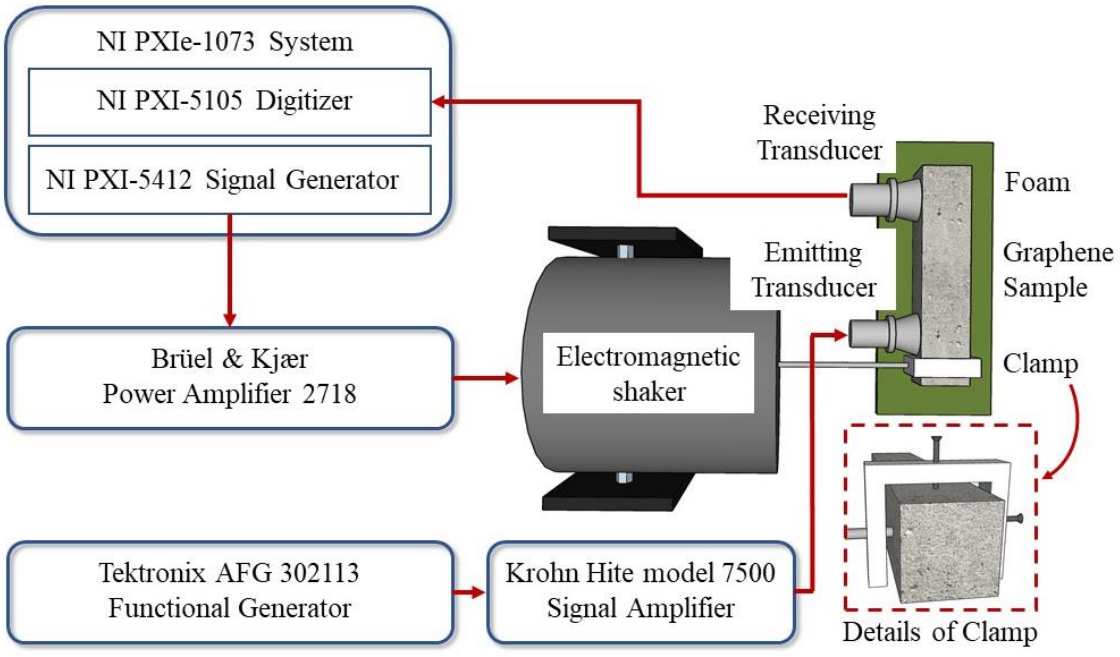

Fig.4-3 Experimental set-up of the proposed AMVA technique

3.3.2 Extraction of sidebands

Since the sidebands can occur at many frequencies of $f_H \pm nf_{L1} \pm nf_{L2}$ $(n = 1,2,3,4)$, it needs to define criteria to ensure the extraction of sidebands for the nonlinear parameter is robust. According to the nonlinear parameters in Eq.(4-11) and (4-12), and the results of the experiments, the following general criteria are used in extracting the sideband for nonlinear parameter calculation.

i) the sidebands are apparent and not masked by the other sidebands;

ii) the magnitudes of sidebands are larger than 0.01% of the magnitudes of probe waves;

iii) the maximum multiple (such as n aforementioned) is four.

In this study, the sidebands are extracted based on these three criteria and used to calculate the nonlinear parameters.

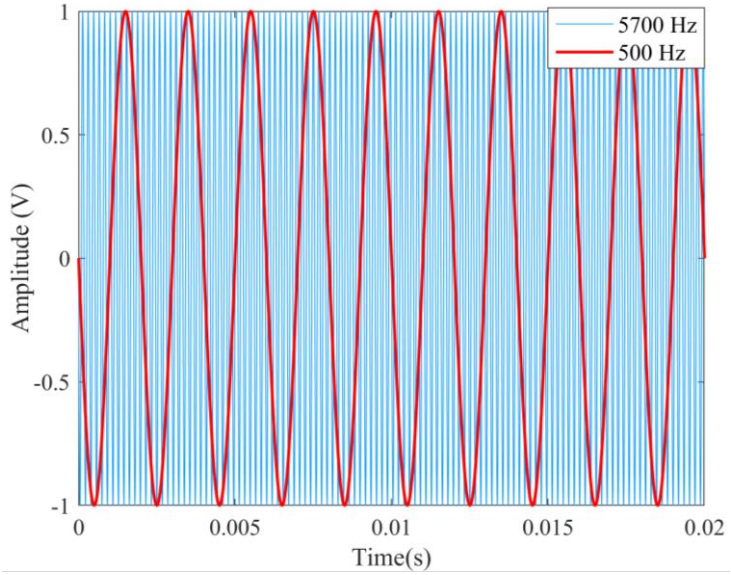

Fig.4-4 Two continuous waves of f_{L1}= 500 Hz and f_{L2}= 5700 Hz

Two monochromatic waves of $f_{L1} = 500$ Hz and $f_{L2} = 5700$ Hz as shown in Fig.4-4 are modulated using Eq.(4-5)-(4-7), respectively. Thus, the amplitude-modulated pump wave of the PAM method is represented in Fig.4-5(a), while the pump wave of the SAM and TAM method is shown in Fig.4-6(a) and Fig.4-7(a), respectively. The fast Fourier transform (FFT)

is then used to transfer the time-domain pump waves into the frequency domain. It is interesting that the pump wave of the PAM method consists of two frequencies at $f_{L1} = 500$ Hz and $f_{L2} = 5700$ Hz as shown in Fig.4-5(b). Whereas there are also two frequency components in the pump wave of the SAM method but the frequencies are at the $f_{L2} - f_{L1} = 5200$ Hz and $f_{L2} + f_{L1} = 6200$ Hz as shown in Fig.4-6(b). Similar to the SAM method, the pump wave of the TAM method contains the frequency components at $f_{L2} - f_{L1} = 5200$ Hz and $f_{L2} + f_{L1} = 6200$ Hz, but the original frequency f_{L2} =5700 Hz is also transmitted as shown in Fig.4-7(b).

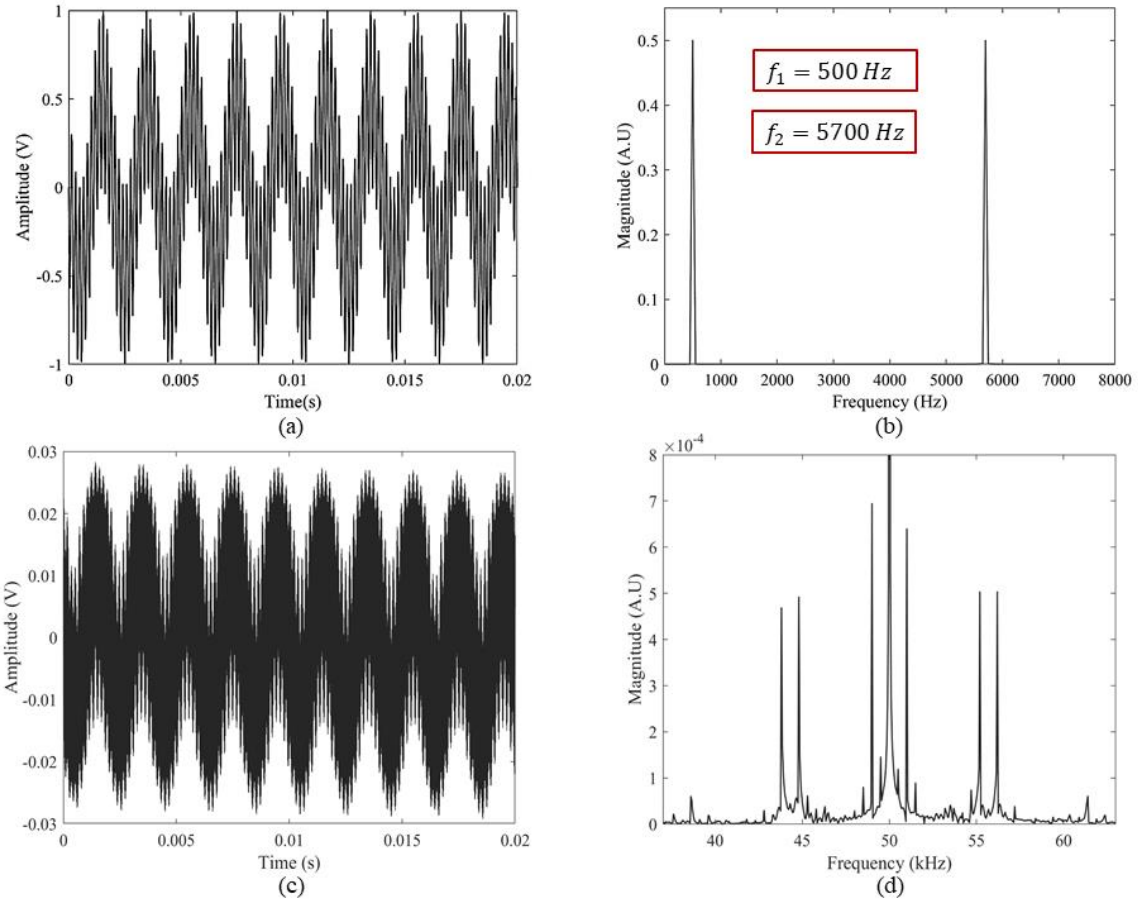

Fig.4-5 Pure cross-modulation (PAM) method: (a) time domain of pump wave (b) frequency domain of pump wave (c) time domain of receiving signal (d) frequency domain of receiving signal

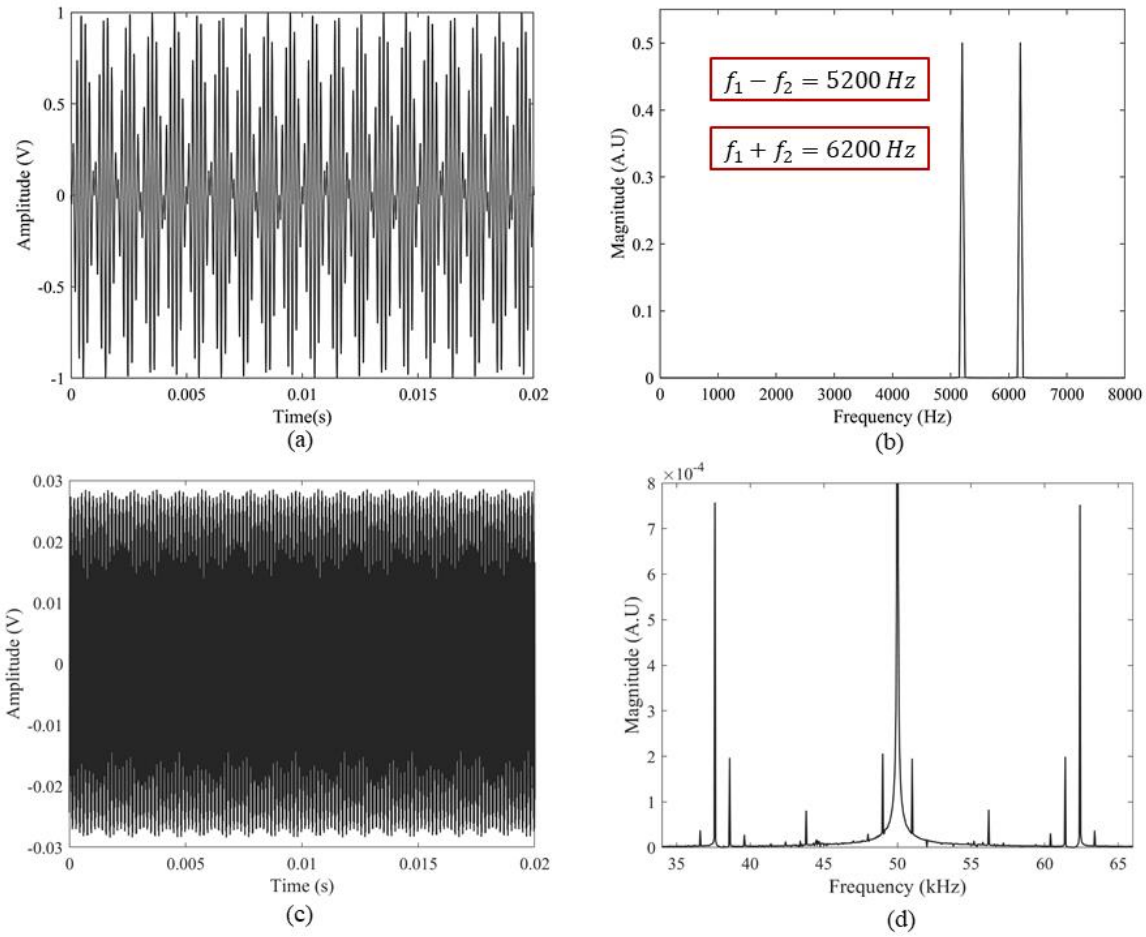

Fig.4-6 Suppressive f_{L1} amplitude-modulation (SAM) method: (a) time domain of pump wave; (b) frequency domain of pump wave; (c) time domain of receiving signal; (d) frequency domain of receiving signal

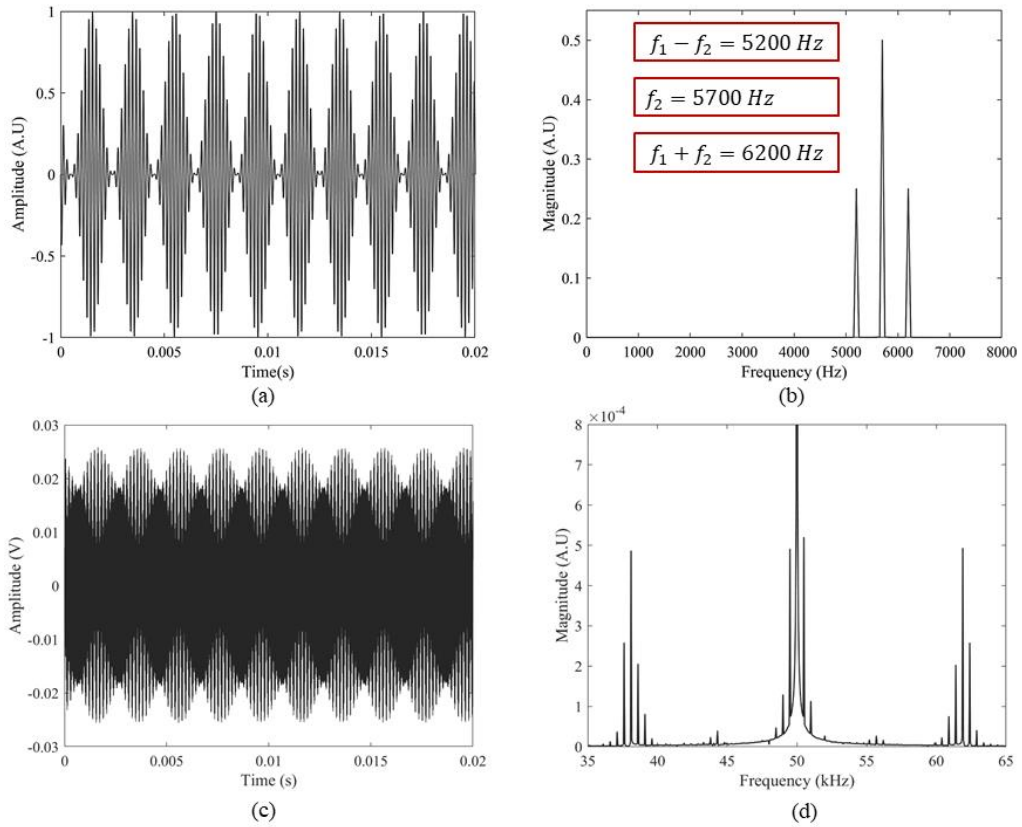

Fig.4-7 Transmitted f_{L1} amplitude-modulation (TAM) method: (a) time domain of pump wave; (b) frequency domain of pump wave; (c) time domain of receiving signal; (d) frequency domain of receiving signal

The pump wave accompanying the probe wave propagates through the whole specimen and is captured for further analysis. The receiving signals of the PAM, SAM and TAM method are shown in Fig.4-5(c) and 4-5(d), Fig.4-6(c) and Fig.4-6(d), and Fig.4-7(c) and 4-7(d), respectively. The PAM, SAM and TAM method have different frequency responses. Therefore, the sidebands, which are selected to calculate the nonlinear parameters, are also different. The details of sidebands used for calculating of the nonlinear parameters are summarized in Table 4-2.

Table 4-2 The frequencies of sidebands for calculating α_P, α_S and α_T

Method	Frequencies of sidebands	Details
PAM method	$f_H - nf_{L1}$ $(n = 1,2,3,4)$	49.5kHz, 49kHz, 48.5kHz, 48kHz
	$f_H + nf_{L2}$ $(n = 1,2,3,4)$	50.5kHz, 51kHz, 51.5kHz, 52kHz
	$f_H \pm nf_{L2}$ $(n = 1)$	44.3kHz, 55.7kHz
	$f_H \pm nf_{L2} \pm nf_{L1}$ $(n = 1)$	43.8kHz, 44.8kHz, 55.2kHz, 56.2kHz
SAM method	$f_H \pm n(f_{L2} + f_{L1})$ $(n = 1,2)$	37.6kHz, 43.8 kHz, 56.2 kHz,62.4 kHz
	$f_H \pm n(f_{L2} - f_{L1}) \pm n(f_{L2} + f_{L1})$ $(n = 1)$	38.6 kHz, 49 kHz, 51 kHz, 51.4 kHz
TAM method	$f_H \pm nf_{L1}$ $(n = 1,2)$	50.5 kHz, 49.5 kHz, 49 kHz, 51 kHz
	$f_H \pm nf_{L2}$ $(n = 1,2)$	38.6kHz, 44.3 kHz, 55.7 kHz, 61.4kHz
	$f_H \pm n(f_{L2} - f_{L1})(n = 1)$	44.8 kHz, 55.2 kHz
	$f_H \pm n(f_{L2} + f_{L1})(n = 1)$	43.8 kHz, 56.2 kHz,
	$f_H \pm n(f_{L2} - f_{L1}) \pm n(f_{L2} + f_{L1})$ $(n = 1\ or\ 2)$	38.1 kHz, 39.1 kHz, 60.9 kHz, 61.9 kHz

3.3.3 Calculation of nonlinear parameters

According to Eq.(4-11) and Eq.(4-12), the nonlinear parameters correspond to the amplitude of sidebands A_S divided by $A_H A_L$(where A_L= A_{L1}, A_{L2} or $A_{L1}A_{L2}$). To control the order of magnitude of the nonlinear parameters for better comparison, only two amplitudes, A_H and A_D are chosen to calculate the nonlinear parameters. A_H is the amplitude at the frequency f_H while A_D is the amplitude of dominant pump frequency. In these AMVA methods, the dominant pump frequency is: i) $f_{L1} = 500$ Hz for the PAM method, ii) $f_{L1} + f_{L2} = 6200$ Hz for the SAM method, iii) $f_{L2} = 5700$ Hz for the TAM method, respectively. In the experiments, the amplitudes of the input pump wave have the same value, whereas the input magnitude of the probe wave increases with a steady step. As shown in Fig.4-8, the circle markers present the data ($\sum \mathrm{A_s}$, $\mathrm{A_H A_D}$) under different input voltage levels of the probe wave. The sum of amplitude of sidebands $\sum A_s$ and $A_H A_D$ shows linear relationship, therefore, the slope of the linear fitting is the nonlinear parameter.

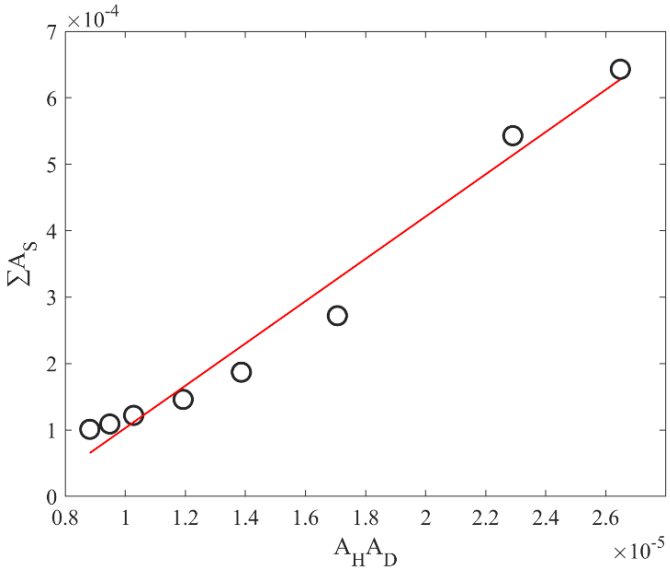

Fig.4-8 Nonlinear parameter α_T obtain from the linear relationship of A_s and A_0A_D

4. Results and discussion

In this study, the specimens were subjected to three thermal treatments,100℃, 250℃ and 360℃. From the previous investigations, PRG mortar specimens had distinct variations from the intact state to the high temperature [48, 49]. Due to the spreading of PGRs in the cement matrix, it reduced the distances between cement particles in cement gels because of the effect of van der Waals forces between PRGs[4]. In the ambient environment, the cement matrix of PRG mortar contacted tightly and was covered by C-S-H gel, which built bridges between the cement matrix and hydration products. At the 100℃, the free and absorbed water escaped, while a part of the bound water also fled. Water evaporation provoked the contraction of cement matrix and introduced more vacant holes, resulting in larger interface distances and more defects. When the specimens were heated to 250℃, the major changes were generated by the loss of bound water from the decomposition of the C-S-H gel. At the 360℃, C-H-S gel on the surface of the cement matrix vanished. The disappearance of hydration products produced masses of vacancies and defects in the cement matrix, which brought into microcracks under small stress. In addition, strain incompatibilities between the aggregates (expand after heating treatment)

and cement matrix (shrink after heating treatment) also led to more pronounced cracks in specimens [6, 50]. It should be noted that nonlinear parameters were obtained at each target temperature by three different AMVA methods. Meanwhile, two conventional measurements, dynamic elastic modulus E_D and longitudinal velocity c_L, were also collected to compare accuracy, sensitivity, and feasibility between the proposed AMVA methods and conventional RF and UPV techniques.

4.1 Results of conventional techniques

4.1.1 Results of resonant frequency technique

The RF tests were conducted at ambient temperature and after heating to target temperature as shown in Fig.4-9. E_D decreases monotonically with the increase of temperature, which is in good agreement with that of cement-based materials exposed to high temperatures. E_D changes significantly at 250℃ and at 360℃, in which the relative changing rate is 32.40% and 35.38%, respectively. Nevertheless, there is only a slight drop with changing rate of 18.66% at 100℃ when compared with 250℃ and 360℃. As to the difference between the elevated temperatures, the results show that from intact state to 100℃, the changing rate is still 18.66%, while from 100℃ to 250℃, the difference between these two temperatures is 13.74%, and it is only 2.98% when considering the difference of changing rate between 250℃ and 360℃. It may be because for temperature up to 100℃, evaporable water plays a dominant role, and this transformation is known to affect the mass of the specimens significantly, and hence, they have a considerable effect on the calculation of E_D [51]. Afterward, when the temperature reaches to 250℃, the weight loss can be attributed to the loss of bound water from the decomposition of the C-S-H, which only causes a slight drop in weight, and then E_D decreases not that obviously as the former state. After that, when the specimen was heated up to 360℃, there is a slight decrease of E_D, which is because the water was no longer the primary factor to affect E_D. The dominant

factor is that the vanishing of hydration products produce many vacancies and defects leading to material deterioration [52, 53].

However, it should be noted that escaping evaporable free and absorbed water in the range of $25℃-100℃$ is theoretically reversible. The results of the RF test have the most significant changing rate compared with the later state. The PGR mortar at $250℃-360℃$ has induced more irreversible damages, including contraction of the cement matrix, expansion of initial defects, and generation of microcracks [52, 54]. But at this state E_D only has a minor decrease.

Therefore, the following deficiencies of the RF method are revealed: i) E_D obtained from the RF method is able to assess high-temperature damages but it is observed in this study that E_D is not that sensitive to characterize permanent microstructural evolution after exposure to high temperature; ii) the measurements highly rely on the moisture content of materials, which some times bring inaccuracy and instability to field application particularly when ambient humidity change greatly, and iii) it is difficult to obtain the mass of structures for calculating E_D in in-situ tests.

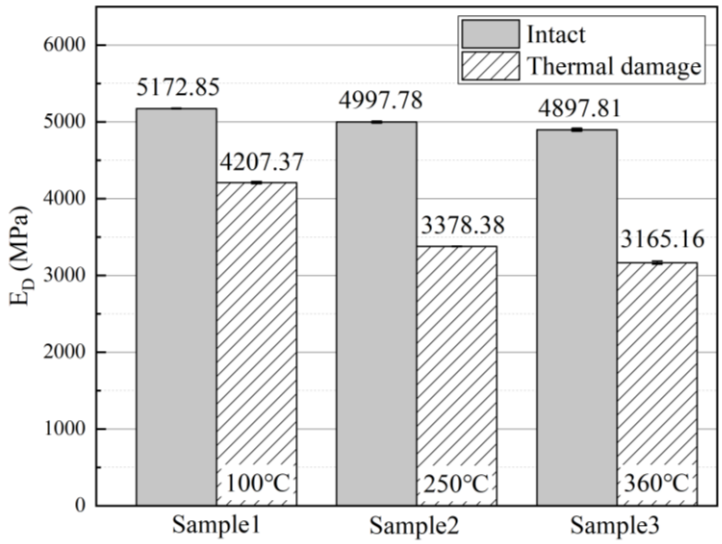

Fig.4-9 E_D of sample 1, 2 and 3 under intact state and thermal damage state

4.1.2 Results of ultrasonic pulse velocity technique

The c_L of PGR mortar specimens both at ambient and elevated temperatures were measured by UPV tests as shown in Fig 4-11. With the increase of temperature, c_L decreases monotonically, which has a similar decreasing trend as E_D, but the changing trend of c_L is gentle. The changing rate of sample 1 to sample 3 before and after exposure to high temperatures is 7.35%, 11.99% and 12.15%, respectively, and it is lower than that of the E_D. It is because the variation of c_L is attributed to the material deterioration caused by defects and microcracks rather than the reversible evaporable moistures. Hence, at 100℃ and 250℃, there are identical weight loss due to moisture decrease and water evaporation, at which the E_D shows significant decrease while the c_L drops slightly. In addition, from $25℃-100℃$, $100℃-250℃$, and $250℃-360℃$, the changing rate is 7.35%, 4.64%, and 0.16%, respectively. The tendency of changing rate is in good agreement with E_D. Despite the effect of water loss, both E_D and c_L are able to characterize the generation and expansion of defects and microcracks.

Regarding the results of c_L in this work, several characteristics of the UPV method could be found: i) even the UPV technique can distinguish the authentic irreversible damage caused by defects and microcracks, but there is still a powerful incentive to enhance the

sensitivity of the technique, ii) penetration approach was used in UPV tests whereas, in the field application, it is sometimes difficult to apply penetration approach when structures are irregular or accessible to both sides of structures is unavailable.

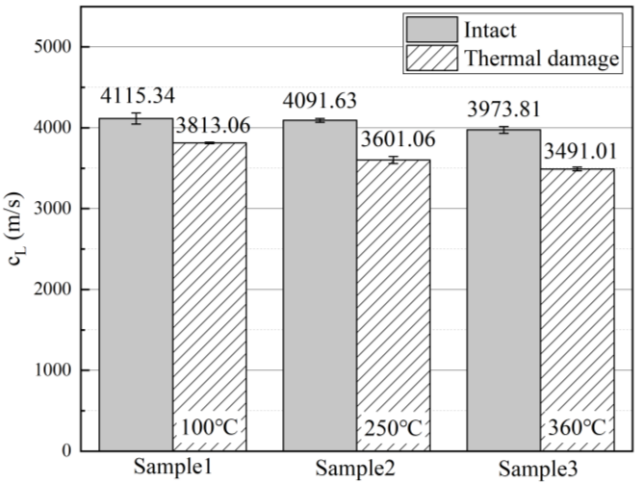

Fig.4-10 c_L of sample 1, 2 and 3 under intact state and thermal damage state

4.2 Results of the proposed nonlinear amplitude-modulation vibro-acoustic techniques

In this section, the experimental results of the three proposed AMVA techniques, PCM, SCM and TCM methods, are discussed. The effectiveness of the AMVA technique to detect and characterize the aforementioned thermal damages in the PRGs mortars is investigated.

4.2.1 Comparison of energy consumption

The energy consumption in the time range from 0s to 0.02s of different pump waves is shown in Fig.4-11. The largest energy consumption is the pure 500 Hz pump wave of the conventional VM technique without any modulation. The energy consumptions of the PAM and SAM method are 63.78% of that in the conventional VM technique. The pump wave of the TAM method has the lowest energy consumption, which is only 50.39% of the conventional VM

technique. The TAM method has less energy consumption and thus is most conducive for long-term NDT and SHM.

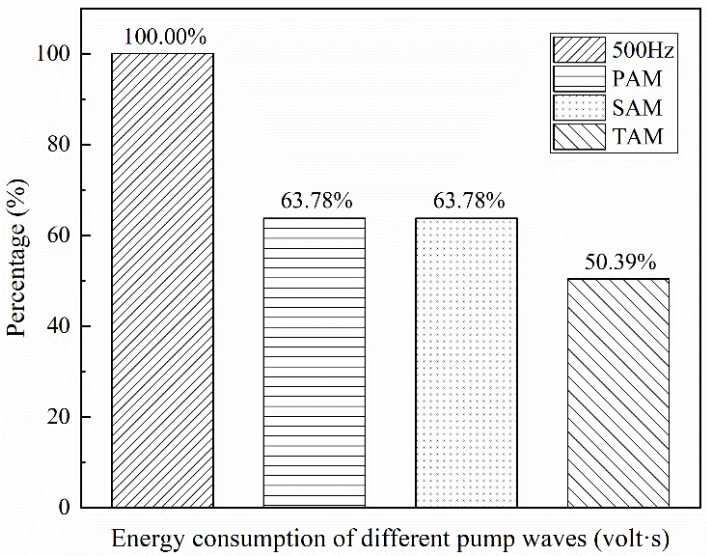

Fig.4-11 The energy consumption of different pump waves

4.2.2 Results of pure amplitude-modulation (PAM) method

The measured signals of the PAM method are transferred into frequency-domain signals as shown in Fig. 4-12, in which the probe wave is 50 kHz while the pump wave is modulated by 500 Hz and 5700 Hz using the PAM method. In Fig. 4-12 (a), the typical frequency spectrum for intact specimens is presented, in which sidebands are not evident around the f_H. It indicated that there sre no distinct defects or damages in the specimens before heating treatments. Hence the material nonlinearity in the medium is inadequate to arouse obvious sidebands. But it should be noted that the nonlinear parameters at intact state are not zero. It is in good agreement that even though no treatment is applied to these specimens, they were still not a perfect medium that had initial minor defects at the beginning.

When the specimen was heated to 100℃, the sidebands were evident as shown in Fig. 4-12(b), in which some sidebands are at frequency intervals equal to 500 Hz and others appear at intervals of 5700 $\pm$ 500 Hz. These sidebands are generated due to the material nonlinearity

caused by the escaping bound water, which leads to the contraction of cement matrix and brings into more considerable interface distance and more defects. The typical frequency spectrum at 250℃ is shown in Fig. 4-12(c). Compared to Fig. 4-12(b), there is a significant increase in the peaks of sidebands with intervals of 500 Hz, whereas only a slight increase in sidebands with intervals of 5700 $\pm$ 500 Hz. Another change occurs when the temperature reached 360℃ along with the considerable growth of magnitudes. As illustrated in Fig.4-12(d), the number of sidebands also increases. This finding is consistent with the aforementioned discussions that the vanishing of hydration products causes more noticeable cracks, cracks gradually merge, and hence, many vacancies and defects appear in the cement matrix.

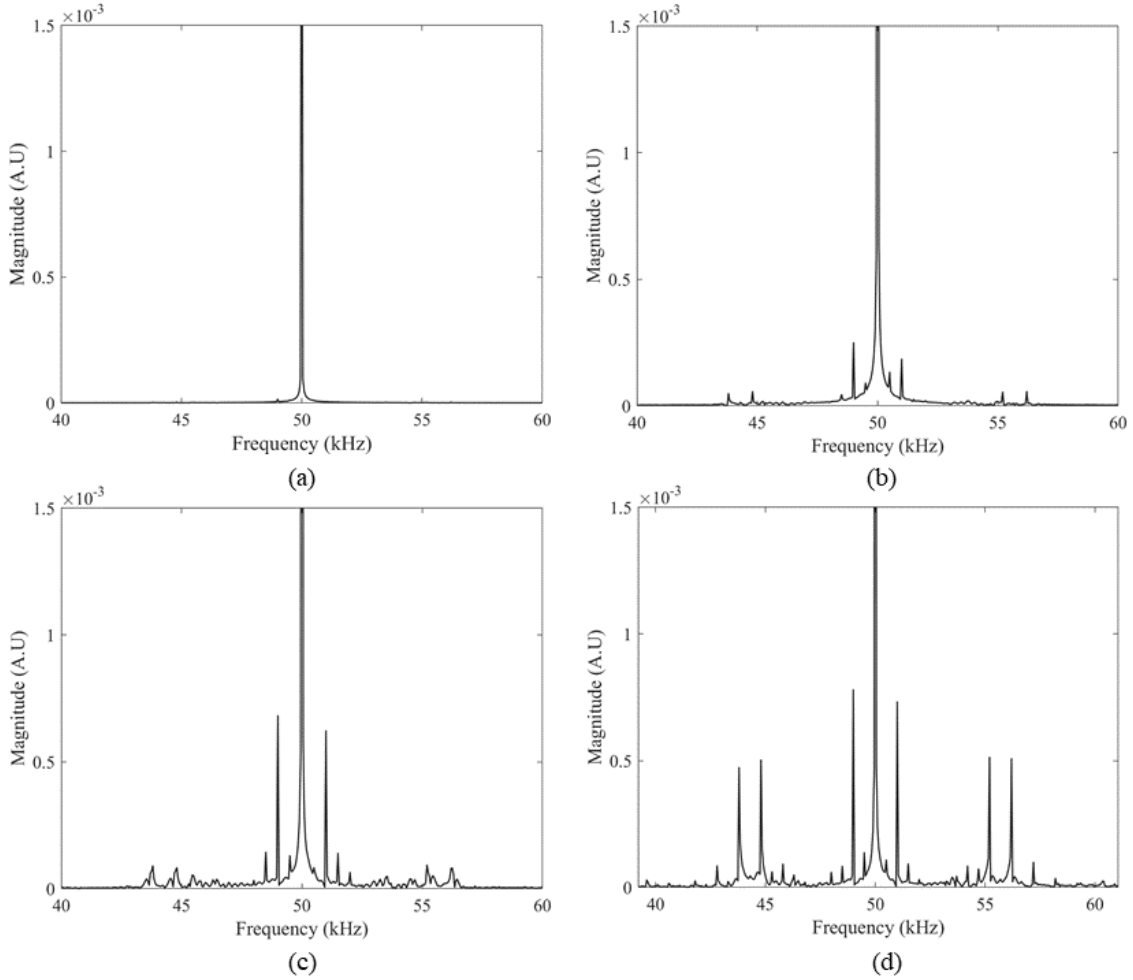

Fig. 4-12 Typical frequency domain of PAM method: (a) 25℃; (b) 100℃; (c) 250℃ and (d) 360℃

Fig.4-13 presents the nonlinear parameter α_P of the PAM method both at intact state and after high-temperature treatment. With the increase of temperature, the α_P increases intensely, particularly from 250℃ to 360℃. Even at 100℃, the changing rate of the α_P between intact state and after heating treatment is around 27.26%, which is almost two-fold of E_D or four-fold of c_L. Furthermore, the relative changing rate at 250℃ was merely 36.28%, and this is 3.88% higher than the E_D and 24.29% higher than the c_L at the same state. Particularly at the 360℃, there is a sharp increment in α_P when the temperature changes from 250℃ to 360℃, and the relative changing rate between intact and after heating to 360℃ is merely 95.46%, which is much larger than the E_D and c_L. At the 360℃, the changing rate of E_D and c_L is only 35.38% and 12.15%, respectively.

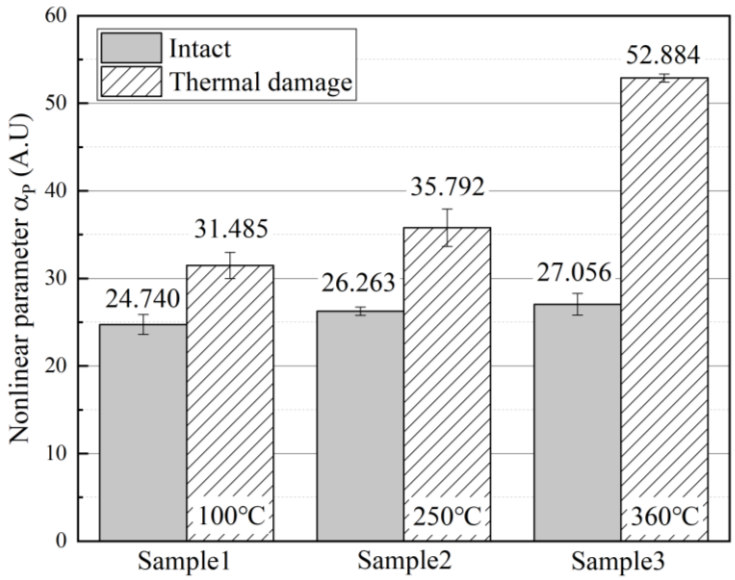

Fig.4-13 α_P of specimen 1, 2, and 3 under intact state and thermal damage state

4.2.3 Results of suppressive f_{L2} cross-modulation (SAM) method

Fig.4-14 shows the typical frequency domain of PGR mortar specimens before and after exposure to 100℃, 250℃ and 360℃ using the SAM method. It should be noted that the pump wave is mixed by 500 Hz and 5700 Hz, but the peak of 5700 Hz is suppressive, and there are only two peaks at 5200 Hz and 6200 Hz as shown in Fig.4-6 (b). Therefore, the sidebands

mainly occurs around 50 kHz with 500 Hz, 5200 Hz and 6200 Hz intervals. Interestingly, for the sidebands that appear with intervals of 5200 Hz and 6200 Hz, the magnitudes of even-sidebands are larger than odd-sidebands. It is because that the modulation parameters of emitting signals, such as bandwidth and modulation ratio, have critical impacts on the harmonic magnitudes[55, 56]. But the frequencies and amplitudes of the emitting probe wave and pump wave are fixed. Hence, the modulation parameters do not affect too much compared to the harmonic responses at different thermal damage levels. When the specimens are intact, there are only some tiny sidebands on the scale of 1×10^{-5} as presented in Fig.4-14(a). Then specimen is heated to 100℃, the sidebands at intervals of 5200 Hz and 6200 Hz increased rapidly. After that, both magnitudes and numbers of sidebands with intervals of 5200 Hz and 6200 Hz increase, meanwhile the sidebands with intervals of 500 Hz are aroused at the 250℃. In Fig.4-14(d), when the specimen is submitted to 360℃, all sidebands at intervals of 500 Hz, 5200 Hz, and 6200 Hz are apparent. The tendency of the SAM method is similar to the PCM method.

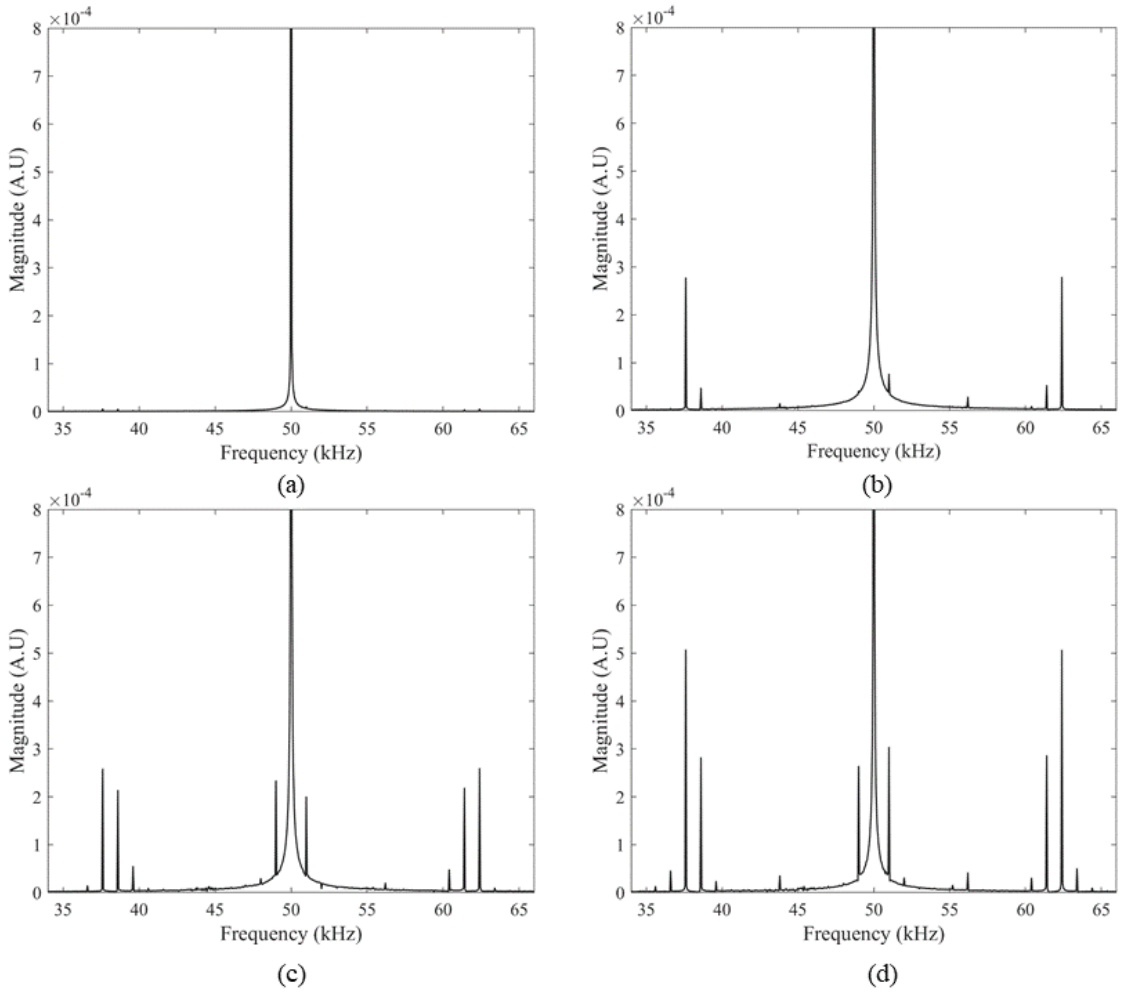

Fig.4-14 Typical frequency domain of SAM method: (a) 25℃; (b) 100℃; (c) 250℃ (d) 360℃

The nonlinear parameter α_s of the SAM method at ambient temperature (25℃) and after heating to 100℃, 250℃ and 360℃ are shown in Fig.4-15. The α_s increases continually with the increase of temperature, which is in good agreement with the tendency of the α_P of the PCM method. The α_s increases slowly from 25℃ to 100℃, with changing rate of 38.32%. While the α_s increases more obviously from 25℃ to 250℃ and to 360℃, and their changing rate is 78.96% and 115.61%, respectively. In another aspect, the changing rate of α_s from 25℃ to 100℃ is beyond two times of E_D and five times of c_L. Moreover, the changing rate of α_s to 250℃, is 66.97% higher than the c_L and 46.56% larger than the E_D. In addition, after exposure to 360℃, the changing rate of α_s is almost 103.46% higher than the c_L and 80.24% larger than

the E_D. These results reveals that α_s is as sensitive as α_p to detect and characterize the initial defects and different levels of thermal damages.

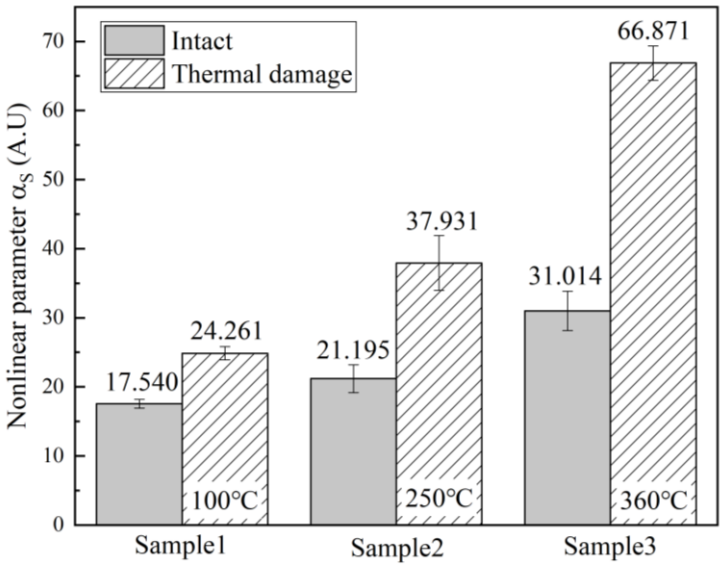

Fig.4-15 α_S of specimen 1, 2 and 3 under intact state and thermal damage state

4.2.4 Results of transmitted f_{L2} cross-modulation (TAM) method

As illustrated in Fig.4-16, the typical frequency domains of the TAM method of the PGR mortar specimens without and with thermal treatment are similar to those of the other two proposed AMVA techniques. But compared with the PAM and SAM method, the 5700 Hz is transmitted, and there are three frequency components, 5200 Hz, 5700 Hz, and 6200 Hz, in the spectrum domain as shown in Fig.4-7(b). The sidebands are similar to the SAM method, but the sidebands with intervals of 5700 Hz are aroused in the TAM method. It should be noted that the energy of emitting pump wave of the TAM method is only 79.01% of the SAM, but the magnitudes of the sideband are in the same order. According to the sidebands in these experiments, the TAM method has similar behaviors as the SAM method, but the emitting energy is lower. This finding reveals that the SAM method can provide a potential energy-saving approach for NDT and SHM, but more experiments should be conducted to demonstrate this point of view in the future. Fig.4-16 (a) shows the typical frequency domain at intact state, in which the sidebands are also at 1×10^{-5} order. Since the temperature reached 100℃,

magnitudes of even-sidebands with intervals of 5200 Hz, 5700 Hz, and 6200 Hz increased. In the frequency domain of the TAM method, even-sidebands are aroused while odd-sidebands are suppressed to some extent. This phenomenon also occurs in the SCM method because the bandwidth, modulation ratio, and emitting amplitude for the SAM and TAM methods are the same. Similar to the SAM method, the magnitudes and numbers of sidebands increase along with the increase of temperature from 25℃ to 360℃.

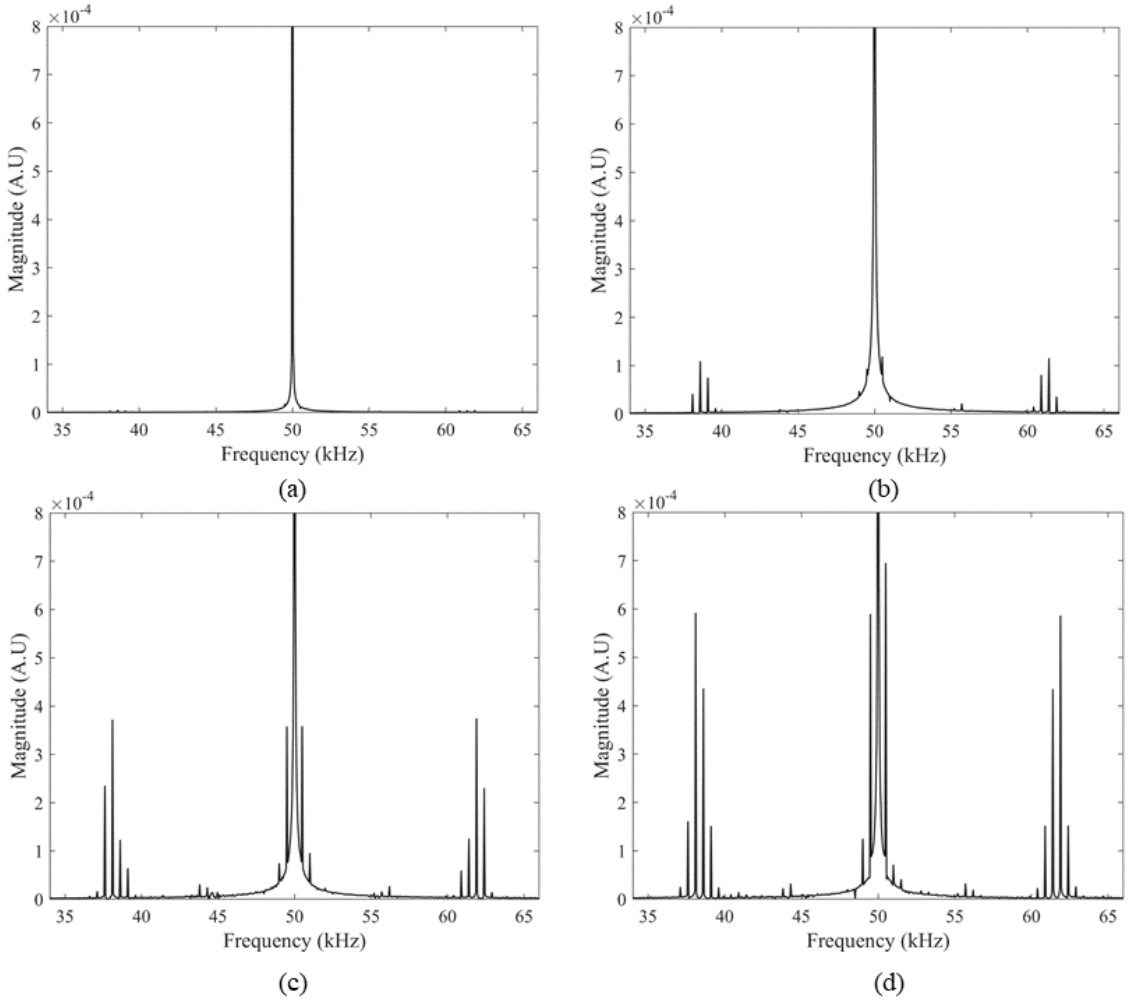

Fig.4-16 Typical frequency domain of SAM method: (a) 25℃; (b) 100℃; (c) 250℃ and (d) 360℃

Fig.4-17 shows the nonlinear parameter α_T before and after heating to target temperature. At intact state, α_T of specimen 1 is the smallest, followed by specimen 2 and specimen 3, respectively. This result is in good agreement with the results of E_D and c_L, in which sample 1 has the largest E_D and c_L followed by specimen 2 and specimen 3. All of these

findings illustrates that even this batch of specimens was cast and cured in the same condition, but there was slightly difference of their inner structures, and the sample 3 had more initial defects and microcracks. Therefore, the samples 3 has the largest nonlinear parameters of three AMVA methods and the smallest E_D and c_L before heating. In another aspect, the good agreement between these measurements reveals that the proposed AMVA techniques, PAM, SAM and TAM methods, can characterize the difference of microstructures in the cement-based materials. Before and after heating treatment, the changing rate is 41.04%, 51.06%, and 59.93% for 100℃, 250℃ and 360℃, respectively. From 25℃ to 100℃, the changing rate of α_T is 33.69% and 22.37% higher than the c_L and E_D. Particularly, from 25℃ to 250℃, the changing rate of α_T was more than five times of c_L and almost two-fold of E_D. All these results demonstrated that α_T has the ability not only to characterize the initial micro defects accurately but also distinguish different thermal damage levels.

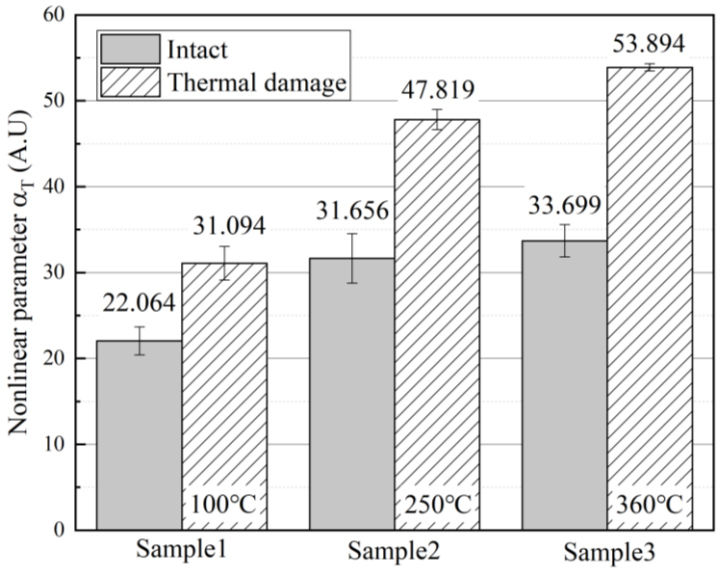

Fig.4-17 α_T of specimen 1, 2 and 3 under intact state and thermal damage state

4.3 Comparison of damage indexes

From Sections 3.1 and 3.2, it is found that the conventional linear parameters E_D and c_L, decrease when the temperature elevates, while the nonlinear parameters of proposed AMVA

methods are all increase. For better comparison, all the linear and nonlinear parameters are transferred into dimensionless index according to the following equation,

$$I = |\psi' - \psi_0|/\psi_0 \quad (4\text{-}13)$$

where I is the dimensionless index, ψ' is the parameter after thermal treatments (100℃, 250℃ and 360℃), and ψ_0 is the parameter at the intact state (25℃). It should be noted that ψ is a generic parameter that can be E_D, c_L, α_P, α_S and α_T.

Thus, the dimensionless index of conventional linear techniques and proposed nonlinear AMVA techniques are presented against the increasing temperatures in Fig.4-18. The dimensionless indexes of the proposed AMVA techniques are all larger than the conventional linear parameters after the specimens are subjected to high temperatures. It demonstrates that the proposed AMVA techniques are more sensitive than the conventional linear techniques. When comparing the nonlinear parameters of the AMVA techniques, the SAM method has the highest sensitivity. Meanwhile, the TAM method has a good correlation to the index of conventional techniques but it has a much higher sensitivity to thermal damages. In addition, it has the lowest energy consumption, according to the discussion in Section 3.2.1. However, even the PAM method is sensitive, particularly at the final state, the tendency of dimensionless index against elevated temperature drifts sharply. Hence, it is difficult to predict damages of the higher temperature by using PAM method. Therefore, according to the experimental results in this study, the SAM and TAM are more feasible and robust for characterizing the thermal damages in the cement-based material.

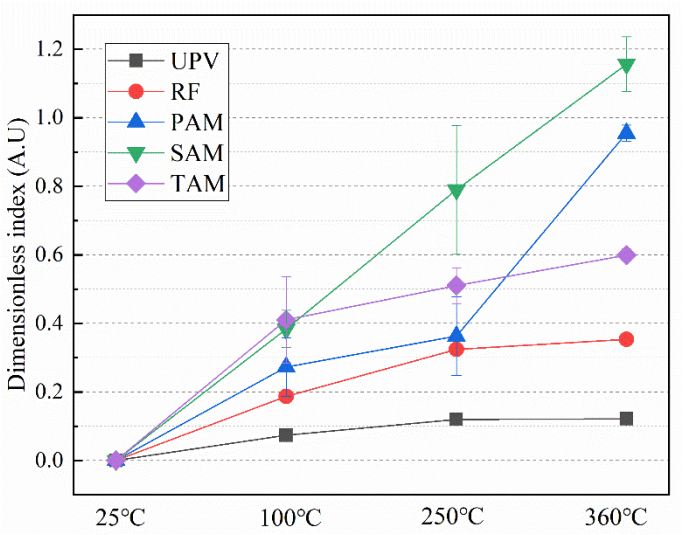

Fig.4-18. Comparison of damage indexes of conventional and proposed techniques

5. Conclusion

In this paper, three AMVA techniques, the PAM, SAM, and TAM methods, have been proposed to characterize the thermal damage of PGR mortar material. The nonlinear parameters of PAM, SAM and TAM method have been theoretically established and experimentally validated its correlation with thermal damages. Additionally, to further evaluate the effect of the proposed AMVA techniques, the conventional linear measurements obtained from the RF test and UPV test have been used to compare with the nonlinear acoustic results. The following conclusions have been drawn as follow:

1) Compared to the conventional VM techniques, the proposed AMVA technique has several advantages, including lower energy consumption and versatility by introducing a modulated pump wave, in which two different low-frequency force harmonic vibrations are combined and interacted in advance.
2) In this study, three different methods, PAM, SAM and TAM methods, of the proposed AMVA technique have been investigated. The emitting pump waves of the PAM, SAM and TAM methods are modulated according to Eq.(4-5)-(4-7). The relationships between nonlinear parameters and sideband generation have been extensively

established. These nonlinear parameters can serve as indicators of damages. In this study, for a better comparison of these three different methods of the proposed AMVA technique, the nonlinear parameters have been defined as the ratio of $\sum A_s$ and $A_H A_D$, where $\sum A_s$ is the sum of amplitudes of sidebands and $A_H A_D$ is the amplitude of probe frequency multiples amplitude of dominant pump frequency.

3) These three CMVA techniques have been demonstrated to be a practical and feasible method to qualify thermal damages in the PGR mortars. The nonlinear parameters α_P, α_S and α_T are found to have an increasing tend when the exposure temperature elevates. The sensitivity of the nonlinear parameters to thermal treatment is much higher compared with the linear measurements, E_D of RF test and c_L of UPV test.
4) The experimental results have suggested that the α_p , α_S and α_T are less affected by the reversible moisture content of specimens. It is because, at the range of $25℃ - 100℃$, when the moisture content changes intensely, the nonlinear parameters do not change that much. On the contrary, the nonlinear parameters have a noticeable increment at $360℃$, at which the most severe damages emerged. It indicates that the nonlinear parameters can detect and characterize the absolute defects and microcracks rather than having a critical effect by the moisture content.

Acknowledgement

Ms Tingyuan Yin's PhD scholarship is supported by China Scholarship Council. The support is greatly appreciated. The authors would like to thank technician, Jon Ayoub, for his help in the experimental work.

References

1. Roig-Flores M, Lucio-Martin T, Alonso MC, et al. Evolution of thermo-mechanical properties of concrete with calcium aluminate cement and special aggregates for energy storage. *Cement and Concrete Research* 2021; 141: 106323.

2. Meng T, Chen Y, Ying K, et al. Deterioration mechanism of concrete under long-term elevated temperature in a metallurgic environment: A case study of the Baosteel company. *Case Studies in Construction Materials* 2021; 14: e00503.

3. Zel IY, Kenessarin M, Kichanov S, et al. Spatial distribution of graphite in cement materials used for radioactive waste conditioning: An approach to analysis of neutron tomography data. *Cement and Concrete Composites* 2021; 119: 103993.

4. Ho VD, Ng C-T, Ozbakkaloglu T, et al. Investigating the reinforcing mechanism and optimized dosage of pristine graphene for enhancing mechanical strengths of cementitious composites. *RSC Advances* 2020; 10: 42777-42789.

5. Sedaghat A, Ram MK, Zayed A, et al. Investigation of physical properties of graphene-cement composite for structural applications. *Open journal of composite materials* 2014; 2014.

6. Li G and Zhang L. Microstructure and phase transformation of graphene-cement composites under high temperature. *Composites Part B: Engineering* 2019; 166: 86-94.

7. Chu H-y, Jiang J-y, Sun W, et al. Effects of graphene sulfonate nanosheets on mechanical and thermal properties of sacrificial concrete during high temperature exposure. *Cement and Concrete Composites* 2017; 82: 252-264.

8. Staszewski WJ. Structural health monitoring using guided ultrasonic waves. *Advances in smart technologies in structural engineering*. Springer, 2004, pp.117-162.

9. Van Den Abeele KE, Sutin A, Carmeliet J, et al. Micro-damage diagnostics using nonlinear elastic wave spectroscopy (NEWS). *Ndt & E International* 2001; 34: 239-248.

10. Kundu T, Eiras JN, Li W, et al. Fundamentals of nonlinear acoustical techniques and sideband peak count. *Nonlinear ultrasonic and vibro-acoustical techniques for nondestructive evaluation*. Springer, 2019, pp.1-88.

11. Allen JCP and Ng CT. Debonding detection at adhesive joints using nonlinear Lamb waves mixing. *NDT & E International* 2022; 125: 102552.

12. Aseem A and Ng CT. Debonding detection in rebar-reinforced concrete structures using second harmonic generation of longitudinal guided wave. *NDT & E International* 2021; 122: 102496.

13. Chen J, Yin T, Kim J-Y, et al. Characterization of thermal damage in sandstone using the second harmonic generation of standing waves. *International Journal of Rock Mechanics and Mining Sciences* 2017; 91: 81-89.

14. Yin T, Ng C-T and Kotousov A. Damage detection of ultra-high-performance fibre-reinforced concrete using a harmonic wave modulation technique. *Construction and Building Materials* 2021; 313: 125306.

15. Yang C and Chen J. Fully noncontact nonlinear ultrasonic characterization of thermal damage in concrete and correlation with microscopic evidence of material cracking. *Cement and Concrete Research* 2019; 123: 105797.

16. Nazarov VE, Ostrovsky LA, Soustova IA, et al. Nonlinear acoustics of micro-inhomogeneous media. *Physics of the Earth and Planetary Interiors* 1988; 50: 65-73.

17. Eiras J, Kundu T, Popovics J, et al. Cement-based material characterization using nonlinear single-impact resonant acoustic spectroscopy (NSIRAS). *Nonlinear Ultrasonic and Vibro-Acoustical Techniques for Nondestructive Evaluation*. Springer, 2019, pp.487-508.

18. Payan C, Garnier V, Moysan J, et al. Applying nonlinear resonant ultrasound spectroscopy to improving thermal damage assessment in concrete. *The Journal of the Acoustical Society of America* 2007; 121: EL125-EL130.

19. Yim HJ, Kim JH, Park S-J, et al. Characterization of thermally damaged concrete using a nonlinear ultrasonic method. *Cement and Concrete Research* 2012; 42: 1438-1446.

20. Donskoy DM and Sutin AM. Vibro-acoustic modulation nondestructive evaluation technique. *Journal of intelligent material systems and structures* 1998; 9: 765-771.

21. Donskoy D, Sutin A and Ekimov A. Nonlinear acoustic interaction on contact interfaces and its use for nondestructive testing. *Ndt & E International* 2001; 34: 231-238.

22. Parsons Z and Staszewski WJ. Nonlinear acoustics with low-profile piezoceramic excitation for crack detection in metallic structures. *Smart Materials and Structures* 2006; 15: 1110.

23. Yoder NC and Adams DE. Vibro-acoustic modulation utilizing a swept probing signal for robust crack detection. *Structural Health Monitoring* 2010; 9: 257-267.

24. Liu B, Luo Z and Gang T. Influence of low-frequency parameter changes on nonlinear vibro-acoustic wave modulations used for crack detection. *Structural Health Monitoring* 2018; 17: 218-226.

25. Zagrai A, Donskoy D, Chudnovsky A, et al. Micro/meso scale fatigue damage accumulation monitoring using nonlinear acoustic vibro-modulation measurements. In: *Testing, Reliability, and Application of Micro-and Nano-Material Systems IV* 2006, p.617506. International Society for Optics and Photonics.

26. Liu P, Sohn H and Jeon I. Nonlinear spectral correlation for fatigue crack detection under noisy environments. *Journal of Sound and Vibration* 2017; 400: 305-316.

27. Zhao N, Huo L and Song G. A nonlinear ultrasonic method for real-time bolt looseness monitoring using PZT transducer–enabled vibro-acoustic modulation. *Journal of Intelligent Material Systems and Structures* 2020; 31: 364-376.

28. He Q and Lin Y. Assessing the severity of fatigue crack using acoustics modulated by hysteretic vibration for a cantilever beam. *Journal of Sound and Vibration* 2016; 370: 306-318.

29. Solodov I, Wackerl J, Pfleiderer K, et al. Nonlinear self-modulation and subharmonic acoustic spectroscopyfor damage detection and location. *Applied physics letters* 2004; 84: 5386-5388.

30. Aymerich F and Staszewski W. Experimental study of impact-damage detection in composite laminates using a cross-modulation vibro-acoustic technique. *Structural Health Monitoring* 2010; 9: 541-553.

31. Kim S, Adams DE, Sohn H, et al. Crack detection technique for operating wind turbine blades using Vibro-Acoustic Modulation. *Structural Health Monitoring* 2014; 13: 660-670.

32. Ooijevaar T, Rogge MD, Loendersloot R, et al. Vibro-acoustic modulation–based damage identification in a composite skin–stiffener structure. *Structural health monitoring* 2016; 15: 458-472.

33. Meo M and Zumpano G. Nonlinear elastic wave spectroscopy identification of impact damage on a sandwich plate. *Composite structures* 2005; 71: 469-474.

34. Aymerich F and Staszewski WJ. Impact damage detection in composite laminates using nonlinear acoustics. *Composites Part A: Applied Science and Manufacturing* 2010; 41: 1084-1092.

35. Pieczonka L, Zietek L, Klepka A, et al. Damage imaging in composites using nonlinear vibro‐acoustic wave modulations. *Structural control and health monitoring* 2018; 25: e2063.

36. Chen J, Jayapalan AR, Kim J-Y, et al. Nonlinear wave modulation spectroscopy method for ultra-accelerated alkali-silica reaction assessment. *ACI Materials Journal* 2009; 106: 340.

37. Mahadevan S, Neal K, Nath P, et al. Quantitative diagnosis and prognosis framework for concrete degradation due to alkali-silica reaction. In: *AIP Conference Proceedings* 2017, p.080006. AIP Publishing LLC.

38. Karve P, Miele S, Neal K, et al. Vibro-acoustic modulation and data fusion for localizing alkali–silica reaction–induced damage in concrete. *Structural Health Monitoring* 2020; 19: 1905-1923.

39. Chen J, Wu Y, Yin T, et al. Characterization of concentrated and distributed cracks in concrete using a harmonic wave modulation technique. *Materials and Structures* 2018; 51: 1-10.

40. Miró M, Eiras JN, Poveda P, et al. Detecting cracks due to steel corrosion in reinforced cement mortar using intermodulation generation of ultrasonic waves. *Construction and Building Materials* 2021; 286: 122915.

41. Klepka A, Pieczonka L, Dziedziech K, et al. Structural damage detection based on nonlinear acoustics: application examples. *Nonlinear Ultrasonic and Vibro-Acoustical Techniques for Nondestructive Evaluation*. Springer, 2019, pp.139-174.

42. Thurston R and Shapiro M. Interpretation of ultrasonic experiments on finite‐amplitude waves. *The Journal of the Acoustical Society of America* 1967; 41: 1112-1125.

43. Van Den Abeele KEA. Elastic pulsed wave propagation in media with second‐or higher‐order nonlinearity. Part I. Theoretical framework. *The Journal of the Acoustical Society of America* 1996; 99: 3334-3345.

44. Vidler J, Kotousov A and Ng C-T. Effective elastic properties of a weakly nonlinear particulate composite. *International Journal of Non-Linear Mechanics* 2022; 141: 103949.

45. Kim J-Y, Jacobs L and Qu J. Nonlinear ultrasonic techniques for material characterization. *Nonlinear ultrasonic and vibro-acoustical techniques for nondestructive evaluation*. Springer, 2019, pp.225-261.

46. ASTM C215-19 Standard Test Method for Fundamental Transverse, Longitudinal, and Torsional Resonant Frequencies of Concrete Specimens.

47. ASTM C597-09 Standard Test Method for Pulse Velocity Through Concrete.

48. Moreno-Navarro F, Sol-Sánchez M, Gámiz F, et al. Mechanical and thermal properties of graphene modified asphalt binders. *Construction and Building materials* 2018; 180: 265-274.

49. Tantawy M. Effect of high temperatures on the microstructure of cement paste. *Journal of Materials Science and Chemical Engineering* 2017; 5: 33.

50. Farage M, Sercombe J and Galle C. Rehydration and microstructure of cement paste after heating at temperatures up to 300 C. *Cement and Concrete Research* 2003; 33: 1047-1056.

51. Ouyang J, Zhao J and Tan Y. Modeling mechanical properties of cement asphalt emulsion mortar with different asphalt to cement ratios and temperatures. *Journal of Materials in Civil Engineering* 2018; 30: 04018263.

52. Alarcon-Ruiz L, Platret G, Massieu E, et al. The use of thermal analysis in assessing the effect of temperature on a cement paste. *Cement and Concrete research* 2005; 35: 609-613.

53. Alizadeh R, Beaudoin JJ and Raki L. Mechanical properties of calcium silicate hydrates. *Materials and Structures* 2011; 44: 13-28.

54. Gallé C and Sercombe J. Permeability and pore structure evolution of silicocalcareous and hematite high-strength concretes submitted to high temperatures. *Materials and Structures* 2001; 34: 619-628.

55. Qiu Z, Chen Y, Kang Y, et al. Investigation into Periodic Signal-based Dithering Modulations for Suppression Sideband Vibro-acoustics in PMSM Used by Electric Vehicles. *IEEE Transactions on Energy Conversion* 2020; 36: 1787-1796.

56. He Y, Xiao Y, Su Z, et al. Contact acoustic nonlinearity effect on the vibro-acoustic modulation of delaminated composite structures. *Mechanical Systems and Signal Processing* 2022; 163: 108161.

Chapter 5

Higher-order effects of amplitude-modulated vibro-acoustic technique for characterization thermal damages in graphene mortar materials

This chapter is based on the following published paper:

Yin, T., Ng, C.T., Vidler, J., Ho, V.D. and Kotousov, A., Characterization of Thermal Damage in Graphene Mortar Materials Using High-order Sideband Generation of Amplitude-modulation Vibro-acoustic Technique.

Statement of Authorship

Title of Paper	Higher-order effects of amplitude-modulated vibro-acoustic technique for characterization thermal damages in graphene mortar materials
Publication Status	☐ Published ☐ Accepted for Publication ☑ Submitted for Publication ☐ Unpublished and Unsubmitted w ork w ritten in manuscript style
Publication Details	Yin, Tingyuan, Ching Tai Ng, James Vidler, Van Dac Ho, and Andrei Kotousov. " Higher-order effects of amplitude-modulated vibro-acoustic technique for characterization thermal damages in graphene mortar materials"

Principal Author

Name of Principal Author (Candidate)	Tingyuan Yin		
Contribution to the Paper	Conceptualization, Methodology, Writing – original draft, Data curation		
Overall percentage (%)	80%		
Certification:	This paper reports on original research I conducted during the period of my Higher Degree by Research candidature and is not subject to any obligations or contractual agreements with a third party that would constrain its inclusion in this thesis. I am the primary author of this paper.		
Signature		Date	22/09/2022

Co-Author Contributions

By signing the Statement of Authorship, each author certifies that:

i. the candidate's stated contribution to the publication is accurate (as detailed above);

ii. permission is granted for the candidate in include the publication in the thesis; and

iii. the sum of all co-author contributions is equal to 100% less the candidate's stated contribution.

Name of Co-Author	Ching-Tai Ng		
Contribution to the Paper	Conceptualization, Supervision, Writing – review & editing		
Signature		Date	23/09/2022

Name of Co-Author	James Vidler		
Contribution to the Paper	Methodology, Validation, Formal analysis		
Signature		Date	27/09/2022

Name of Co-Author	Van Dac Ho		
Contribution to the Paper	Validation, Investigation, Resources		
Signature		Date	27/09/2022

Name of Co-Author	Andrei Kotousov		
Contribution to the Paper	Conceptualization, Supervision, Writing – review & editing		
Signature		Date	23/09/2022

Please cut and paste additional co-author panels here as required.

Characterization of Thermal Damage in Graphene Mortar Materials Using High-order Sideband Generation of Amplitude-modulation Vibro-acoustic Technique

Tingyuan Yin[1], Ching Tai Ng[1,*], James Vidler[2], Van Dac Ho[1], Andrei Kotousov[2]

[1] School of Civil, Environmental and Mining Engineering, The University of Adelaide, Adelaide, SA 5005, Australia

[2] School of Mechanical Engineering, The University of Adelaide, Adelaide SA 5005, Australia

Abstract

In this paper, an amplitude-modulated vibro-acoustic (AMVA) technique using a transmitted amplitude-modulated pump wave to achieve lower power consumption and versatility is proposed to characterize different thermal damage levels of pristine graphene mortar specimens with various dosages. In previous studies, only primary field u_1 and secondary field u_2 were considered in the theoretical model. Hence, some higher-order sidebands were not included even though they are frequently presented in experimental results and useful for damage detection purposes. Therefore, a theoretical model containing higher-order effects is established to include those higher-order sidebands. A nonlinear parameter β is defined based on this theoretical model and experimental results demonstrated that β is feasible and sensitive to characterize thermal damages as well as distinguish various dosages of cement-based materials when compared to the results of the conventional resonant frequency technique. Therefore, AMVA technique has great potential to be a reliable and efficient technique for evaluating microstructural changes in cement-based materials.

* Corresponding author: alex.ng@adelaide.edu.au

Keywords: vibro-acoustic, amplitude-modulation, higher-order effect, nonlinearity, pristine graphene, mortar, cement-based material, high-temperature, NDT, SHM.

1. Introduction

Cement-based material is one of the most popular construction materials, which is also the major material for some particular structures, e.g., tunnels, nuclear power plants, and radioactive waste storage. Thermal damages caused by unexpected fires or long-term high-temperature conditions threaten the life of structures, as it adversely affects the mechanical properties and durability of cement-based materials [1-3]. There are mainly two approaches to minimize the impact of thermal damage in cement-based materials: (i) utilizing practical strategies to decrease thermal stress, such as applying surface insulation and cooling pipes; (ii) focusing on enhancing the crack-arrest capability of cement-based materials by adding fibers or additives [4]. The first approach is proposed with regard to practical construction skills, whereas it brings difficulties for construction and increases costs. Therefore, the second approach that concerns strengthening cement-based materials has motivated much research in recent years [5, 6]. Some studies improved the thermal properties of cement-based materials by incorporating pristine graphene or graphene derivatives in cement composites [7-9]. Compared to plain cement-based materials, cement composites with graphene have a more compact matrix, lower porosity, and higher thermal diffusivity against fire and long-term high-temperature service environments [10-12].

Even though the thermal properties of cement-based materials are improved, there is still a powerful incentive to develop the non-destructive evaluation (NDE) and structural health monitoring (SHM) techniques for assessing the structural damages after fire accidents and monitoring the accumulation of thermal damages under in-service high-temperature conditions. Current practice for inspecting structures made by cement-based materials relies on conventional NDE and SHM methods, e.g., rebound method and ultrasonic pulse velocity method. However, the conventional approaches are limited to detecting damage that has reached the macro-scale, and they are incapable of characterizing the early-state damage of

micro-scale [13-15]. Examples of promising techniques that are sensitive to evaluate the degradation of materials and microscopic damages are the nonlinear acoustical and ultrasonic techniques [16]. Recent research has discovered that ultra-tiny damage can produce detectable acoustic nonlinearity, which can provide damage detection of micro-damages in the early state until macro-scale damages result in structural failure [17-19]. The nonlinear vibro-acoustic (VA) technique is one of the promising acoustical techniques that enables the assessment of micro-scale defects and damages.

1.1 Conventional vibro-acoustic technique

In the conventional nonlinear VA technique, a high-frequency (HF) wave and a low-frequency (LF) wave are simultaneously introduced into the monitored structures. When the structures are linear (e.g., undamaged or integrity), the receiving signals only contain two frequency components, i.e., f_H (HF) and f_L (LF). For the nonlinear structures (e.g., due to material degradation or cracks), the response frequencies differ from the input frequencies f_H and f_L, as a result of the nonlinear transformation of the input energy. In the spectrum of nonlinear structures, some extra frequency components appeal at $f_H \pm nf_L$, nf_H and nf_L ($n = 1,2,3$ ...). The components $f_H \pm nf_L$ are sidebands while nf_H and nf_L are higher-order harmonics. In the conventional VA technique, the measurement is usually expressed in terms of the nonlinear parameter related to the numbers and amplitudes of sidebands [20-22]. In addition, utilizing sidebands can avoid the nonlinearity caused by the amplifier, transducer, and coupling mechanisms [23].

The selection of LF wave, including source and frequency, is a critical process for applying the VA technique. The source of the LF wave can be divided into two alternative methods: i) the impact method or ii) the forced method [24]. For the impact method, the

structure is struck with an impactor, where f_L is the resonant response of the structure. In the force method, the structure is forced to vibrate by an electro-mechanical driving unit, and the LF pump wave is usually a simple harmonic wave at a constant frequency f_L.

However, the resonant response is normally accompanied by multiple modes in the impact method. This means there is not only one resonant frequency, but several frequencies of multiple modes appear from the LF source. Hence, identifying the accurate frequencies of sidebands is challenging because all the modal responses affect the modulation of sidebands, which are easily masked by the aliasing effect of signal processing. Additionally, in the forced method, transmitting LF pump waves generally cause a significant burden for the electro-mechanical driving unit, particularly for ultra low-frequency range or for long-term monitoring. Therefore, the deficiencies mentioned above provide a powerful impetus to develop the conventional VA technique to achieve more robustness, applicability, and energy-saving.

1.2 Amplitude-modulated vibro-acoustic technique

In the literature, some studies investigated the approaches to improve VA techniques. Solodov *et al*. investigated the self-modulation mode of nonlinear acoustic vibration to assess cracked defects due to cyclic-loading fatigue in Ni-base superalloy plates. Their study found that both sub-harmonic and self-modulation modes showed high sensitivity to the localization of defects [25]. Zaitsev *et al*. proposed a novel nonlinear-modulation VA method for crack detection, including thermally-produced cracks in a glass rod and artificial crack-like defects on a thick glass plate. The results indicated that the probe wave with high enough amplitudes would perturb the state of the contacts, hence, the additional pump action is not as strong influence as the case of weak probe wave [26]. Aymerich *et al*. [27] conducted experiments on a laminated composite plate with impact damage, and Trojniar *et al*. [28] detected fatigue damage on an

aluminum plate by using a cross-modulation VA method, in which they found that the Luxembourg-Gorky effect was observed in solids. Kim *et al.* developed the VA technique by utilizing operational loads of wind turbines as LF pump excitation signals to achieve long-term SHM during the operation of the wind turbine system [29]. Liu *et al*. used a wide-band HF probing wave instead of a monochromatic HF probing wave for VA technique to assess the fatigue crack on a thick aluminum plate. The experimental results implied that the wide-band HF input increases the sensitivity to the defects, decreases the effect of stationary noises, and reduces the data collection time [30]. Swept-signal was applied as the HF probe wave in VA technique, meanwhile the resonance frequency was used as the frequency of the pump wave to make this method more sensitive [31, 32]. Bispectrum was applied to analyze the response data from VA technique by Czeluśniak *et al*. [33], which makes the results significantly less noisy, producing less spurious peaks and easy to interpret. Dorendorf *et al*. demonstrated the appearance of modulation in VA technique due to local and global nonlinearity by introducing a physical explanation and validating it through FE simulation [34]. Alnuaimi *et al.* [35], Arumaikani *et al.* [36] and Basu *et al.* [37] used a new sideband peak count-Index (SPC-I) technique for sensing damage in thermoplastic resin composite plate, corrosion and bending-induced damage of the reinforcing steel in concrete, respectively. Furthermore, Castellano et al. applied SPC technique to monitor stress-induced damage in concrete with coarse-grained aggregates [38]. Additionally, machine learning [39, 40] was introduced for the VA technique to automate the threshold selection, increase the efficiency of the probabilistic damage diagnosis process, and allow estimation of the damage level of VA-based damage.

Recently, an amplitude-modulated vibro-acoustic (AMVA) technique was proposed [27, 41]. Different from the conventional VA technique using the monochromatic LF pump wave, the AMVA technique applies a pre-amplitude-modulated LF wave as the pump wave, which contains two low frequencies f_{L1} and f_{L2}. In the frequency domain, the sidebands

present at $f_H \pm nf_{L1} \pm nf_{L2}$ ($n = 1,2,3 \ldots$) when the medium is nonlinear. The AMVA technique can be classified into the pure amplitude-modulated (PAM) method, suppressed amplitude-modulated (SAM) method, and transmitted amplitude-modulated (TAM) method [42], according to the different amplitude-modulated approaches of LF pump wave. The amplitude-modulated pump wave has the following advantages in the AMVA technique: i) having a wider frequency range of LF emitter without changing the hardware and having advantages of the amplitude-modulated methods, ii) being more energy-efficient and practical, iii) sensitive to damages [43].

Besides the general procedures of the aforementioned AMVA technique, some analytical approaches to damage modeling were also proposed. There are usually two distinct types of nonlinearity: i) localized nonlinearity and ii) distributed nonlinearity. The localized nonlinearity is typically related to crack-wave interaction and contact models, while the distributed nonlinearity affects the governing equations (*e.g.*, higher-order elements in Hooke's law) in global sense [44]. Yin *et al.* [43] established a contact model to investigate the HF probe wave and the pre-mixed LF pump wave of TAM method propagating through a concentrated crack, at which the interaction of waves was caused by the localized nonlinearity. In another paper [42], the theoretical framework of PAM, SAM, and TAM method was proposed, where nonlinear features appear due to distributed nonlinearity. The nonlinear parameters of PAM, SAM, and TAM method were derived from the nonlinear elastic wave propagation equations in continuous media.

The previous studies only consider the second-order effect of AMVA technique. However, it is interesting to find that some sidebands, which are not obtained from the wave equation only with second-order effect, present in frequency domain of experimental results at a quite early-damage state. Additionally, when the damage accumulates to a certain level, these sidebands cannot be omitted due to their distinct amplitudes. Therefore, it is necessary to

develop the theoretical approach to expand the quasi-linear equation to higher order in order to well describe the experimental observation and build a more comprehensive nonlinear parameter for AMVA technique.

In this study, the pristine graphene (PRG) mortars with various PRG sizes, both at ambient and elevated temperatures, were evaluated by the TAM method of the AMVA technique. Furthermore, a theoretical model is proposed to describe the elastic nonlinearity caused by global thermal damage, in which frequency components mix and energy transfer from the fundamental three frequencies to sum and difference frequencies along with the wave propagation. It should be noted that a polynomial expansion of the equation is used, from which higher-order harmonics and sidebands are derived. The contributions of this paper are as follows:

- A theoretical model taking into account of higher-order effects for TAM method of AMVA technique is proposed for the first time.
- A nonlinear parameter of TAM method considering higher-order sidebands is defined. The feasibility and effectiveness of the nonlinear parameter are validated through a series of experiments.
- Research investigating the application of AMVA technique on cement-based materials was relatively few in the literature. However, cement-based materials are large-consuming, and they are a combined material with complex properties. In particularly, the studies demonstrate that AMVA technique can distinguish the different dosages of cement-based materials is very limited. Therefore, it is worth to investigate the application of the AMVA technique to cement-based materials with different dosages.

2. The mechanism of amplitude-modulated vibro-acoustic technique

In this section, quadratic and cubic nonlinearity is considered for wave propagation in isotropic elastic material to explore the distributed nonlinearity on the fundamental waves and higher-order harmonics and sidebands. Explicit expressions of the nonlinear parameters are given. Lastly, a nonlinear parameter is defined considering the relationship between fundamental waves and higher-order sidebands. This nonlinear parameter is utilized to detect thermal damages in Section 3.

2.1 The formulation and solution of higher-order modulation equation

Consider the governing equation for a single-mode elastic wave propagating in a nonlinear one-dimensional infinite solid written in the Lagrangian coordinate [45],

$$\frac{\partial^2 u}{\partial t^2} = c^2[1 - \beta\frac{\partial u}{\partial x} - \gamma\left(\frac{\partial u}{\partial x}\right)^2]\frac{\partial^2 u}{\partial x^2} \tag{5-1}$$

where u is the particle displacement, t is the time, x is the Lagrangian coordinate, and c is the linear wave velocity. β and γ are the nonlinear parameter. β contains the third-order elastic constant while γ includes the fourth-order elastic constant.

By using the perturbation theory, the solution of Eq.(1) can be written as,

$$u = u_1 + u_2 + u_3 \tag{5-2}$$

u_1, u_2 and u_3 satisfying $u_1 \gg u_2 \gg u_3$.

Inserting Eq.(5-2) into Eq.(5-1), then Eq.(5-1) can be decoupled into,

$$\frac{\partial^2 u_1}{\partial t^2} - c^2\frac{\partial^2 u_1}{\partial x^2} = 0 \tag{5-3a}$$

$$\frac{\partial^2 u_2}{\partial t^2} + c^2\beta\frac{\partial u_1}{\partial x}\frac{\partial^2 u_1}{\partial x^2} - c^2\frac{\partial^2 u_2}{\partial x^2} = 0 \tag{5-3b}$$

$$\frac{\partial^2 u_3}{\partial t^2} + c^2\gamma\left(\frac{\partial u_1}{\partial x}\right)^2\frac{\partial^2 u_1}{\partial x^2} + c^2\beta\frac{\partial u_2}{\partial x}\frac{\partial^2 u_1}{\partial x^2} + c^2\beta\frac{\partial u_1}{\partial x}\frac{\partial^2 u_2}{\partial x^2} - c^2\frac{\partial^2 u_3}{\partial x^2} = 0 \tag{5-3c}$$

u_2 is driven by u_1, and u_3 is driven by u_1 and u_2. The solution for u_1 is not affected by the nonlinearity, hence, u_1 is the same as the input signal of TAM method of AMVA technique as shown below,

$$u_1 = A_H\cos(\omega_H\tau + \phi_H) + A_{L2}\cos(\omega_{L2}\tau + \phi_{L2})[1 + A_{L1}\cos(\omega_{L1}\tau + \phi_{L1})] \tag{5-4}$$

In the TAM method of AMVA technique, the input signals include a HF probe wave $A_H\cos(\omega_H\tau + \phi_H)$, and a LF amplitude-modulated pump wave pre-mixed by $A_{L1}\cos(\omega_{L1}\tau + \phi_{L1})$ and $A_{L2}\cos(\omega_{L2}\tau + \phi_{L2})$, where A denotes the amplitude of signal, ω is the angular frequency, and ϕ indicates the phase. The subscript H presents the HF probe wave, and $L1$ and $L2$ denote the two LF pump wave used for amplitude modulation, where $\omega_{L1} < \omega_{L2} < \omega_H$. It should be noted that the pre-mixed pump wave is the part $A_{L2}\cos(\omega_{L2}\tau + \phi_{L2})[1 + A_{L1}\cos(\omega_{L1}\tau + \phi_{L1})]$ as shown in Eq.(5-4).

Solving u_2 by inserting Eq.(5-4) into Eq.(5-3b), and then substituting u_1 and u_2 into Eq.(5-3c), the explicit expression of u_3 can be solved. The total derivation of u_2 and u_3 can be found in Appendix A. The purpose of the derivation is to explore the relationship between the sidebands and fundamental waves, and hence, to obtain a nonlinear parameter for damage evaluation. Therefore, the static components and the higher-order harmonics are omitted when presenting the final solution of u_2 and u_3 as shown in Eq.(5-5). But it should be noted that the static components and the higher-order harmonics are used in the derivation.

$$u_2 + u_3 = \sum_{i=1}^{2}\{(-1)^{i+1}\frac{A_H A_{L2}}{4c^2}x\beta\omega_H\omega_{L2}\cos\left[\left(\omega_H + (-1)^i\omega_{L2}\right)\tau + \left(\phi_H + (-1)^i\phi_{L2}\right)\right] \tag{5-5}$$

$$+\frac{A_H A_{L1} A_{L2}^2}{16c^2} x\beta^2 \omega_H \omega_{L2}^2 \, \xi_{(H\pm L1)} \sin\big[\big(\omega_H + (-1)^i \omega_{L1}\big)\tau + \big(\phi_H + (-1)^i \phi_{L1}\big) + \varphi_{(H\pm L1)}\big]$$

$$+\frac{A_H A_{L2}^2}{64c^2} x\beta^2 \omega_H |2\omega_{L2}^2 + A_{L1}^2(\omega_{L2}^2 - \omega_{L1}^2)| \, \xi_{(H\pm 2L2)} \sin[\,\big(\omega_H + (-1)^i 2\omega_{L2}\big)\tau + (\phi_H + (-1)^i 2\phi_{L2}) + \varphi_{(H\pm 2L2)}]$$

$$+\frac{A_H A_{L1}^2 A_{L2}^2}{64c^2} x\beta^2 \omega_H (\omega_{L2}^2 - \omega_{L1}^2) \, \xi_{(H\pm 2L1)} \sin[\big(\omega_H + (-1)^i 2\omega_{L1}\big)\tau + (\phi_H + (-1)^i 2\phi_{L1}) + \varphi_{(H\pm 2L1)}]$$

$$-\frac{A_H A_{L1} A_{L2}}{8c^2} x\beta \omega_H \big[\omega_{L2} + (-1)^i \omega_{L1}\big] \cos[\big(\omega_H + \omega_{L2} + (-1)^i \omega_{L1}\big)\tau + (\phi_H + \phi_{L2} + (-1)^i \phi_{L1})]$$

$$+\frac{A_H A_{L1} A_{L2}}{8c^2} x\beta \omega_H \big[\omega_{L2} + (-1)^{i+1} \omega_{L1}\big] \cos[\big(\omega_H - \omega_{L2} + (-1)^i \omega_{L1}\big)\tau + (\phi_H - \phi_{L2} + (-1)^i \phi_{L1})]$$

$$+\frac{A_H A_{L1} A_{L2}^2}{32c^2} x\beta^2 \omega_H \omega_{L2} \big|\omega_{L1} + (-1)^i \omega_{L2}\big| \, \xi_{(H+2L2\pm L1)} \sin[\big(\omega_H + 2\omega_{L2} + (-1)^i \omega_{L1}\big)\tau + (\phi_H + 2\phi_{L2} + (-1)^i \phi_{L1}) + \varphi_{(H+2L2\pm L1)}]$$

$$+\frac{A_H A_{L1} A_{L2}^2}{32c^2} x\beta^2 \omega_H \omega_{L2} \big|\omega_{L1} + (-1)^{i+1} \omega_{L2}\big| \, \xi_{(H-2L2\pm L1)} \sin[\big(\omega_H - 2\omega_{L2} + (-1)^i \omega_{L1}\big)\tau + (\phi_H - 2\phi_{L2} + (-1)^i \phi_{L1}) + \varphi_{(H-2L2\pm L1)}]$$

$$+\frac{A_H A_{L1}^2 A_{L2}^2}{128c^2} x\beta^2 \omega_H \omega_{L2} (\omega_{L1} + (-1)^i \omega_{L2})^2 \, \xi_{(H+2L2\pm 2L1)} \sin[\big(\omega_H + 2\omega_{L2} + (-1)^i 2\omega_{L1}\big)\tau + (\phi_H + 2\phi_{L2} + (-1)^i 2\phi_{L1}) + \varphi_{(H+2L2\pm 2L1)}]$$

$$+\frac{A_H A_{L1}^2 A_{L2}^2}{128c^2} x\beta^2 \omega_H \omega_{L2} (\omega_{L1} + (-1)^{i+1} \omega_{L2})^2 \, \xi_{(H-2L2\pm 2L1)} \sin[\big(\omega_H - 2\omega_{L2} + (-1)^i 2\omega_{L1}\big)\tau + (\phi_H - 2\phi_{L2} + (-1)^i 2\phi_{L1}) + \varphi_{(H-2L2\pm 2L1)}]\}$$

where ξ is the variable, and its subscript indicates the corresponding sidebands. For instance, $\xi_{H\pm L2}$ is the variables of sidebands at the frequency $f_H + f_{L2}$ and $f_H - f_{L2}$. Because it assumes

no attenuation in the isotropic elastic media, the group of sidebands (e.g., $f_H + f_{L2}$ and $f_H - f_{L2}$) is expected to be symmetric. Additionally, φ is the phase of the wave after propagation, and the subscript represents its sideband order. The details of ξ and φ are provided in Appendix A. Furthermore, the frequency components derived from u_2 and u_3 are summarized in Table 5-1.

Table 5-1 Extra frequency components due to material nonlinearity

Catalog	Analytical Solution of u_2	Analytical Solution of u_3
Direct component	ω_{L1}	ω_H, ω_{L2}
Harmonics	$2\omega_H, 2\omega_{L2}, 2\omega_{L1}$	$3\omega_H, 3\omega_{L2}, 3\omega_{L1}$
Sidebands	$\omega_H \pm \omega_{L2}$ $\omega_H \pm \omega_{L2} \pm \omega_{L1}$	$\omega_H \pm \omega_{L1}$ $\omega_H \pm 2\omega_{L1}$ $\omega_H \pm 2\omega_{L2}$ $\omega_H \pm 2\omega_{L2} \pm \omega_{L1}$ $\omega_H \pm 2\omega_{L2} \pm 2\omega_{L1}$

2.2 Definition of the nonlinear parameter of amplitude-modulated vibro-acoustic technique

In Eq.(5-5), it is interesting to find that all sideband components are related to A_H and A_{L2} ($\omega_{L1} < \omega_{L2}$). Therefore, a nonlinear parameter of TAM method for AMVA technique can be defined as below,

$$\beta \sim \frac{\sum A_s}{A_H A_{L2}} \tag{5-6}$$

where A_s is the amplitude of sideband components.

For better comparison of β that considered second order effect and third order effect, $\beta^{(2)}$ and $\beta^{(2+3)}$ are defined. $\beta^{(2)}$ is based on the second-order effect is,

$$\beta^{(2)} \sim \frac{\sum (A_s^{(\omega_H \pm \omega_{L2})} + A_s^{(\omega_H \pm \omega_{L2} \pm \omega_{L1})})}{A_H A_{L2}} \tag{5-7}$$

While the definition of $\beta^{(2+3)}$ based on the second-order and third-order effect is,

$$\beta^{(2+3)} \sim \beta^{(2)} + \frac{\sum(A_S^{(\omega_H \pm \omega_{L1})} + A_S^{(\omega_H \pm 2\omega_{L2})} + A_S^{(\omega_H \pm 2\omega_{L1})} + A_S^{(\omega_H \pm 2\omega_{L2} \pm \omega_{L1})} + A_S^{(\omega_H \pm 2\omega_{L2} \pm 2\omega_{L1})})}{A_H A_{L2}} \quad (5\text{-}8)$$

3. Experimental study

3.1 Specimens

The physical properties of two kinds of PRGs are shown in Table 5-2. The ordinary Portland cement (OPC) of mortar mixes was produced by Adelaide Brighton Cement LTD following Australian Standard AS 3972-2010 [46]. Nature sands with 2.36 mm maximum particle size was used as the fine coarse. MasterGlenium SKY 8100 complying with Australian Standard AS 1478.1-2000 [47] was utilized as the superplasticizer.

Table 5-2 Physical properties of different PRG

Group	Particle (μm)	Thickness (nm)	Purity (%)	Pour bulk density (g/cm^3)
Mix1	43	1-3	98	0.13
Mix2	73	1-3	98	0.12

Table5-3 Designed mixed of PRG mortar specimens

Group	Specimen ID	PRG (%)	PRG size (μm)	Cement (kg/m^3)	Water (kg/m^3)	Sand (kg/m^3)	Superplasticizer (kg/m^3)
Mix1	M1S1 M1S2 M1S3	0.07	43	527	255.6	1448	1.4
Mix2	M2S1 M2S2 M2S3	0.07	73	527	255.6	1448	1.4

*The percentage of PRG based on the weight of cement binder.

The designed mixes of PRG mortar specimens were based on previous studies investigating optimized PRG dosage for improvement of mechanical strength [11, 48]. The details are presented in Table 5-3. After preparing all the materials of mixtures, the aqueous

solution, including PRGs, superplasticizer, and water, was first sonicated by Ultrasonication UIP1000hdT for 30 min for better dispersion of PRGs. The dry mixture consisted of the OPC, and natural sand was sufficiently mixed for 4 min, and then the aqueous solution was gradually and steadily added to the dry mixture for 5 min. All mixtures were poured into $40\text{mm} \times 40\text{mm} \times 180\text{mm}$ molds and then vibrated for 1 min to get rid of entrapped air. There were three PRG mortar specimens in each designed mixed, and their marks were shown in the Specimen ID column in Table 5-3. All the specimens were covered by wet fabrics and plastic sheets to keep moisture. After 24 hours, the specimens were demounted and left in the fog room where the environmental conditions were constant ($23 \pm 2℃$ and humidity $> 95\%$) for curing until testing.

3.2 Thermal experiment

Before conducting the thermal experiments, all the specimens were taken out of the fog room and left in the ambient environments ($23 \pm 2℃$ and humidity $45 \pm 5\%$) until the masses of the specimens were kept constant. After that, M1S1 and M2S1 were grouped together to be heated to 100℃. In addition, M1S2 and M2S2, and M1S3 and M2S3 were grouped, and their target heating temperature was 250℃ and 360℃, respectively. These groups of specimens were heated by an electrical muffle furnace (Elite BSF 12/22A) with a $5℃/\text{min}$ heating rate. When the furnace reached the target temperatures, the specimens were kept at constant target temperatures for two hours. Then the specimens were at ambient conditions until their temperatures and masses were no longer changed. In addition, three $20mm \times 20mm \times 20mm$ cubic specimens of Mix1 and Mix2 were prepared and taken photos by a microscope (OLYMPUS) before and after high-temperature treatments to track the changes of micro-cracks.

3.3 Experiment of resonant frequency technique following ASTM C215-19

Experiments following ASTM C215-19 were used to i) obtain the dynamic elastic modulus E_d of PRG mortar specimens exposure to different high temperatures and ii) compare E_D with the nonlinear parameter β of the proposed AMVA technique. All the tests followed ASTM C215-19 [49], which covered the measurement of the fundamental longitudinal frequency n' of PRG mortar bar for the purpose of obtaining E_d. In this study, the impact resonance method was selected as the procedure, in which the supported PRF mortar specimen was struck with an impactor hammer, and the specimen response was received by an accelerometer (SN#578) on the specimen. The signal was then fed into the coupler (KISTLER type 5134B) and converted into a digital signal through the data acquisition unit (DAQ NI USB 6281) with 20 kHz sampling rate. Additionally, n' obtaining from the resonant frequency test were used as the reference to select the frequency of the pump wave in the AMVA experiments.

3.4 Experiment of amplitude-modulated vibro-acoustic technique

3.4.1 Experimental set-up

The schematic set-up of AMVA technique is displayed in Fig.5-1. A LF amplitude-modulated pump wave pre-mixed according to Eq.(5-4), and its frequencies were $f_{L1} = 0.5$ kHz and $f_{L2} =$ 5.7 kHz, which were selected by a series of resonant frequency tests. This pump wave was transmitted to the signal generator (NI PXI-5412) and then fed into the power amplifier (Brüel & Kjær 2718) to be magnified to 20 dB. Afterward, this pump wave was sent to an electromagnetic shaker and transmitted to the PRG specimen. It should be noted that i) a designed clamp was made by the 3D printer to connect the rod of shaker and specimen for the purpose of ensuring the pump signal entirely and steadily be emitted, and ii) a soft foam was

laid below the specimen to increase the flexibility of the vibration, as shown in Fig.5-2(a). The end of the rod was sharpened as a pinpoint to effectively reduce the distortion caused by uneven contact and to ensure the effective connection between the rod of the shaker and the specimen. In addition, a HF probe wave at $f_H = 50$ kHz was generated by the functional generator (Tektronix AFG 302113). The HF probe signal was transmitted to the signal amplifier (Krohn Hite Model 7500) and then emitted by the emitting transducer (GOW•RLD 50K-P40F) with 50 kHz central frequency. A coupling glue (Dow Corning vacuum silicone grease) was used to bond the surfaces between transducers and specimen. Finally, both LF pump wave and HF probe wave were emitted simultaneously and received by another non-mental transducer. The receiving signal was transmitted to the digitizer (NI PXI-5105 12bit) and converted into a digital signal for further analysis. It is important to note that the peak-to-peak voltage of the pump wave was kept constant during the experiments while the voltage of the probe wave gradually increased at a steady rate.

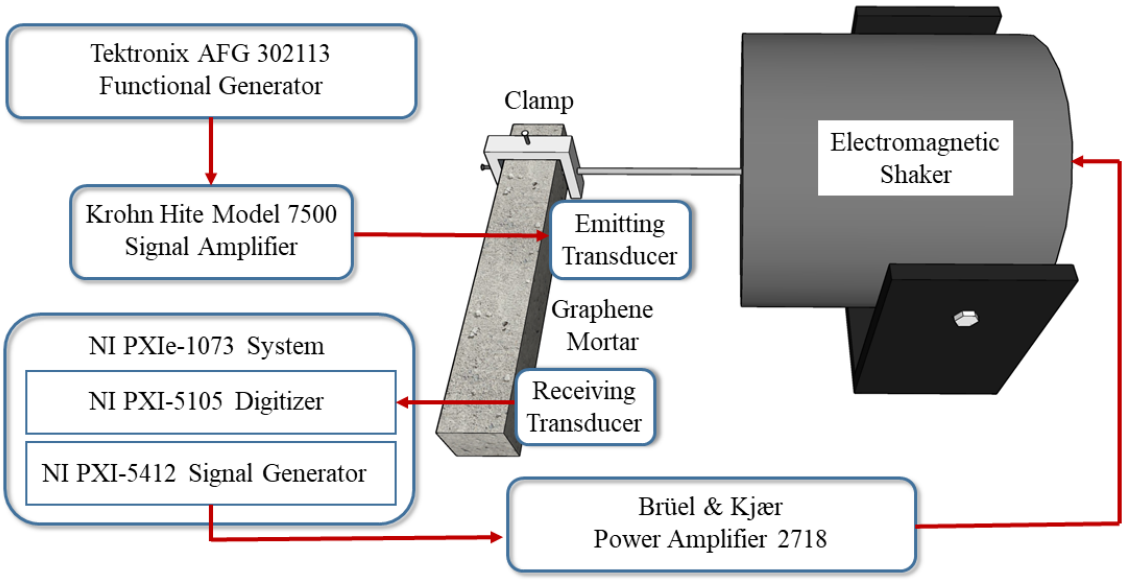

Fig.5-1 Schematic set-up of AMVA technique

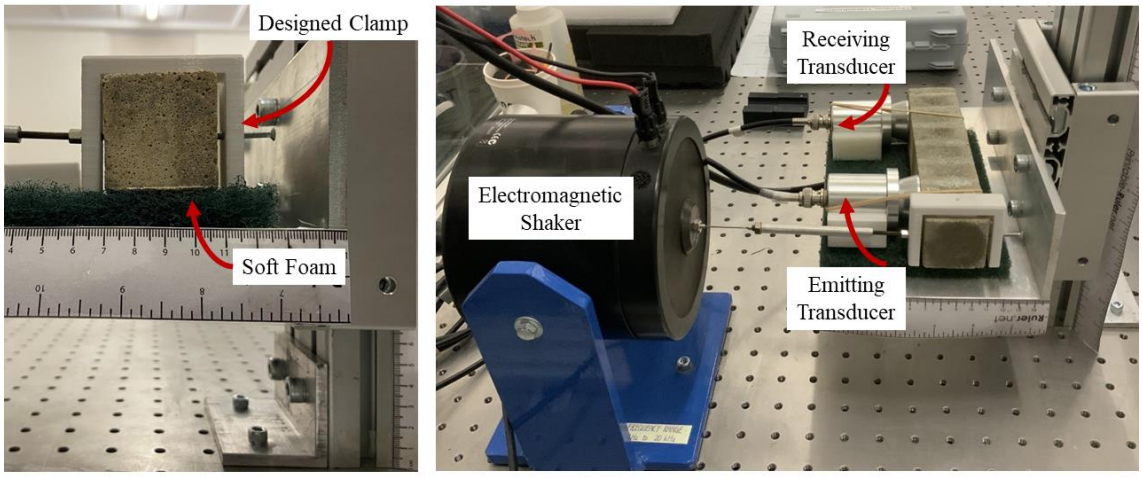

(a) (b)

Fig.5-2 (a) Designed clamp made by 3D printer, (b) Experimental set-up of AMVA technique

3.4.2 Data analysis

Emitting and receiving signal

The continuous amplitude-modulated pump wave was pre-mixed according to Eq.(5-4), and its time domain signal is shown in Fig.5-3(a). The time domain pump wave was transferred into the spectrum by short-time Fourier transform as presented in Fig.5-3(b). After adjusting the length of the window and number of overlapped samples, the shape of the signal on time axis was corresponding to Fig.5-3(a). Meanwhile, it can be seen from frequency axis that there were three obvious bright lines, which correspond to f_{L2}=5.7 kHz and $f_{L2} \pm f_{L1}$=5.2 kHz, 6.2 kHz, respectively. The name of the transmitted amplitude-modulated (TAM) method indicates that f_{L2} is transmitted rather than suppressed when using this amplitude-modulated approach. It is because from Eq.(5-4), the pump wave parts are $A_{L2}\cos(\omega_{L2}\tau + \phi_{L2})[1 + A_{L1}\cos(\omega_{L1}\tau + \phi_{L1})]$, which can be transformed into $A_{L2}\cos(\omega_{L2} + \phi_{L2}) + 0.5A_{L1}A_{L2}\cos[(\omega_{L2} + \omega_{L1})\tau + (\phi_{L2} + \phi_{L1})] + 0.5A_{L1}A_{L2}\cos[(\omega_{L2} - \omega_{L1})\tau + (\phi_{L2} - \phi_{L1})]$. Therefore, there are three frequency components in the frequency axis in the spectrum.

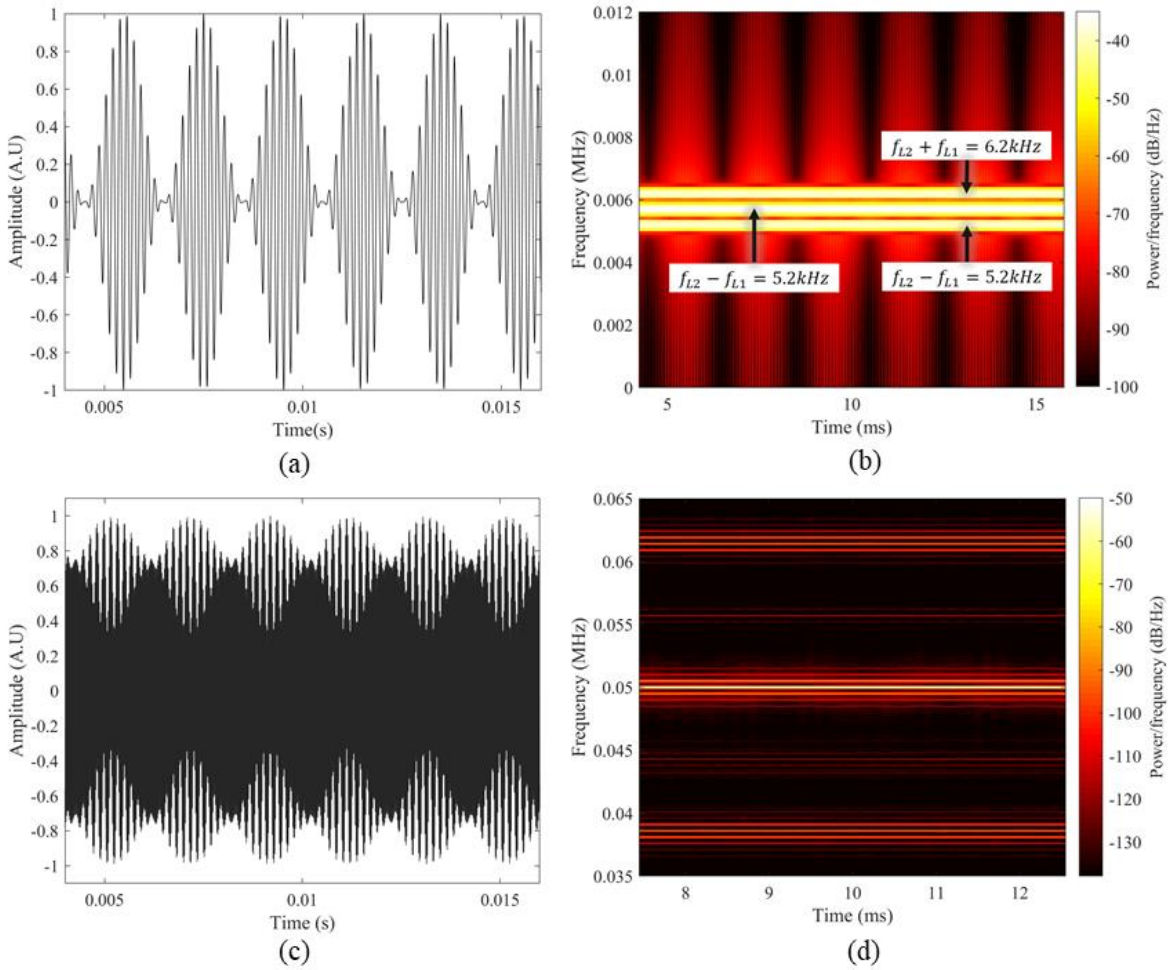

Fig.5-3 TAM method of AMVA technique: (a) time domain signal of emitting pump wave; (b) spectrum of emitting pump wave; (c) typical time domain signal of receiving signal; (d) typical spectrum of receiving signal

When monochromatic continuous probe wave $A_H\cos(\omega_H\tau+\phi_H)$ is emitted simultaneously with the amplitude-modulated continuous pump wave $A_{L2}\cos(\omega_{L2}\tau+\phi_{L2})[1+A_{L1}\cos(\omega_{L1}\tau+\phi_{L1})]$, these two waves propagated through the whole monitored specimen and the received signal is shown in Fig.5-3 (c). The received signal was analyzed using the same procedure, and its typical spectrum is displayed in Fig.5-3 (d). The frequency of probe wave is 50 kHz, and sidebands are shown as the bright bars next to 50 kHz when the monitored structures have thermal damage.

Selection of sidebands

A typical frequency domain signal with sidebands is shown in Fig.5-4. In this study, it is found that in the intact specimens, some sidebands still appear in the frequency domain. It is because PRG mortar is a cement-based composite material that always has inherent defects even before heating treatment, which induce some sidebands with small magnitudes. Therefore, it is better to select sidebands that i) occur steadily from intact state to higher damaged levels and ii) are apparent and not masked by the other sideband components.

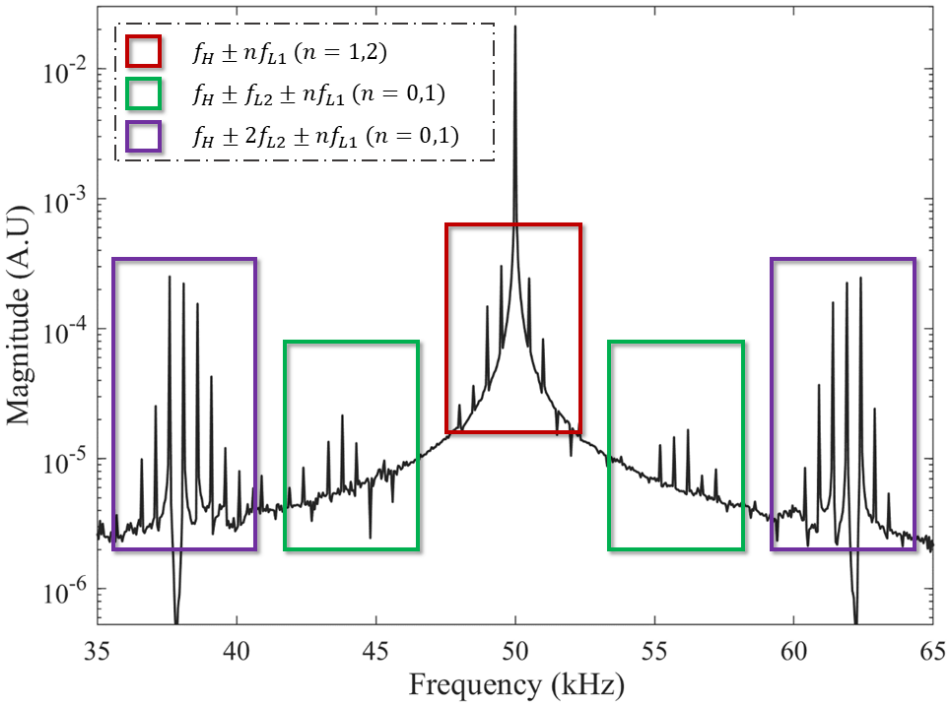

Fig.5-4 Typical frequency domain with different order sidebands

The sidebands selected for calculating the nonlinear parameter are shown in Fig.4, and the details are presented in Table 5-4. It could be found that all the frequencies of sideband components correspond to Eq.(5-5), but the sidebands at $f_H \pm 2f_{L2} \pm 2f_{L1}$ sometimes were weak to be considered. Hence, only sideband components listed in Table 4 were used to calculate the nonlinear parameter β in this study. However, the

higher-order sidebands at $f_H \pm 2f_{L2} \pm 2f_{L1}$ and $2f_H \pm nf_{L2} \pm nf_{L1}$ ($n = 1,2$) are quite sensitive when the specimen exposure to high temperatures, which show a great number of sidebands with sharply increasing magnitudes. Therefore, the higher-order sidebands as a potential tool for damage assessment are deserved further study.

Table 5-4 The frequencies of sidebands for calculating the nonlinear parameter $\beta^{(2+3)}$

Frame	Order	Frequencies of sidebands	Detailed frequencies (kHz)
Red frame in Fig.4 $f_H \pm nf_{L1}$	$n = 1$	$f_H + f_{L1}$	50.5
		$f_H - f_{L1}$	49.5
	$n = 2$	$f_H + 2f_{L1}$	51.0
		$f_H - 2f_{L1}$	49.0
Green frame in Fig.4 $f_H \pm f_{L2} \pm nf_{L1}$	$n = 0$	$f_H + f_{L2}$	55.7
		$f_H - f_{L2}$	44.3
	$n = 1$	$f_H + f_{L2} + f_{L1}$	56.2
		$f_H + f_{L2} - f_{L1}$	55.2
		$f_H - f_{L2} + f_{L1}$	44.8
		$f_H - f_{L2} - f_{L1}$	43.8
Purple frame in Fig.4 $f_H \pm 2f_{L2} \pm nf_{L1}$	$n = 0$	$f_H + 2f_{L2}$	61.4
		$f_H - 2f_{L2}$	38.6
	$n = 1$	$f_H + 2f_{L2} + f_{L1}$	61.9
		$f_H + 2f_{L2} - f_{L1}$	60.9
		$f_H - 2f_{L2} + f_{L1}$	39.1
		$f_H - 2f_{L2} - f_{L1}$	38.1
	$n = 2$	$f_H + 2f_{L2} + 2f_{L1}$	62.4
		$f_H + 2f_{L2} - 2f_{L1}$	60.4
		$f_H - 2f_{L2} + 2f_{L1}$	39.6
		$f_H - 2f_{L2} - 2f_{L1}$	37.6

Calculation of nonlinear parameter β

According to the relationship between $\sum A_S$ and $A_H A_{L2}$ in Eq.(5-6), the nonlinear parameter β can be defined as the slope of the linear fitting of $\sum A_S$ and $A_H A_{L2}$. As mentioned in Section 3.4.1, the voltage of the input pump wave remains the same while the voltage of the input probe wave increases steadily. Hence, a group of points ($\sum A_S$, $A_H A_{L2}$) were plotted as shown in Fig.5-5(a). The reasons to use a group of points ($\sum A_S$, $A_H A_{L2}$) is to avoid the effect of system nonlinearity and to ensure adequate input energy to induce the nonlinear distortion, such as second harmonics or sidebands. Firstly, if there is an intercept on the y-axis, as presented in

Fig.5-5(b), it indicates that when input signals are zero, the distortion of nonlinearity already exists. Therefore, the nonlinearity comes from the measurement system. Using the trendline of data points in Fig.5-5(a) ($\sum A_S$, $A_H A_{L2}$) can efficiently remove the adverse effect of instrumental nonlinearity. Additionally, when supposing the intercept shown on the x-axis as displayed in Fig.5-5(c), it implies that enough input energy is able to induce the nonlinear phenomena. In this study, most of the experimental data can be described by the situation shown in Fig.5-5(c), which demonstrates one of the merits of the vibro-acoustic technique is that system nonlinearity has only little influence on the measurements.

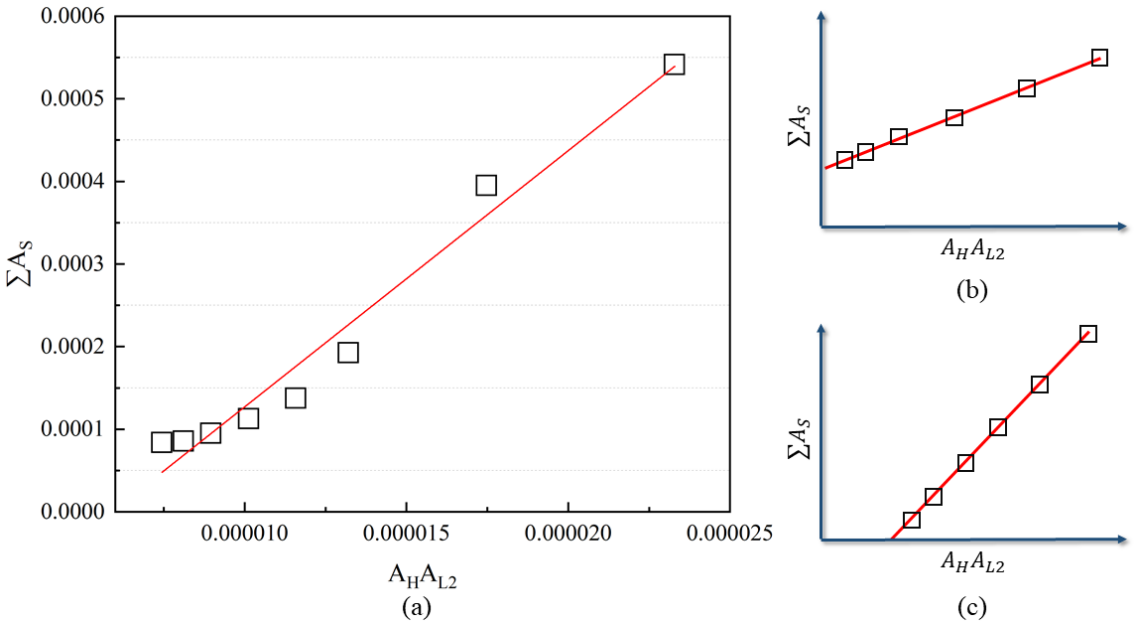

Fig.5-5 (a) Linear fitting of $A_H A_{L2}$ and $\sum A_S$ for calculation of nonlinear parameter β in experiment, (b) nonlinearity from system, (c) adequate input energy to induce nonlinear distortion

4. Results and discussion

4.1 Photos of specimens before and after high-temperature treatments

The typical photos of specimens of Mix1 and Mix2 before and after high-temperature treatments were presented in Fig.5-6 and Fig.5-7, respectively. The scale of each photo was shown as a blue line in the right-hand corner, which was 40μm. Furthermore, the cracks were marked in red circles. It can be seen that damages of high-temperature were usually distributed

cracks, in which the width was in the range of 2-10 μm. The temperature of the heat treatments became higher, and the distribution density of cracks was greater.

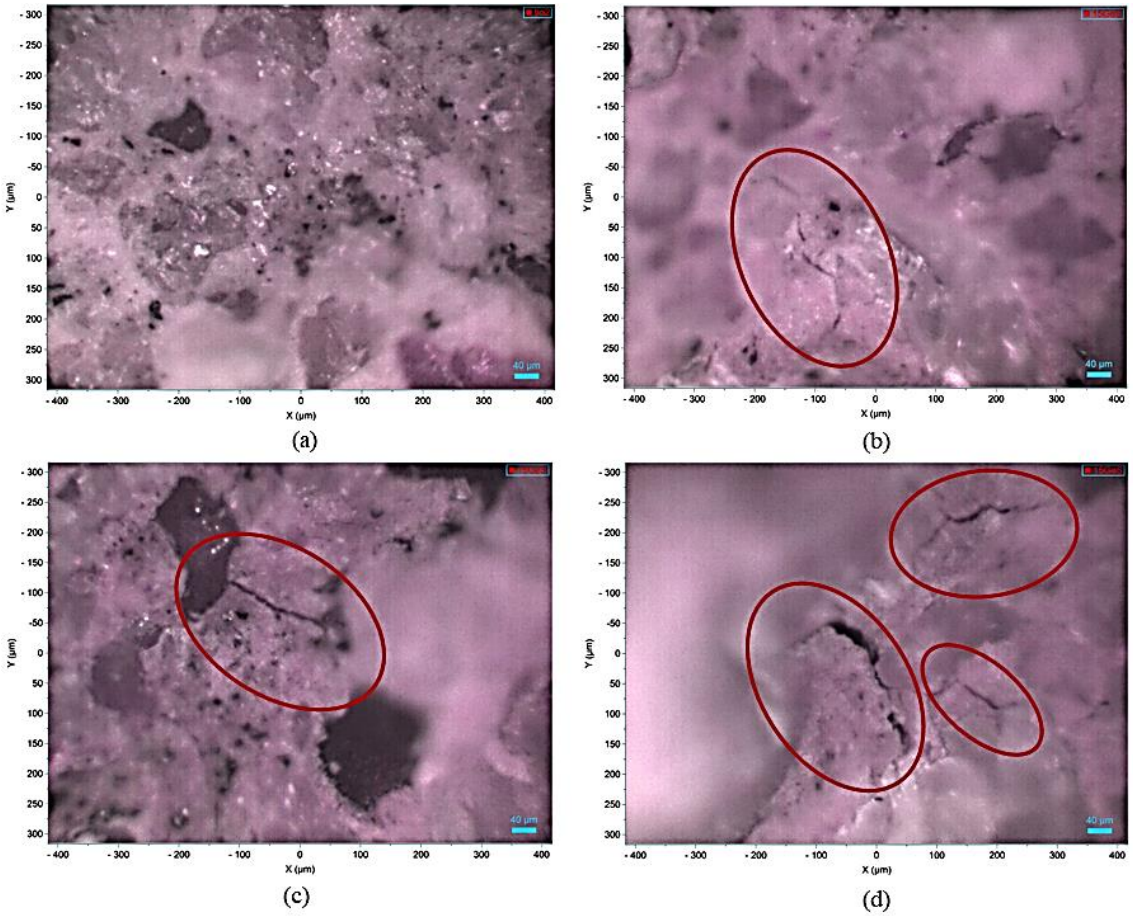

Fig.5-6 Photos of Mix1 of (a) intact state, (b) 100℃, (c) 250℃, (d) 360℃

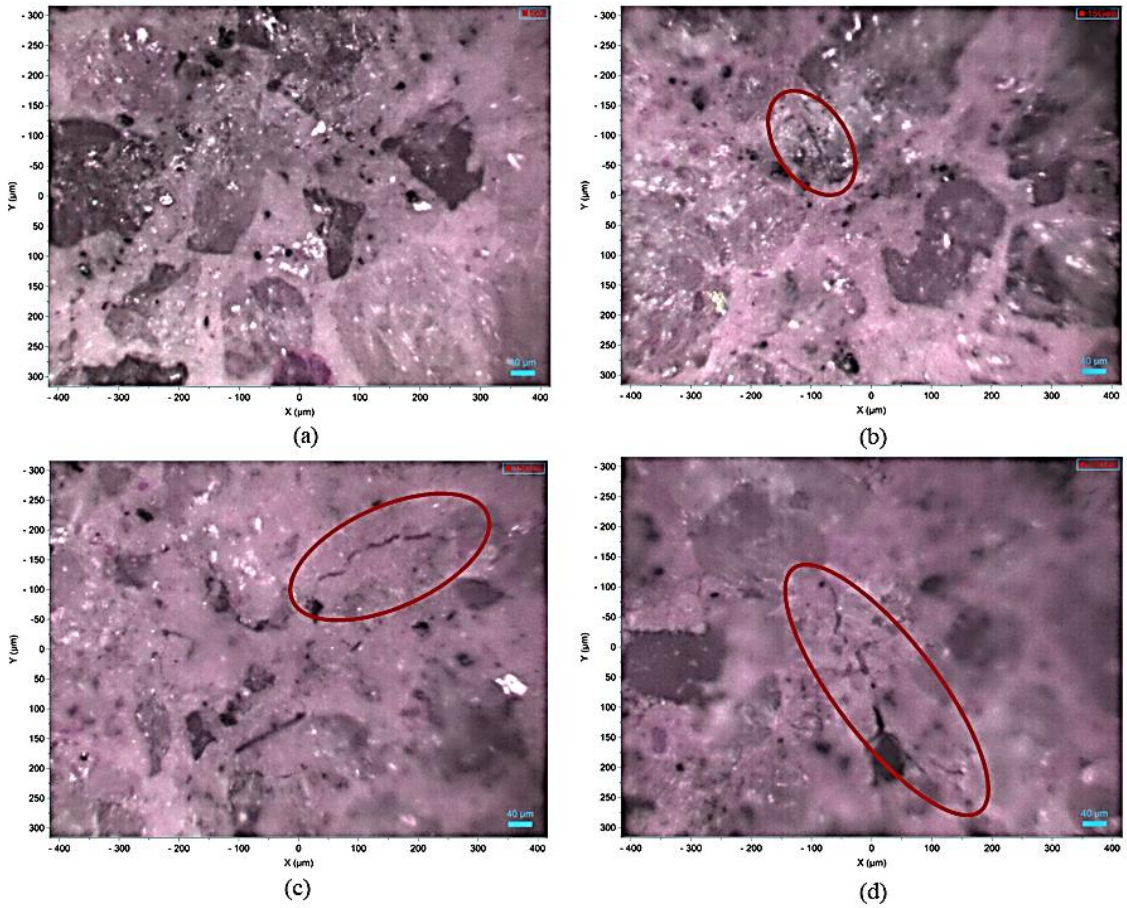

Fig.5-7 Photos of Mix2 of (a) intact state, (b) 100℃, (c) 250℃, (d) 360℃

4.2 Results of dynamic elastic modulus E_d

According to the experiments discussed in Section 3.2, M1S1 and M2S1 were heated to 100℃. The target heating temperature of M1S2 and M2S2 was 250℃, and the final batch of M1S3 and M2S3 were heated to 360℃. As stated in ASTM C215-19 [43], the mass of the monitored structure was used for calculation of dynamic elastic modulus E_d. Therefore, the masses of these PRG mortar specimens were measured before and after heat treatments. The results are shown in Fig.5-6. It can be found that after being heated to 100℃, the mass loss ratio of M1S1 and M2S1 was 2.37% and 2.12%, respectively. The mass losses of this batch of PRG mortar specimens were around 2%, which are attributed to water evaporation and loss of part of physically bound water in the PRG mortar material [7]. When the PRG mortar specimens were heated to 250℃, the mass loss ratio of M1S2 and M2S2 was 5.92% and 5.64%, respectively.

Meanwhile, at the target temperature 360℃, the mass loss ratio of M1S3 and M2S3 was 6.70%, and 5.70%, respectively. In the range of 250−360℃, the mass loss ratios were all around 6%, which are related to the loss of chemically bound water as well as the dehydration products.

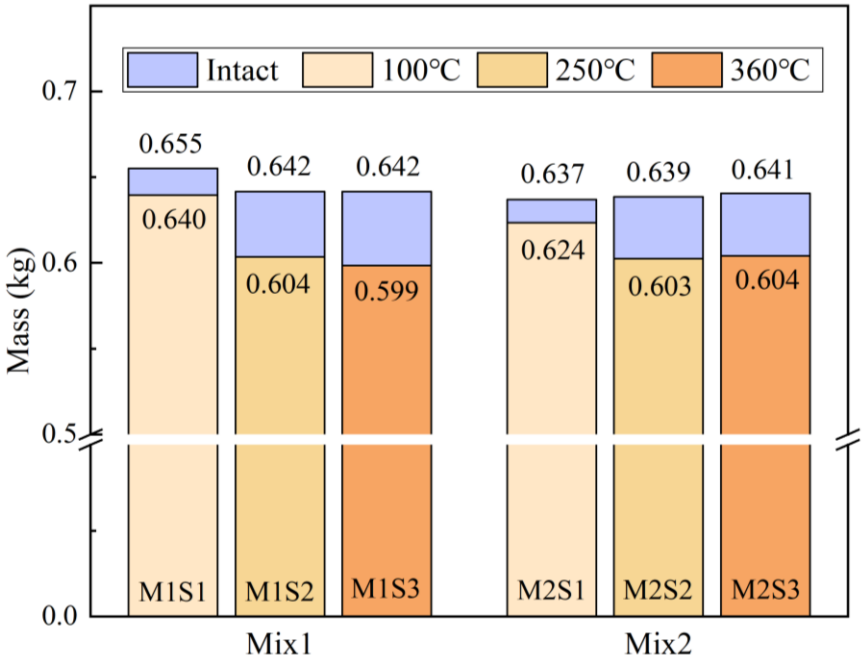

Fig.5-8 The mass of PRG specimens in the intact state and after high-temperature exposure

After measuring the mass of each PRG specimen, the experiments following ASTM C215-19 [49] were conducted before heating treatment. The results are presented in Fig.5-9. The tests were conducted ten times for each specimen, and its value and error bar are shown in Fig.5-9. In addition, the average E_d of each mix of PRG specimen was displayed in red. Along with the increase of PRG size from Mix1 to Mix2, the average E_d was also increased. It was because most of the mechanical adhesion forces generated by friction between surfaces of PRGs and cement gels have stronger connection due to larger surface areas of PRGs [11]. Furthermore, large PRGs can reinforce cement composite by reducing the distances between cement particles in cement gels through the van der Waals forces [50]. Therefore, E_d which is an index indicates the mechanical properties of materials, increases with the size of PRG.

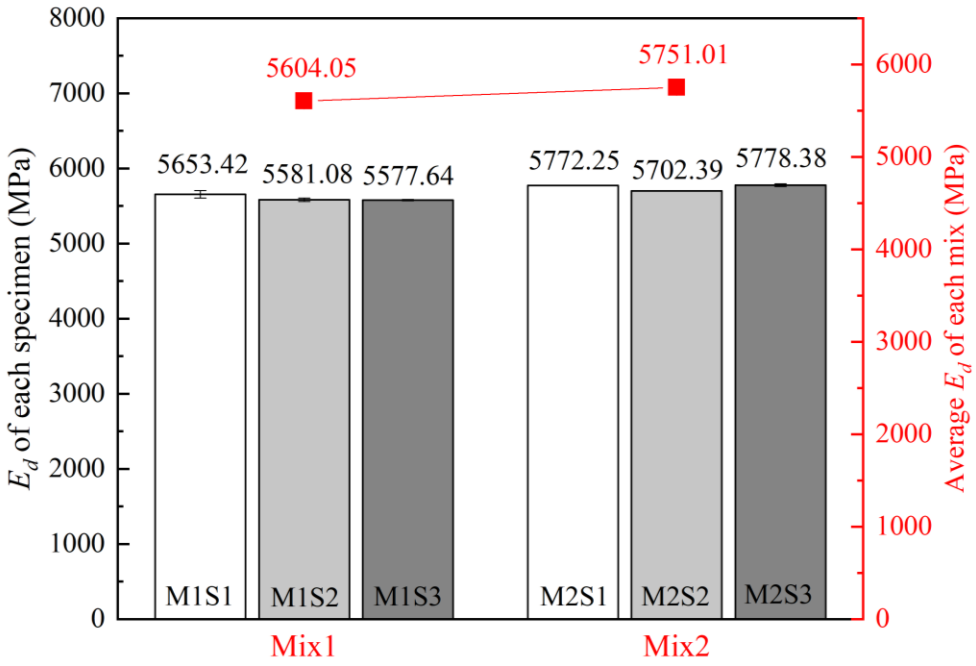

Fig.5-9 E_d of PRG mortar specimens in the intact state

After the thermal treatments, the resonant frequency tests were conducted to obtain E_d of PRG mortar specimens exposure to high temperatures as shown in Fig.5-10. The batch of PRG mortar specimens heated to 100℃ was M1S1 and M2S1. The changing ratio from intact state to 100℃ of M1S1 and M2S1 was 18.67% and 21.63%, respectively. As mentioned above, the change of E_d was majorly caused by the loss of reversible water content in the PRG mortar materials. In addition, the water content significantly affects the mass of monitored structures, and hence, it has a critical influence on E_d. However, it should be noted that the decrease of E_d for specimen exposure to 100℃ was not caused by permanent structural changes (e.g., cracks or defects) but by mass loss due to evaporation of free water. Thus, the result E_d obtained from the resonant frequency test is not steady and highly depends on the testing conditions, such as moisture content, which restrict its practical application.

Similarly, the changing ratio from intact state to 250℃ of the next batch specimens including M1S2, and M2S2, was 32.40% and 27.29%, respectively. Furthermore, the changing

ratio 35.38% and 31.52% corresponded to M1S3 and M2S3, which were exposed to 360℃. As illustrated in Fig.5-10, E_d of Mix2 after the heating treatments were generally larger than Mix2. It is in good agreement with the conclusion that larger size PRGs with larger surface areas are beneficial to mechanical properties as well as microstructural patterns. Consequently, E_d of resonant frequency technique is able to distinguish the different dosages of PRG mortars. Nevertheless, the decreasing trend between 250℃ to 360℃ is not as sharp as the trend between ambient temperature to 100 ℃. However, the irreversible changes occurred after 100 ℃, including loss of physically bonded water from the decomposition of the C-S-H and the vanish of hydration products, which are the main factors leading to real structural damage or failure. Hence, the results E_d of resonant frequency test is not that sensitive to irreversible damages or degradation but they are seriously affected by the reversible water content of material based on the experimental results in this study.

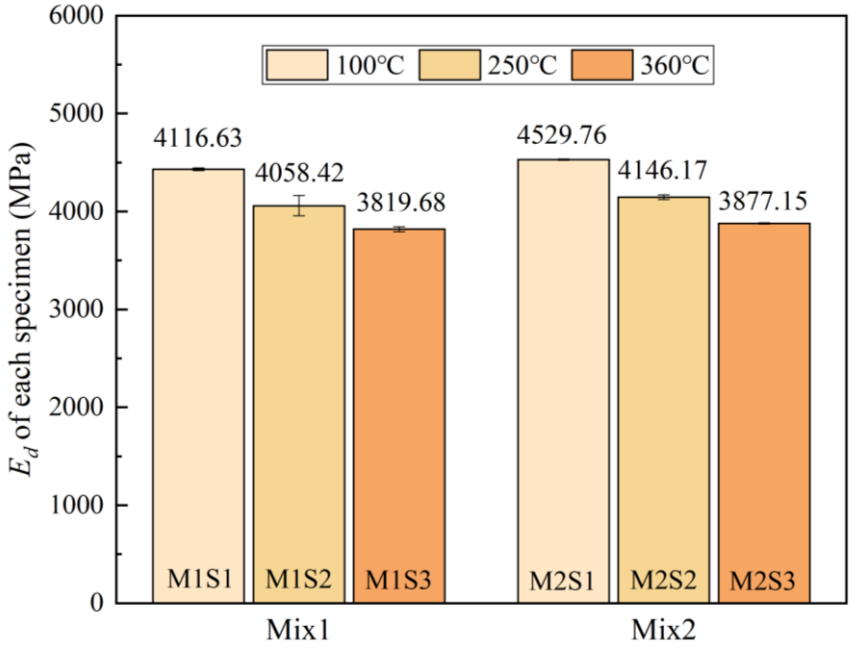

Fig.5-10 E_d of PRG mortar specimens after exposure to high-temperature

4.3 Results of nonlinear parameter $\beta^{(2)}$ and $\beta^{(2+3)}$

The data obtained from the experiment of AMVA technique are analyzed following data analysis approach in Section 3.4.2, in which the data were transformed into the frequency domain through the fast Fourier transform (FFT) as shown in Fig.5-11. It is interesting that PRG mortar specimen at the intact state has inherent defects and cracks that cause distortion in the signal. So there are some tiny sidebands showing in the frequency domain at the intact state as displayed in Fig.5-11 (a). Hence, it is obvious that the nonlinear parameter $\beta^{(2)}$ and $\beta^{(2+3)}$ at the intact state is not zero for the inherent defects and cracks. When the PRG mortar specimens were heated to the elevated temperature from 100℃ to 360℃, the amplitudes and numbers of sidebands were both increased. The typical frequency domain at 100℃, 250℃, and 360℃ is presented in Fig.5-11 (b), (c), and (d), respectively.

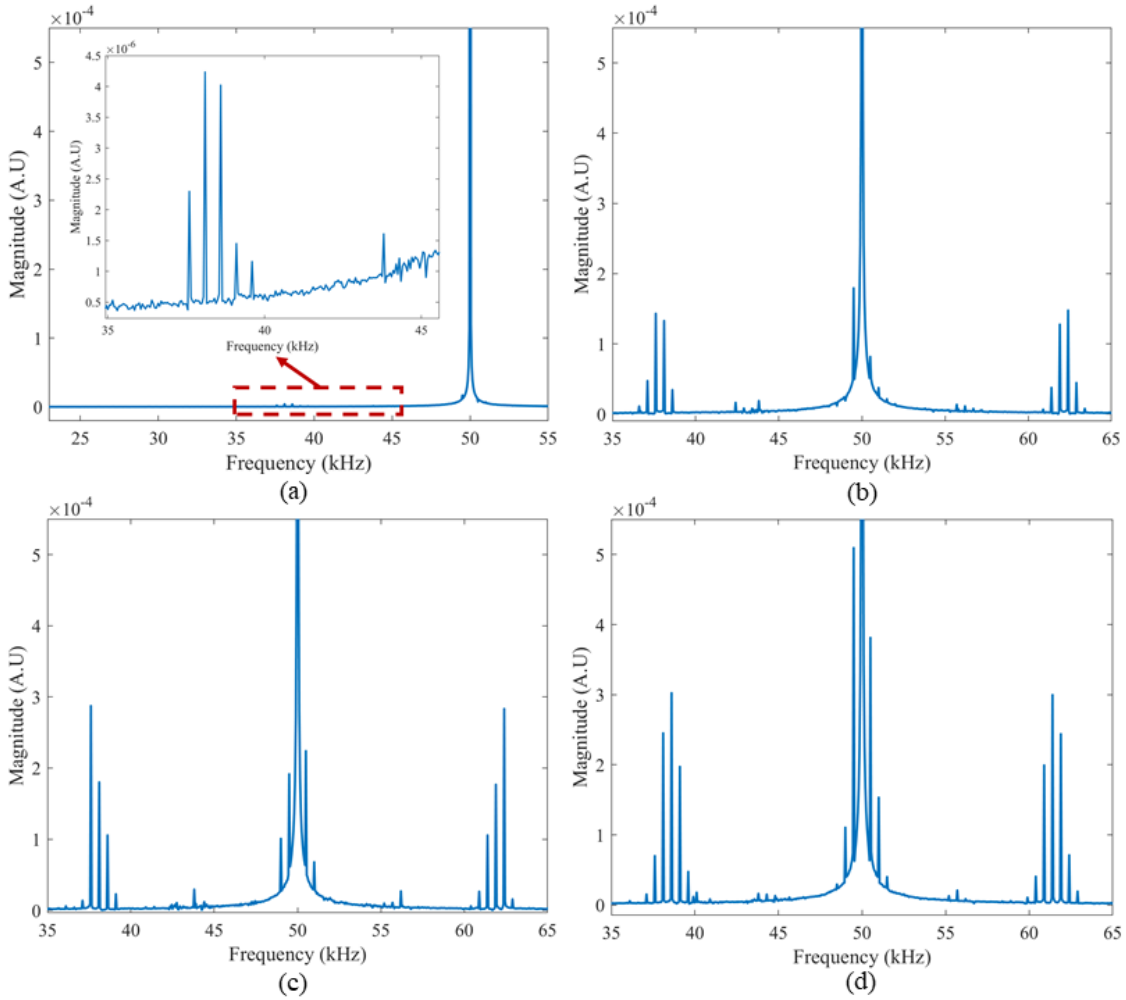

Fig.5-11 Frequency domain of Mix2: (a) intact state, (b) 100 ℃, (c) 250 ℃, (d) 360 ℃

The nonlinear parameter $\beta^{(2+3)}$ of all PRG mortar specimens in the intact state were shown in Fig.5-12. The particle size of pristine graphene of Mix1 was 43μm, while it was 73 μm of Mix2. According to the previous research [11], the mortar with larger pristine graphene has better behavior on both compressive and tensile strengths, which is attributed to the better microstructural patterns of the cement-based material. It was because the cement hydration process is enhanced due to the reduction of distances between cement particles in cement gels caused by van der Waals forces between PRGs. Therefore, the average $\beta^{(2+3)}$ of Mix2 is 27.70, which is smaller than Mix1 of 24.87. It means that the specimens of Mix2 have fewer inherent defects and microcracks. The results are in accordance with the measurement E_d in Section 4.2.

The error bar of average $\beta^{(2+3)}$ only indicates whether the manufacturing quality of the batch of specimens is consistent. It does not represent the accuracy of the measurements in AMVA experiments.

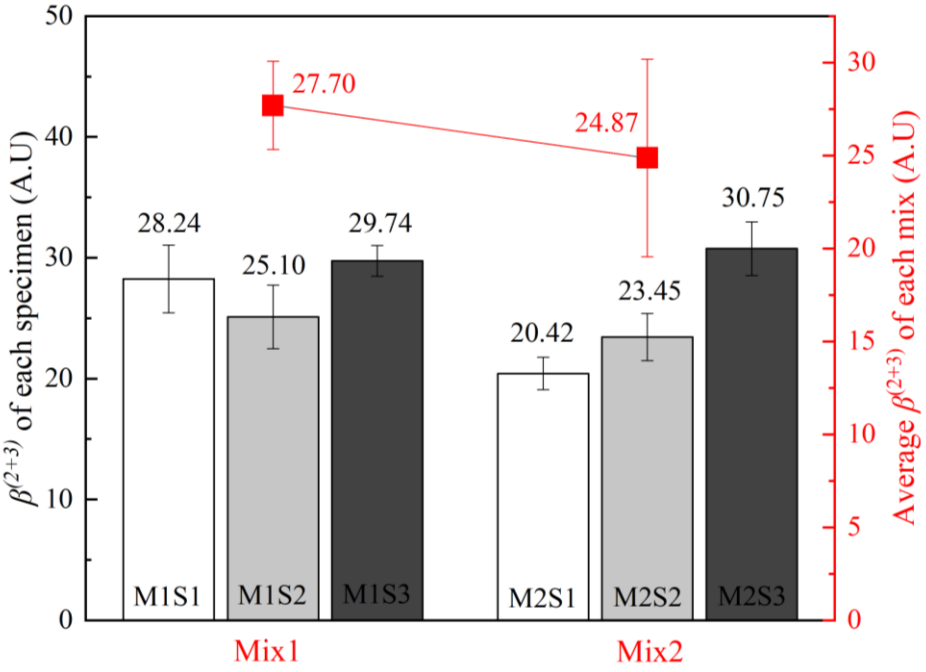

Fig.5-12 $\beta^{(2+3)}$ of PRG mortar specimens in the intact state

When the PRG mortar specimens were heated to the target temperature, all the specimens were tested through the AMVA technique, and the results are shown in Fig.5-13. Generally, $\beta^{(2+3)}$ of Mix2 after heating to 100℃, 250℃, and 360℃ are smaller than those of Mix1. It is because PRGs with larger sizes have larger friction adhesion forces due to their larger surface areas connecting with cement gels (*e.g.*, $43 \times 43 = 1849\mu m^2$, and $73 \times 73 = 5329\mu m^2$). When the PRG cement-based material suffered from high temperatures, the stronger friction afforded by the larger-size PRGs could help prevent the generation and development of microcracks due to inconsistent expansions of different materials exposed to high temperatures. It should be noted that there is a sharp increase of $\beta^{(2+3)}$ for the specimens heated to 250℃ and 360℃. The changing ratio of M1S2 at 250℃ is 112.84% while M2S2 is

92.89%. Furthermore, the changing ratio of M1S3 and M2S3 exposure to 360℃ is 171.86% and 151.85%, respectively. The reason is discussed in Section 4.2 that when the PRG mortar specimens were heated to 100℃, most of the changes could be attributed to the evaporation of water that was reversible. But there is only tiny irreversible structural changes caused by the loss of part of physically bound water in the PRG mortar. Therefore, $\beta^{(2+3)}$ of both M1S1 and M2S1 heated to 100℃ do not show a noticeable change for the specimens heated to 250℃ and 360℃. There was a significant change in the $\beta^{(2+3)}$ of M1S2 and M2S2 at 250℃, which can be explained by the loss of chemically bound water and dehydration products. Hence, some microcracks were generated, and inherent defects developed at this state. Another sharper increment of $\beta^{(2+3)}$ was observed at 360℃ due to the continuing bound water loss and dehydration products, which led to the contraction of the cement matrix and produced more considerable interface distance and more damage. It demonstrated that the AMVA technique was enabled to distinguish the actual microstructural changes instead of being affected by the testing condition.

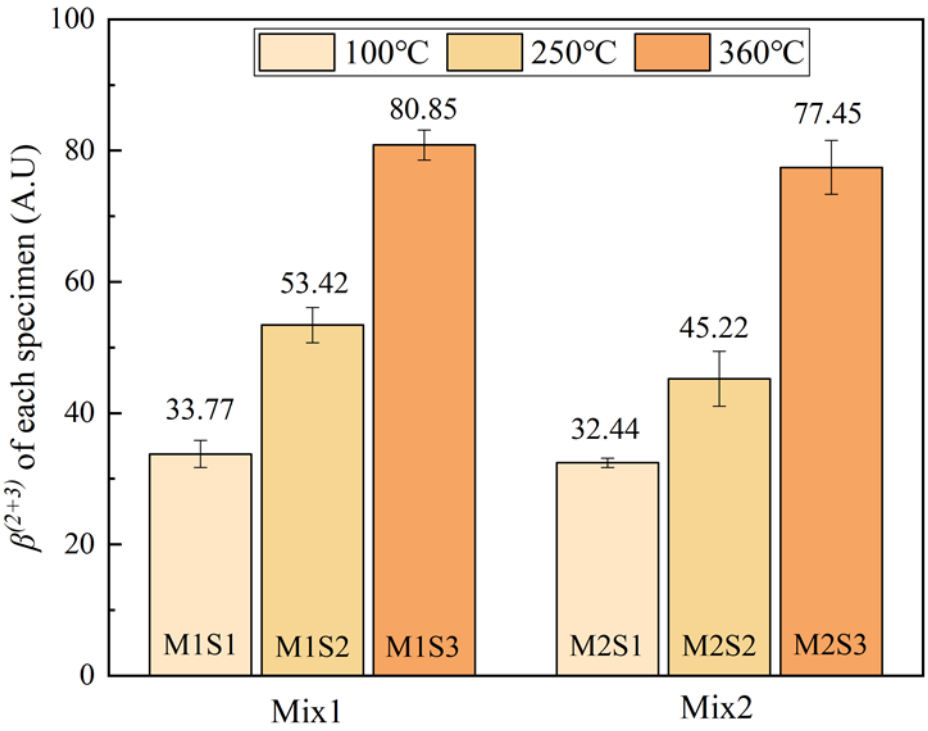

Fig.5-13 $\beta^{(2+3)}$ of PRG mortar specimens after exposure to high-temperature

The results of $\beta^{(2)}$ of PRG mortar specimens in the intact state and after exposure to high temperatures were presented in Fig.14. Comparing to $\beta^{(2+3)}$, it was found that the values of $\beta^{(2)}$ were all smaller than $\beta^{(2+3)}$ because the parts of $A_H A_{L2}$ are the same but $\sum A_s$ of $\beta^{(2)}$ were smaller than $\sum A_s$ of $\beta^{(2+3)}$. It should be noted that each $\beta^{(2)}$ of Mix1 and Mix2 were not consistent with $\beta^{(2+3)}$ in intact state, but the average $\beta^{(2)}$ of each mix of PRG, as marked in red in Fig.5-14(a), had the same tendency as $\beta^{(2+3)}$ that the average nonlinear parameter of Mix1 was larger than Mix2. This result also indicated that the specimens of Mix1 had more inherent defects compared to the specimens of Mix2, which was also in agreement with the results of E_d. The inconsistency of $\beta^{(2)}$ might be caused by the following reason: i) the sidebands in intact state were small, and little changes would cause significant differences of $\beta^{(2)}$, ii) the energy distributed to various extra frequencies due to material nonlinearity, and energy that shifted to $\omega_H \pm \omega_{L2}$ and $\omega_H \pm \omega_{L2} \pm \omega_{L1}$ cannot present whole nonlinear distortion according to the experimental results in this study. After exposure to high temperatures, it was interesting to find that that $\beta^{(2)}$ of M1S1 after heated to 100℃ was smaller than $\beta^{(2)}$ of intact state. It might be because when there was critical damage in the medium, it would be a considerable energy shift from fundamental frequency components to higher order harmonics and sidebands, and these distortions can be used to characterize the damage in the medium distributed to a certain range of frequency. When only a small range of frequency was considered, the energy distributed in this area can describe the damages but is not that reliable and robust, particularly in the early damage state. However, $\beta^{(2)}$ and $\beta^{(2+3)}$ had the same tendency that β increased when the temperature became higher. Therefore, when compared with $\beta^{(2)}$, $\beta^{(2+3)}$ that containing a wide range of sidebands was more reliable and feasible to

assess damages due to material nonlinearity. Hence, $\beta^{(2)}$ was not considered for the following dimensionless index transformation for sensitivity comparison.

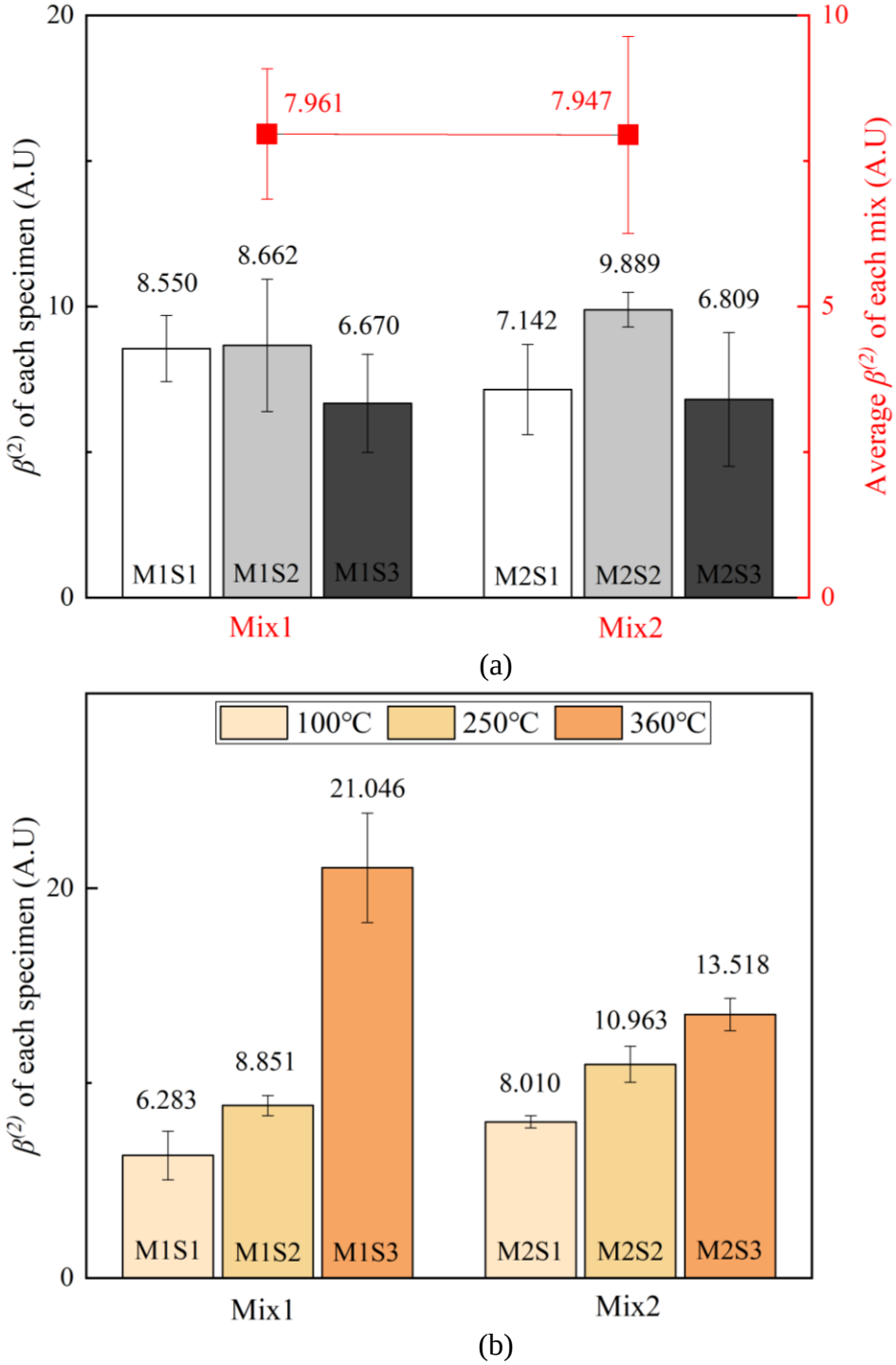

Fig.5-14 $\beta^{(2)}$ of PRG mortar specimens: (a) intact state, (b) after exposure to high-temperature

4.4 Comparison of E_d and $\beta^{(2+3)}$

In Sections 4.2 and 4.3, it was found that when the temperature was elevated, the tendency of E_d was decreased but $\beta^{(2+3)}$ was increased. For a better comparison of the conventional resonant frequency technique and the proposed AMVA technique, both E_d and $\beta^{(2+3)}$ were transformed into a dimensional index following Eq.(5-7),

$$\gamma = (E_d^0 - E_d')/E_d^0 \text{ or } \gamma = (\beta' - \beta^0)/\beta^0 \quad (5\text{-}7)$$

where γ is the dimensionless index, E_d^0 is the E_d at intact state, E_d' is the E_d exposure to high temperature, while β^0 is the β at intact state and β' is the β after heating treatments.

Both E_d and $\beta^{(2+3)}$ of Mix1 and Mix2 under 25℃, 100℃, 250℃ and 360℃ were transferred into γ, which were displayed together in Fig.15. It can be seen that γ of E_d increased gradually from ambient temperature to 360℃, while γ of $\beta^{(2+3)}$ had sharp increases during the different high-temperature levels. Particularly at 360℃, γ of $\beta^{(2+3)}$ were 500% larger than γ of E_d. It demonstrated the nonlinear parameter $\beta^{(2+3)}$ was much more sensitive to thermal damage in cement-based materials when compared to E_d. Furthermore, it was obvious that two curves of γ of E_d, including Mix1 and Mix2, were quite closed. Therefore, it was difficult to distinguish the difference between the PRG mortar specimens with various dosages through the conventional resonant frequency test, particularly when the moisture content of materials changed frequently. At the state heating to 100℃, it was interesting to find that γ of $\beta^{(2+3)}$ of Mix1 was smaller than Mix2. It was because the change in this state could be attributed to the loss of evaporable water, but there were also some parts of microstructural changes due to physically bound water loss. It might be the reason that γ of $\beta^{(2+3)}$ of Mix2 at 100℃ was larger than the other index. At the state of 250℃ and 360℃, γ of $\beta^{(2+3)}$ of Mix2 were all larger than γ of $\beta^{(2+3)}$ of Mix2, which is in good agreement with the conclusion that

specimens of Mix2 with larger PRG particle size had better material structures to be resistant to high-temperature treatments.

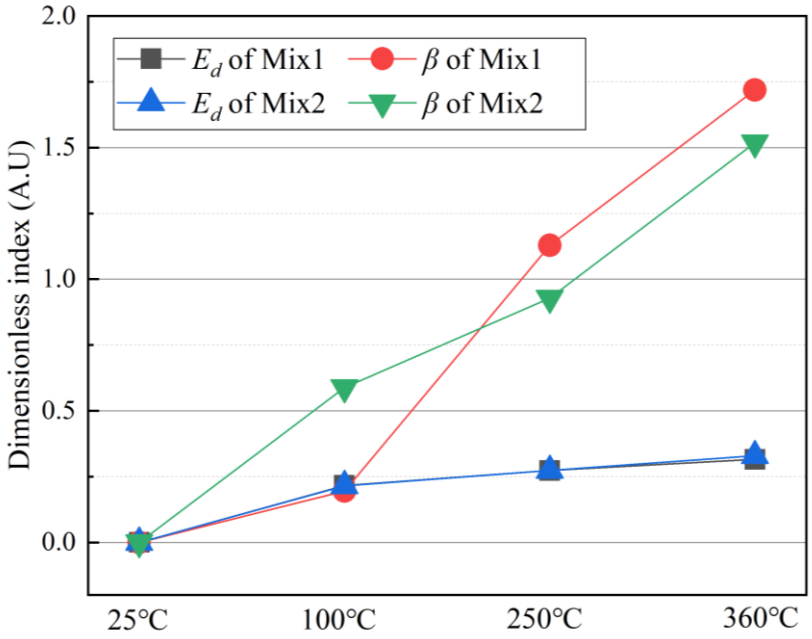

Fig.5-15 Comparison of damage indexes

5. Conclusion

In this paper, a higher-order effect of AMVA technique has been proposed and investigated. A theoretical model containing higher-order effects has been established in order to obtain the nonlinear parameter $\beta^{(2+3)}$ to describe the thermal damages as well as distinguish the different dosages of cement-based materials. Furthermore, experiments of both conventional resonant frequency technique and AMVA technique have been conducted on PRG mortar specimens with different dosages under different high-temperature levels. The main conclusions have been drawn as follows.

(i) The theoretical model containing higher-order effects can utilize multi-order sidebands, which have abundant information of material nonlinearity that can be used for damage detection.

(ii) The proposed AMVA technique is different too the conventional vibro-acoustic technique using single-frequency pump wave and probe wave. In the AMVA technique, a transmitted amplitude-modulated pump wave was introduced for the purpose of lower power consumption and versatility.

(iii) The experimental results reveal that β of the AMVA technique is sensitive to characterize different levels of thermal damage as well as to distinguish PRG mortar materials with various dosages when compared with E_d from the conventional resonant frequency technique. Particularly when thermal treatment achieved 360 ℃, the dimensionless index of β is 500% higher than E_d.

Acknowledgements

Ms Tingyuan Yin's PhD scholarship is supported by China Scholarship Council. The support is greatly appreciated. The authors also would like to thank technicians Jon Ayoub and Michael Teague, and Dr. Xin Xu for their help with experimental work.

References

1. Chen, X.-t., et al., *Coupled transport and poro-mechanical properties of a heat-treated mortar under confinement.* Cement and Concrete Research, 2013. **49**: p. 10-20.
2. Memon, S.A., et al., *Durability of sustainable concrete subjected to elevated temperature–A review.* Construction and Building Materials, 2019. **199**: p. 435-455.
3. Xue, S., et al., *Influences of thermal damage on water transport in heat-treated cement mortar: Experimental and theoretical analyses.* Construction and Building Materials, 2021. **288**: p. 123100.

4. Jing, G., et al., *Introducing reduced graphene oxide to enhance the thermal properties of cement composites.* Cement and Concrete Composites, 2020. **109**: p. 103559.
5. Chen, Y., et al., *High-temperature properties of cement paste with graphene oxide agglomerates.* Construction and Building Materials, 2022. **320**: p. 126286.
6. Sharifianjazi, F., et al., *Fibre-Reinforced Polymer Reinforced Concrete Members under Elevated Temperatures: A Review on Structural Performance.* Polymers, 2022. **14**(3): p. 472.
7. Chu, H.-y., et al., *Effects of graphene sulfonate nanosheets on mechanical and thermal properties of sacrificial concrete during high temperature exposure.* Cement and Concrete Composites, 2017. **82**: p. 252-264.
8. Moreno-Navarro, F., et al., *Mechanical and thermal properties of graphene modified asphalt binders.* Construction and Building materials, 2018. **180**: p. 265-274.
9. Li, G. and L. Zhang, *Microstructure and phase transformation of graphene-cement composites under high temperature.* Composites Part B: Engineering, 2019. **166**: p. 86-94.
10. Lin, Y. and H. Du, *Graphene reinforced cement composites: A review.* Construction and Building Materials, 2020. **265**: p. 120312.
11. Ho, V.D., et al., *Influence of pristine graphene particle sizes on physicochemical, microstructural and mechanical properties of Portland cement mortars.* Construction and Building Materials, 2020. **264**: p. 120188.
12. Ho, V.D., et al., *Enhancing the performance and environmental impact of alkali-activated binder-based composites containing graphene oxide and industrial by-products.* Construction and Building Materials, 2021. **284**: p. 122811.

13. Chen, J., et al., *Characterization of thermal damage in sandstone using the second harmonic generation of standing waves.* International Journal of Rock Mechanics and Mining Sciences, 2017. **91**: p. 81-89.

14. Kim, B.-C., J. Chen, and J.-Y. Kim, *Relation between crack density and acoustic nonlinearity in thermally damaged sandstone.* International Journal of Rock Mechanics and Mining Sciences, 2020. **125**: p. 104171.

15. Kim, J.-Y., et al., *Use of combined linear and nonlinear ultrasound to examine microstructural and microchemical variations in highly irradiated 304 stainless steel.* Journal of Nuclear Materials, 2021. **545**: p. 152644.

16. Aseem, A. and C.T. Ng, *Debonding detection in rebar-reinforced concrete structures using second harmonic generation of longitudinal guided wave.* NDT & E International, 2021. **122**: p. 102496.

17. Vidler, J., A. Kotousov, and C.-T. Ng, *Effect of randomly distributed voids on effective linear and nonlinear elastic properties of isotropic materials.* International Journal of Solids and Structures, 2021. **216**: p. 83-93.

18. Vidler, J., A. Kotousov, and C.-T. Ng, *Effective elastic properties of a weakly nonlinear particulate composite.* International Journal of Non-Linear Mechanics, 2022: p. 103949.

19. Eiras, J., et al., *Nondestructive monitoring of ageing of alkali resistant glass fiber reinforced cement (GRC).* Journal of Nondestructive Evaluation, 2013. **32**(3): p. 300-314.

20. Van Den Abeele, K.-A., P.A. Johnson, and A. Sutin, *Nonlinear elastic wave spectroscopy (NEWS) techniques to discern material damage, part I: nonlinear wave modulation spectroscopy (NWMS).* Journal of Research in Nondestructive Evaluation, 2000. **12**(1): p. 17-30.

21. Van Den Abeele, K.-A., et al., *Nonlinear elastic wave spectroscopy (NEWS) techniques to discern material damage, Part II: Single-mode nonlinear resonance acoustic spectroscopy.* Journal of Research in Nondestructive Evaluation, 2000. **12**(1): p. 31-42.

22. Zhang, Z., et al., *Contact acoustic nonlinearity (CAN)-based continuous monitoring of bolt loosening: Hybrid use of high-order harmonics and spectral sidebands.* Mechanical Systems and Signal Processing, 2018. **103**: p. 280-294.

23. Kundu, T., et al., *Fundamentals of nonlinear acoustical techniques and sideband peak count*, in *Nonlinear Ultrasonic and Vibro-Acoustical Techniques for Nondestructive Evaluation*. 2019, Springer. p. 1-88.

24. Donskoy, D.M. and A.M. Sutin, *Vibro-acoustic modulation nondestructive evaluation technique.* Journal of intelligent material systems and structures, 1998. **9**(9): p. 765-771.

25. Solodov, I., et al., *Nonlinear self-modulation and subharmonic acoustic spectroscopyfor damage detection and location.* Applied physics letters, 2004. **84**(26): p. 5386-5388.

26. Zaitsev, V., et al., *Novel nonlinear-modulation acoustic technique for crack detection.* Ndt & e international, 2006. **39**(3): p. 184-194.

27. Aymerich, F. and W. Staszewski, *Experimental study of impact-damage detection in composite laminates using a cross-modulation vibro-acoustic technique.* Structural Health Monitoring, 2010. **9**(6): p. 541-553.

28. Trojniar, T., et al. *Fatigue crack detection using nonlinear vibro-acoustic cross-modulations based on the Luxemburg-Gorky effect*. in *Health Monitoring of Structural and Biological Systems 2014*. 2014. SPIE.

29. Kim, S., et al., *Crack detection technique for operating wind turbine blades using Vibro-Acoustic Modulation.* Structural Health Monitoring, 2014. **13**(6): p. 660-670.

30. Liu, P., H. Sohn, and I. Jeon, *Nonlinear spectral correlation for fatigue crack detection under noisy environments.* Journal of Sound and Vibration, 2017. **400**: p. 305-316.

31. Liu, B., Z. Luo, and T. Gang, *Influence of low-frequency parameter changes on nonlinear vibro-acoustic wave modulations used for crack detection.* Structural Health Monitoring, 2018. **17**(2): p. 218-226.

32. Qin, X., et al., *Full life-cycle monitoring and earlier warning for bolt joint loosening using modified vibro-acoustic modulation.* Mechanical Systems and Signal Processing, 2022. **162**: p. 108054.

33. Czeluśniak, K., W.J. Staszewski, and F. Aymerich, *Local bispectral characteristics of nonlinear vibro-acoustic modulations for structural damage detection.* Mechanical Systems and Signal Processing, 2022. **178**: p. 109199.

34. Dorendorf, L., N. Lalkovski, and M. Rutner, *Physical explanation for vibro-acoustic modulation due to local and global nonlinearities in a structure and its experimental and numerical validation.* Journal of Sound and Vibration, 2022. **528**: p. 116885.

35. Alnuaimi, H., et al., *An improved nonlinear ultrasonic technique for detecting and monitoring impact induced damage in composite plates.* Ultrasonics, 2022. **119**: p. 106620.

36. Arumaikani, T., S. Sasmal, and T. Kundu, *Detection of initiation of corrosion induced damage in concrete structures using nonlinear ultrasonic techniques.* The Journal of the Acoustical Society of America, 2022. **151**(2): p. 1341-1352.

37. Basu, S., et al., *Nonlinear ultrasonics-based technique for monitoring damage progression in reinforced concrete structures.* Ultrasonics, 2021. **115**: p. 106472.

38. Castellano, A., et al., *Linear and nonlinear ultrasonic techniques for monitoring stress-induced damages in concrete.* Journal of Nondestructive Evaluation, Diagnostics and Prognostics of Engineering Systems, 2021. **4**(4).

39. Miele, S., et al., *Diagnosis of internal cracks in concrete using vibro-acoustic modulation and machine learning.* Structural Health Monitoring, 2022: p. 14759217211047901.

40. Cicirello, A. and F. Giunta, *Machine learning based optimization for interval uncertainty propagation.* Mechanical Systems and Signal Processing, 2022. **170**: p. 108619.

41. Yin, T., C.T. Ng, and A. Kotousov. *Thermal damage detection and monitoring of pristine graphene mortar materials using a cross-modulation vibro-acoustic technique*. in *ACAM10: 10th Australasian Congress on Applied Mechanics: 10th Australasian Congress on Applied Mechanics*. 2021. Engineers Australia.

42. Yin, T., et al., *Amplitude-Modulation Vibro-Acoustic Technique for Damage Evaluation.* Structural Health Monitoring, 2022: p. 14759217221106209.

43. Yin, T., C.-T. Ng, and A. Kotousov, *Damage detection of ultra-high-performance fibre-reinforced concrete using a harmonic wave modulation technique.* Construction and Building Materials, 2021. **313**: p. 125306.

44. Packo, P., et al., *Modeling and Numerical Simulations in Nonlinear Acoustics Used for Damage Detection*, in *Nonlinear Ultrasonic and Vibro-Acoustical Techniques for Nondestructive Evaluation*. 2019, Springer. p. 103-137.

45. Cantrell, J.H., *Fundamentals and applications of nonlinear ultrasonic nondestructive evaluation.* Ultrasonic Nondestructive Evaluation: Engineering and biological material characterization, 2004. **363**: p. 434.

46. *Australian Standard*, in *General purpose and blended cements*. 2010, Standards Australia International Ltd: Sydney, NSW 2001, Australia.

47. *Australian Standard*, in *Chemical admixtures for concrete, mortar and grout Part 1: Admixtures for concrete*. 2000, Standards Australia International Ltd: Sydney, NSW 2001, Australia.

48. Ho, V.D., et al., *Investigating the reinforcing mechanism and optimized dosage of pristine graphene for enhancing mechanical strengths of cementitious composites.* RSC Advances, 2020. **10**(70): p. 42777-42789.

49. *ASTM C215-19*, in *Standard Test Method for Fundamental Transverse, Longitudinal, and Torsional Resonant Frequencies of Concrete Specimens*. 2019, ASTM International.

50. Yang, H., et al., *A critical review on research progress of graphene/cement based composites.* Composites Part A: Applied Science and Manufacturing, 2017. **102**: p. 273-296.

Appendix A

Following the analysis of perturbation theory, which is based on the idea that the response of a weak nonlinear system can be seem as the linear response (*i.e.* the nonlinear terms in Eq. (1) are set to zero), and the nonlinear response with reducing significance. The reducing significance of responses can be indicated by writing,

$$u = \epsilon^0 u_1 + \epsilon^1 u_2 + \epsilon^2 u_3 \tag{5-A1}$$

where ϵ is a small parameter and its order can be seen as a tool to track the significance of terms. Insert Eq. (A1) into Eq. (1), then we will balance the order ϵ^0, ϵ^1, and ϵ^2 terms,

$$\epsilon^0 \frac{\partial^2 u_1}{\partial t^2} = \epsilon^0 c^2 \frac{\partial^2 u_1}{\partial x^2} \tag{5-A2}$$

$$\epsilon^1 \frac{\partial^2 u_2}{\partial t^2} = \epsilon^1 c^2 \frac{\partial^2 u_2}{\partial x^2} - \epsilon^1 c^2 \beta \frac{\partial u_1}{\partial x}\frac{\partial^2 u_1}{\partial x^2} \tag{5-A3}$$

$$\epsilon^2 \frac{\partial^2 u_3}{\partial t^2} = \epsilon^2 c^2 \frac{\partial^2 u_3}{\partial x^2} - \epsilon^2 c^2 \gamma \left(\frac{\partial u_1}{\partial x}\right)^2 \frac{\partial^2 u_1}{\partial x^2} - \epsilon^2 c^2 \beta \frac{\partial u_2}{\partial x}\frac{\partial^2 u_1}{\partial x^2} - \epsilon^2 c^2 \beta \frac{\partial u_1}{\partial x}\frac{\partial^2 u_2}{\partial x^2} \tag{5-A4}$$

Eq.(5-A2) is identical to the case where the system is linear (*i.e.* setting the nonlinear parameter β and γ to zero in Eq.(5-1)), which is corresponding to Eq.(5-3a). Meanwhile, Eq.(5-A3) and (5-A4) is consistent with Eq.(5-3b) and (5-3c), respectively.

Inserting Eq.(5-4) into Eq.(5-3b), and assume that $u_2 = xf(\tau)$, where $\tau = t - x/c$, and $f(\tau)$ is the function related to t and x. Then we will have,

$$\begin{aligned} -\frac{\beta}{c}\{&A_H\omega_H \sin(\omega_H\tau + \phi_H) + A_{L2}\omega_{L2}[1 + A_{L1}\cos(\omega_{L1}\tau + \phi_{L1})]\sin(\omega_{L2}\tau + \phi_{L2}) \\ &+ A_{L2}A_{L1}\omega_{L1}\cos(\omega_{L2}\tau + \phi_{L2})\sin(\omega_{L1}\tau + \phi_{L1})\}\{A_H\omega_H^2\cos(\omega_H\tau \\ &+ \phi_H) + A_{L2}\cos(\omega_{L2}\tau + \phi_{L2})[\omega_{L2}^2 + A_{L1}(\omega_{L2}^2 + \omega_{L1}^2)\cos(\omega_{L1}\tau \\ &+ \phi_{L1})] - 2A_{L2}A_{L1}\omega_{L2}\omega_{L1}\sin(\omega_{L2}\tau + \phi_{L2})\sin(\omega_{L1}\tau + \phi_{L1})\} \\ &+ 2cf'(\tau) \end{aligned} \tag{5-A5}$$

Solving Eq. (5-A5) to obtain the solution of $f(\tau)$, and then u_2 can be written as,

$$
\begin{aligned}
u_2 = x\{C_1 - \frac{\beta}{32c^2}[&4A_H^2\omega_H^2\cos(2\omega_H\tau + 2\phi_H) \\
&+ 2A_{L2}^2(2\omega_{L2}^2 + A_{L1}^2\omega_{L2}^2 - A_{L1}^2\omega_{L2}^2)\cos(2\omega_{L2}\tau + 2\phi_{L2}) \\
&- 8A_{L2}^2A_{L1}\omega_{L2}^2\cos(\omega_{L1}\tau + \phi_{L1}) \\
&+ 2A_{L2}^2A_{L1}^2(\omega_{L1}^2 - \omega_{L2}^2)\cos(2\omega_{L1}\tau + 2\phi_{L1}) \\
&- 8A_HA_{L2}\omega_H\omega_{L2}\cos(\omega_H\tau - \omega_{L2}\tau + \phi_H - \phi_{L2}) \\
&+ 8A_HA_{L2}\omega_H\omega_{L2}\cos(\omega_H\tau + \omega_{L2}\tau + \phi_H + \phi_{L2}) \\
&+ A_{L2}^2A_{L1}^2(\omega_{L2} - \omega_{L1})^2\cos(2\omega_{L2}\tau - 2\omega_{L1}\tau + 2\phi_{L2} - 2\phi_{L1}) \\
&+ A_{L2}^2A_{L2}^2(\omega_{L2} + \omega_{L1})^2\cos(2\omega_{L2}\tau + 2\omega_{L1}\tau + 2\phi_{L2} + 2\phi_{L1}) \\
&+ 4A_{L2}^2A_{L1}\omega_{L2}(\omega_{L2} - \omega_{L1})\cos(2\omega_{L2}\tau - \omega_{L1}\tau + 2\phi_{L2} - \phi_{L1}) \\
&+ 4A_{L2}^2A_{L1}\omega_{L2}(\omega_{L2} + \omega_{L1})\cos(2\omega_{L2}\tau + \omega_{L1}\tau + 2\phi_{L2} + \phi_{L1}) \\
+4A_HA_{L2}A_{L1}\omega_H&(\omega_{L2} + \omega_{L1})\cos(\omega_H\tau + \omega_{L2}\tau + \omega_{L1}\tau + \phi_H + \phi_{L2} + \phi_{L1}) \\
+4A_HA_{L2}A_{L1}\omega_H&(\omega_{L2} - \omega_{L1})\cos(\omega_H\tau + \omega_{L2}\tau - \omega_{L1}\tau + \phi_H + \phi_{L2} - \phi_{L1}) \\
-4A_HA_{L2}A_{L1}\omega_H&(\omega_{L2} - \omega_{L1})\cos(\omega_H\tau - \omega_{L2}\tau + \omega_{L1}\tau + \phi_H - \phi_{L2} + \phi_{L1}) \\
-4A_HA_{L2}A_{L1}\omega_H&(\omega_{L2} + \omega_{L1})\cos(\omega_H\tau - \omega_{L2}\tau - \omega_{L1}\tau + \phi_H - \phi_{L2} - \phi_{L1})]\}
\end{aligned}
\tag{5-A6}
$$

We follow the same steps, to substitute $u_1$and u_2 into Eq.(5-3c), and to assume $u_3 = xg(\tau)$, where $g(\tau)$ is the function of t and x. After omitting constant terms, higher order terms and LF sidebands ($nf_2 \pm nf_1$, where $n = 1,2,3$ ...), u_3 can be written in,

$$
\begin{aligned}
u_3 = x\{-\frac{\beta^2}{256c^2}[&16xA_H\omega_H^2\big(-A_H^2\omega_H^2 \\
&- A_{L1}^2(2\omega_{L2}^2 + A_{L1}^2\omega_{L2}^2 + A_{L1}^2\omega_{L1}^2)\big)\cos(\omega_H\tau + \phi_H) \\
+8cA_H\omega_H&\big(3A_H^2\omega_H^2 + 4A_{L2}^2(2\omega_{L2}^2 + A_{L1}^2\omega_{L2}^2 + A_{L1}^2\omega_{L1}^2)\big)\sin(\omega_H\tau + \phi_H) \\
-8xA_{L2}\omega_{L2}^2&(4A_H^2\omega_H^2 + A_{L2}^2(2\omega_{L2}^2 + 3A_{L1}^2\omega_{L2}^2 + A_{L1}^2\omega_{L1}^2)\cos(\omega_{L2}\tau + \phi_{L2}) \\
+4cA_{L2}\omega_{L2}&(16A_H^2\omega_H^2 + A_{L2}^2(6\omega_{L2}^2 + 13A_2^2\omega_{L2}^2 + 3A_2^2\omega_2^2)\sin(\omega_{L2}\tau + \phi_{L2}) \\
+16xA_H^3\omega_H^4&\cos(3\omega_H\tau + 3\phi_H) - \frac{40}{3}cA_H^3\omega_H^3\sin(3\omega_H\tau + 3\phi_H) \\
+8xA_{L2}^3\omega_{L2}^2&(2\omega_{L2}^2 + 3A_{L1}^2\omega_{L2}^2 - 3A_{L1}^2\omega_{L1}^2)\cos(3\omega_{L2}\tau + 3\phi_{L2}) \\
-\frac{20}{3}cA_{L2}^3\omega_{L2}&(2\omega_{L2}^2 + 3A_{L1}^2\omega_{L2}^2 - 3A_{L1}^2\omega_{L1}^2)\sin(3\omega_{L2}\tau + 3\phi_{L2}) \\
-32xA_HA_{L2}^2A_{L1}\omega_H\omega_{L2}^2&(\omega_H + \omega_{L1})\cos(\omega_H\tau + \omega_{L1}\tau + \phi_H + \phi_{L1}) \\
+80cA_HA_{L2}^2A_{L1}\omega_H\omega_{L2}^2&\sin(\omega_H\tau + \omega_{L1}\tau + \phi_H + \phi_{L1}) \\
-32xA_HA_{L2}^2A_{L1}\omega_H\omega_{L2}^2&(\omega_H - \omega_{L1})\cos(\omega_H\tau - \omega_{L1}\tau + \phi_H - \phi_{L1}) \\
+80cA_HA_{L2}^2A_{L1}\omega_H\omega_{L2}^2&\sin(\omega_H\tau - \omega_{L1}\tau + \phi_H - \phi_{L1})
\end{aligned}
\tag{5-A7}
$$

$$+8xA_H A_{L2}^2 \omega_H(\omega_H - 2\omega_{L2})(2\omega_{L2}^2 + A_{L1}^2\omega_{L2}^2 - A_{L1}^2\omega_{L1}^2)\cos(\omega_H\tau - 2\omega_{L2}\tau + \phi_H - 2\phi_{L2})$$

$$-20cA_H A_{L2}^2 \omega_H(2\omega_{L2}^2 + A_{L1}^2\omega_{L2}^2 - A_{L1}^2\omega_{L1}^2)\sin(\omega_H\tau - 2\omega_{L2}\tau + \phi_H - 2\phi_{L2})$$

$$+8xA_H A_{L2}^2 \omega_H(\omega_H + 2\omega_{L2})(2\omega_{L2}^2 + A_{L1}^2\omega_{L2}^2 - A_{L1}^2\omega_{L1}^2)\cos(\omega_H\tau + 2\omega_{L2}\tau + \phi_H + 2\phi_{L2})$$

$$-20cA_H A_{L2}^2 \omega_H(2\omega_{L2}^2 + A_{L1}^2\omega_{L2}^2 - A_{L1}^2\omega_2^2)\sin(\omega_H\tau + 2\omega_{L2}\tau + \phi_H + 2\phi_{L2})$$

$$-8xA_H A_{L2}^2 A_{L1}^2 \omega_H(\omega_H + 2\omega_{L1})(\omega_{L2}^2 - \omega_{L1}^2)\cos(\omega_H\tau + 2\omega_{L1}\tau + \phi_H + 2\phi_{L1})$$

$$+20cA_H A_{L2}^2 A_{L1}^2 \omega_H(\omega_{L2}^2 - \omega_{L1}^2)\sin(\omega_H\tau + 2\omega_{L1}\tau + \phi_H + 2\phi_{L1})$$

$$-8xA_H A_{L2}^2 A_{L1}^2 \omega_H(\omega_H - 2\omega_{L1})(\omega_{L2}^2 - \omega_{L1}^2)\cos(\omega_H\tau - 2\omega_{L1}\tau + \phi_H - 2\phi_{L1})$$

$$+20cA_H A_{L2}^2 A_{L1}^2 \omega_H(\omega_{L2}^2 - \omega_{L1}^2)\sin(\omega_H\tau - 2\omega_{L1}\tau + \phi_H - 2\phi_{L1})$$

$$+16xA_H A_{L2}^2 A_{L1}\omega_H\omega_{L2}(\omega_{L2} + \omega_{L1})(\omega_H + 2\omega_{L2} + \omega_{L1})\cos(\omega_H\tau + 2\omega_{L2}\tau + \omega_{L1}\tau + \phi_H + 2\phi_{L2} + \phi_{L1})$$

$$-40cA_H A_{L2}^2 A_{L1}\omega_H\omega_{L2}(\omega_{L2} + \omega_{L1})\sin(\omega_H\tau + 2\omega_{L2}\tau + \omega_{L1}\tau + \phi_H + 2\phi_{L2} + \phi_{L1})$$

$$+16xA_H A_{L2}^2 A_{L1}\omega_H\omega_{L2}(\omega_{L2} - \omega_{L1})(\omega_H + 2\omega_{L2} - \omega_{L1})\cos(\omega_H\tau + 2\omega_{L2}\tau - \omega_{L1}\tau + \phi_H + 2\phi_{L2} - \phi_{L1})$$

$$-40cA_H A_{L2}^2 A_{L1}\omega_H\omega_{L2}(\omega_{L2} - \omega_{L1})\sin(\omega_H\tau + 2\omega_{L2}\tau - \omega_{L1}\tau + \phi_H + 2\phi_{L2} - \phi_{L1})$$

$$+16xA_H A_{L2}^2 A_{L1}\omega_H\omega_{L2}(\omega_{L2} - \omega_{L1})(\omega_H - 2\omega_{L2} + \omega_{L1})\cos(\omega_H\tau - 2\omega_{L2}\tau + \omega_{L1}\tau + \phi_H - 2\phi_{L2} + \phi_{L1})$$

$$-40cA_H A_{L2}^2 A_{L1}\omega_H\omega_{L2}(\omega_{L2} - \omega_{L1})\sin(\omega_H\tau - 2\omega_{L2}\tau + \omega_{L1}\tau + \phi_H - 2\phi_{L2} + \phi_{L1})$$

$$+16xA_H A_{L2}^2 A_{L1}\omega_H\omega_{L2}(\omega_{L2} + \omega_{L1})(\omega_H - 2\omega_{L2} - \omega_{L1})\cos(\omega_H\tau - 2\omega_{L2}\tau - \omega_{L1}\tau + \phi_H - 2\phi_{L2} - \phi_{L1})$$

$$-40cA_H A_{L2}^2 A_{L1}\omega_H\omega_{L2}(\omega_{L2} + \omega_{L1})\sin(\omega_H\tau - 2\omega_{L2}\tau - \omega_{L1}\tau + \phi_H - 2\phi_{L2} - \phi_{L1})$$

$$+4xA_H A_{L2}^2 A_{L1}^2 \omega_H(\omega_{L2} + \omega_{L1})^2(\omega_H + 2\omega_{L2} + 2\omega_{L1})\cos(\omega_H\tau + 2\omega_{L2}\tau + 2\omega_{L1}\tau + \phi_H + 2\phi_{L2} + 2\phi_{L1})$$

$$-10cA_0 A_{L2}^2 A_{L1}^2 \omega_H(\omega_{L2} + \omega_{L1})^2\sin(\omega_H\tau + 2\omega_{L2}\tau + 2\omega_{L1}\tau + \phi_H + 2\phi_{L2} + 2\phi_{L1})$$

$$+4xA_H A_{L2}^2 A_{L1}^2 \omega_H(\omega_{L2} - \omega_2)^2(\omega_H + 2\omega_{L2} - 2\omega_{L1})\cos(\omega_H\tau + 2\omega_{L2}\tau - 2\omega_{L1}\tau + \phi_H + 2\phi_{L2} - 2\phi_{L1})$$

$$
\begin{aligned}
&-10cA_H A_{L2}^2 A_{L1}^2 \omega_H (\omega_{L2}-\omega_{L1})^2 \sin(\omega_H\tau + 2\omega_{L2}\tau - 2\omega_{L1}\tau + \phi_H + 2\phi_{L2} \\
&\qquad - 2\phi_{L1}) \\
&+4xA_H A_{L2}^2 A_{L1}^2 \omega_H (\omega_{L2}-\omega_{L1})^2 (\omega_H - 2\omega_{L2} + 2\omega_{L1}) \cos(\omega_H\tau - 2\omega_{L2}\tau + 2\omega_{L1}\tau \\
&\qquad + \phi_H - 2\phi_{L2} + 2\phi_{L1}) \\
&-10cA_H A_{L2}^2 A_{L1}^2 \omega_H (\omega_{L2}-\omega_{L1})^2 \sin(\omega_H\tau - 2\omega_{L2}\tau + 2\omega_{L1}\tau + \phi_H - 2\phi_{L2} \\
&\qquad + 2\phi_{L1}) \\
&+4xA_H A_{L2}^2 A_{L1}^2 \omega_H (\omega_{L2}+\omega_{L1})^2 (\omega_H - 2\omega_{L2} - 2\omega_{L1}) \cos(\omega_H\tau - 2\omega_{L2}\tau - 2\omega_{L1}\tau \\
&\qquad + \phi_H - 2\phi_{L2} - 2\phi_{L1}) \\
&-10cA_H A_{L2}^2 A_{L1}^2 \omega_H (\omega_{L2}+\omega_{L1})^2 \sin(\omega_H\tau - 2\omega_{L2}\tau - 2\omega_{L1}\tau + \phi_H - 2\phi_{L2} \\
&\qquad - 2\phi_{L1})]\}
\end{aligned}
$$

The purpose of derivation is to figure out the relationship between sidebands and fundamental signals, therefore, sidebands around f_H in Eq.(5-A7) are left in the following derivations and other components are omitted. According to the principle that $a\sin\theta + b\cos\theta = \sqrt{(a^2+b^2)}\sin(\theta+\varphi)$, where $\varphi = \tan^{-1}(b/a)$, the Eq.(5-A7) can be transferred into,

$$
\begin{aligned}
&\frac{1}{64}\sqrt{\frac{A_H^2 A_{L2}^4 \omega_H^2 x^2 \beta^4 [25c^2 + 4x^2(\omega_H + 2\omega_{L2})^2][(2+A_{L1}^2)\omega_{L2}^2 - A_{L1}^2\omega_{L1}^2]^2}{c^8}}\sin[(\omega_H \\
&\qquad + 2\omega_{L2})\tau + (\phi_H + 2\phi_{L2}) + \varphi_{(H+2L2)}] + \\
&\frac{1}{64}\sqrt{\frac{A_H^2 A_{L2}^4 \omega_H^2 x^2 \beta^4 [25c^2 + 4x^2(\omega_H - 2\omega_{L2})^2][(2+A_{L1}^2)\omega_{L2}^2 - A_{L1}^2\omega_{L1}^2]^2}{c^8}}\sin[(\omega_H \\
&\qquad + 2\omega_{L2})\tau + (\phi_H + 2\phi_{L2}) + \varphi_{(H-2L2)}] + \\
&\frac{1}{16}\sqrt{\frac{A_H^2 A_{L2}^4 A_{L1}^2 \omega_H^2 \omega_{L2}^4 x^2 \beta^4 [25c^2 + 4x^2(\omega_H + \omega_{L1})^2]}{c^8}}\sin[(\omega_H + \omega_{L1})\tau + (\phi_H \\
&\qquad + \phi_{L1}) + \varphi_{(H+2L1)}] + \\
&\frac{1}{16}\sqrt{\frac{A_H^2 A_{L2}^4 A_{L1}^2 \omega_H^2 \omega_{L2}^4 x^2 \beta^4 [25c^2 + 4x^2(\omega_H - \omega_{L1})^2]}{c^8}}\sin[(\omega_H - \omega_{L1})\tau + (\phi_H \\
&\qquad - \phi_{L1}) + \varphi_{(H-2L1)}] +
\end{aligned}
\tag{5-A8}
$$

$$\frac{1}{64}\sqrt{\frac{A_H^2A_{L2}^4A_{L1}^2\omega_H^2(\omega_{L2}^2-\omega_{L1}^2)^2x^2\beta^4[25c^2+4x^2(\omega_H+2\omega_{L2})^2]}{c^8}}\sin[(\omega_H+2\omega_{L1})\tau$$
$$+(\phi_H+2\phi_{L1})+\varphi_{(H+2L1)}]+$$
$$\frac{1}{64}\sqrt{\frac{A_H^2A_{L2}^4A_2^2\omega_H^2(\omega_{L2}^2-\omega_{L1}^2)^2x^2\beta^4[25c^2+4x^2(\omega_H-2\omega_{L2})^2]}{c^8}}\sin[(\omega_H-2\omega_2)\tau$$
$$+(\phi_H-2\phi_{L1})+\varphi_{(H-2L1)}]+$$
$$\frac{1}{32}\sqrt{\frac{A_H^2A_{L2}^4A_{L1}^2\omega_H^2\omega_{L2}^2(\omega_{L2}+\omega_{L1})^2x^2\beta^4[25c^2+4x^2(\omega_H+2\omega_{L2}+\omega_{L1})^2]}{c^8}}\sin[(\omega_H$$
$$+2\omega_{L2}+\omega_{L1})\tau+(\phi_H+2\phi_{L2}+\phi_{L1})+\varphi_{(H+2L2+L1)}]+$$
$$\frac{1}{32}\sqrt{\frac{A_H^2A_{L2}^4A_{L1}^2\omega_H^2\omega_{L2}^2(\omega_{L2}-\omega_{L1})^2x^2\beta^4[25c^2+4x^2(\omega_H+2\omega_{L2}-\omega_{L1})^2]}{c^8}}\sin[(\omega_H$$
$$+2\omega_{L2}-\omega_{L1})\tau+(\phi_H+2\phi_{L2}-\phi_{L1})+\varphi_{(H+2L2-L1)}]+$$
$$\frac{1}{32}\sqrt{\frac{A_H^2A_{L2}^4A_{L1}^2\omega_H^2\omega_{L2}^2(\omega_{L2}-\omega_{L1})^2x^2\beta^4[25c^2+4x^2(\omega_H-2\omega_{L2}+\omega_{L1})^2]}{c^8}}\sin[(\omega_H$$
$$-2\omega_{L2}+\omega_{L1})\tau+(\phi_H-2\phi_{L2}+\phi_{L1})+\varphi_{(H-2L2+L1)}]+$$
$$\frac{1}{32}\sqrt{\frac{A_H^2A_{L2}^4A_{L1}^2\omega_H^2\omega_{L2}^2(\omega_{L2}+\omega_{L1})^2x^2\beta^4[25c^2+4x^2(\omega_H-2\omega_{L2}-\omega_{L1})^2]}{c^8}}\sin[(\omega_H$$
$$-2\omega_{L2}-\omega_{L1})\tau+(\phi_H-2\phi_{L2}-\phi_{L1})+\varphi_{(H-2L2-L1)}]+$$
$$\frac{1}{128}\sqrt{\frac{A_H^2A_{L2}^4A_{L1}^2\omega_H^2(\omega_{L2}+\omega_{L1})^4x^2\beta^4[25c^2+4x^2(\omega_H+2\omega_{L2}+2\omega_{L1})^2]}{c^8}}\sin[(\omega_H$$
$$+2\omega_{L2}+2\omega_{L1})\tau+(\phi_H+2\phi_{L2}+2\phi_{L1})+\varphi_{(H+2L2+2L1)}]+$$
$$\frac{1}{128}\sqrt{\frac{A_H^2A_{L2}^4A_{L1}^2\omega_H^2(\omega_{L2}-\omega_{L1})^4x^2\beta^4[25c^2+4x^2(\omega_H+2\omega_{L2}-2\omega_{L1})^2]}{c^8}}\sin[(\omega_H$$
$$+2\omega_{L2}-2\omega_{L1})\tau+(\phi_H+2\phi_{L2}-2\phi_{L1})+\varphi_{(H+2L2-2L1)}]+$$
$$\frac{1}{128}\sqrt{\frac{A_H^2A_{L2}^4A_{L1}^2\omega_H^2(\omega_{L2}-\omega_{L1})^4x^2\beta^4[25c^2+4x^2(\omega_H-2\omega_{L2}+2\omega_{L1})^2]}{c^8}}\sin[(\omega_H$$
$$-2\omega_{L2}+2\omega_{L1})\tau+(\phi_H-2\phi_{L2}+2\phi_{L1})+\varphi_{(H-2L2+2L1)}]+$$

$$\frac{1}{128}\sqrt{\frac{A_H^2 A_{L2}^4 A_{L1}^2 \omega_H^2 (\omega_{L2}+\omega_{L1})^4 x^2 \beta^4 [25c^2 + 4x^2(\omega_H - 2\omega_{L2} - 2\omega_{L1})^2]}{c^8}} \sin[(\omega_H - 2\omega_{L2} - 2\omega_{L1})\tau + (\phi_H - 2\phi_{L2} - 2\phi_{L1}) + \varphi_{(H-2L2-2L1)}]$$

where φ is the phase components, and its subscript indicates the sidebands components it belongs to. The details of φ are listed below,

$$\begin{aligned}
\varphi_{(H+2L2)} &= \tan^{-1}[-\frac{2x(\omega_H + 2\omega_{L2})}{5c}] \\
\varphi_{(H-2L2)} &= \tan^{-1}[-\frac{2x(\omega_H - 2\omega_{L2})}{5c}] \\
\varphi_{(H+L1)} &= \tan^{-1}[-\frac{2x(\omega_H + \omega_{L1})}{5c}] \\
\varphi_{(H-L1)} &= \tan^{-1}[-\frac{2x(\omega_H - \omega_{L1})}{5c}] \\
\varphi_{(H+2L1)} &= \tan^{-1}[-\frac{2x(\omega_H + 2\omega_{L1})}{5c}] \\
\varphi_{(H-2L1)} &= \tan^{-1}[-\frac{2x(\omega_H - 2\omega_{L1})}{5c}] \\
\varphi_{(H+2L2+L1)} &= \tan^{-1}[-\frac{2x(\omega_H + 2\omega_{L2} + \omega_{L1})}{5c}] \\
\varphi_{(H+2L2-L1)} &= \tan^{-1}[-\frac{2x(\omega_H + 2\omega_{L2} - \omega_{L1})}{5c}] \\
\varphi_{(H-2L2+L1)} &= \tan^{-1}[-\frac{2x(\omega_H - 2\omega_{L2} + \omega_{L1})}{5c}] \\
\varphi_{(H-2L2-L1)} &= \tan^{-1}[-\frac{2x(\omega_H - 2\omega_{L2} - \omega_{L1})}{5c}] \\
\varphi_{(H+2L2+2L1)} &= \tan^{-1}[-\frac{2x(\omega_H + 2\omega_{L2} + 2\omega_{L1})}{5c}] \\
\varphi_{(H+2L2-2L1)} &= \tan^{-1}[-\frac{2x(\omega_H + 2\omega_{L2} - 2\omega_{L1})}{5c}] \\
\varphi_{(H-2L2+2L1)} &= \tan^{-1}[-\frac{2x(\omega_H - 2\omega_{L2} + 2\omega_{L1})}{5c}] \\
\varphi_{(H-2L2-2L1)} &= \tan^{-1}[-\frac{2x(\omega_H - 2\omega_{L2} - 2\omega_{L1})}{5c}]
\end{aligned} \tag{5-A9}$$

Combing the sidebands components of u_2 and u_3, then it can be written as,

$-\frac{A_H A_{L2}}{4c^2} x\beta\omega_H\omega_{L2}\cos(\omega_H\tau+\omega_{L2}\tau+\phi_H+\phi_{L2})$ $+\frac{A_H A_{L2}}{4c^2} x\beta\omega_H\omega_{L2}\cos(\omega_H\tau-\omega_{L2}\tau+\phi_H-\phi_{L2})$	Sidebands of $(\omega_H \pm \omega_{L2}$
$+\frac{A_H A_{L1} A_{L2}^2}{16c^2} x\beta^2\omega_H\omega_{L2}^2\,\xi_{(H+L1)}\sin\big[(\omega_H+\omega_{L1})\tau+(\phi_H+\phi_{L1})+\varphi_{(H+L1)}\big]$ $+\frac{A_H A_{L1} A_{L2}^2}{16c^2} x\beta^2\omega_H\omega_{L2}^2\,\xi_{(H-L1)}\sin\big[(\omega_H-\omega_{L1})\tau+(\phi_H-\phi_{L1})+\varphi_{(H-L1)}\big]$	Sidebands of $(\omega_H \pm \omega_{L1}$
$+\frac{A_H A_{L2}^2}{64c^2} x\beta^2\omega_H\lvert 2\omega_{L2}^2+A_{L1}^2(\omega_{L2}^2-\omega_{L1}^2)\rvert\,\xi_{(H+2L2)}\sin[(\omega_H+2\omega_{L2})\tau+(\phi_H+2\phi_{L2})+\varphi_{(\omega_H+2\omega_{L2})}]$ $+\frac{A_H A_{L2}^2}{64c^2} x\beta^2\omega_H\lvert 2\omega_{L2}^2+A_{L1}^2(\omega_{L2}^2-\omega_{L1}^2)\rvert\,\xi_{(H-2L2)}\sin[(\omega_H-2\omega_{L2})\tau+(\phi_H-2\phi_{L2})+\varphi_{(\omega_H-2\omega_{L2})}]$	Sidebands of $(\omega_H \pm 2\omega_{L2})$
$+\frac{A_H A_{L1}^2 A_{L2}^2}{64c^2} x\beta^2\omega_H(\omega_{L2}^2-\omega_{L1}^2)\,\xi_{(H+2L1)}\sin[(\omega_H+2\omega_{L1})\tau+(\phi_H+2\phi_{L1})+\varphi_{(H+2L1)}]$ $+\frac{A_H A_{L1}^2 A_{L2}^2}{64c^2} x\beta^2\omega_H(\omega_{L2}^2-\omega_{L1}^2)\,\xi_{(H-2L1)}\sin[(\omega_H-2\omega_{L1})\tau+(\phi_H-2\phi_{L1})+\varphi_{(H-2L1)}]$	Sidebands of $(\omega_H \pm 2\omega_{L1})$
$-\frac{A_H A_{L1} A_{L2}}{8c^2} x\beta\omega_H(\omega_{L2}+\omega_{L1})\cos[(\omega_H+\omega_{L2}+\omega_{L1})\tau+(\phi_H+\phi_{L2}+\phi_{L1})]$ $-\frac{A_H A_{L1} A_{L2}}{8c^2} x\beta\omega_H(\omega_{L2}-\omega_{L1})\cos[(\omega_H+\omega_{L2}+\omega_{L1})\tau+(\phi_H+\phi_{L2}+\phi_{L1})]$	Sidebands of $(\omega_H \pm \omega_{L2} \pm \omega_{L1})$

(A10)

$+\frac{A_H A_{L1} A_{L2}}{8c^2} x\beta\omega_H(\omega_{L2} - \omega_{L1})\cos[(\omega_H - \omega_{L2} + \omega_{L1})\tau + (\phi_H - \phi_{L2} + \phi_{L1})]$	
$+\frac{A_H A_{L1} A_{L2}}{8c^2} x\beta\omega_H(\omega_{L2} + \omega_{L1})\cos[(\omega_H - \omega_{L2} - \omega_{L1})\tau + (\phi_H - \phi_{L2} - \phi_{L1})]$	
$+\frac{A_H A_{L1} A_{L2}^2}{32c^2} x\beta^2\omega_H\omega_{L2}\lvert\omega_{L1} + \omega_{L2}\rvert\,\xi_{(H+2L2+L1)}\sin[(\omega_H + 2\omega_{L2} + \omega_{L1})\tau + (\phi_H + 2\phi_{L2} + \phi_{L1}) + \varphi_{(H+2L2+L1)}]$	
$+\frac{A_H A_{L1} A_{L2}^2}{32c^2} x\beta^2\omega_H\omega_{L2}\lvert\omega_{L1} - \omega_{L2}\rvert\,\xi_{(H+2L2-L1)}\sin[(\omega_H + 2\omega_{L2} - \omega_{L1})\tau + (\phi_H + 2\phi_{L2} - \phi_{L1}) + \varphi_{(H+2L2-L1)}]$	Sidebands of $(\omega_H \pm 2\omega_{L2} \pm \omega_{L1})$
$+\frac{A_H A_{L1} A_{L2}^2}{32c^2} x\beta^2\omega_H\omega_{L2}\lvert\omega_{L1} - \omega_{L2}\rvert\,\xi_{H-2L2+L1}\sin[(\omega_H - 2\omega_{L2} + \omega_{L1})\tau + (\phi_H - 2\phi_{L2} + \phi_{L1}) + \varphi_{(H-2L2+L1)}]$	
$+\frac{A_H A_{L1} A_{L2}^2}{32c^2} x\beta^2\omega_H\omega_{L2}\lvert\omega_{L1} + \omega_{L2}\rvert\,\xi_{H-2L2+L1}\sin[(\omega_H - 2\omega_{L2} - \omega_{L1})\tau + (\phi_H - 2\phi_{L2} - \phi_{L1}) + \varphi_{(H-2L2-L1)}]$	
$+\frac{A_H A_{L1}^2 A_{L2}^2}{128c^2} x\beta^2\omega_H\omega_{L2}(\omega_{L1} + \omega_{L2})^2\,\xi_{H+2L2+2L1}\sin[(\omega_H + 2\omega_{L2} + 2\omega_{L1})\tau + (\phi_H + 2\phi_{L2} + 2\phi_{L1}) + \varphi_{(H+2L2+2L1)}]$	Sidebands of $(\omega_H \pm 2\omega_{L2} \pm 2\omega_{L1})$
$+\frac{A_H A_{L1}^2 A_{L2}^2}{128c^2} x\beta^2\omega_H\omega_{L2}(\omega_{L1} - \omega_{L2})^2\,\xi_{H+2L2-2L1}\sin[(\omega_H + 2\omega_{L2} - 2\omega_{L1})\tau + (\phi_H + 2\phi_{L2} - 2\phi_{L1}) + \varphi_{(H+2L2-2L1)}]$	

$$+\frac{A_H A_{L1}^2 A_{L2}^2}{128c^2} x\beta^2 \omega_H \omega_{L2}(\omega_{L1} - \omega_{L2})^2 \xi_{H-2L2+2L1} \sin[(\omega_H - 2\omega_{L2} + 2\omega_{L1})\tau + (\phi_H - 2\phi_{L2} + 2\phi_{L1}) + \varphi_{(H-2L2+2L1)}]\}$$

$$+\frac{A_H A_{L1}^2 A_{L2}^2}{128c^2} x\beta^2 \omega_H \omega_{L2}(\omega_{L1} + \omega_{L2})^2 \xi_{H-2L2-2L1} \sin[(\omega_H - 2\omega_{L2} - 2\omega_{L1})\tau + (\phi_H - 2\phi_{L2} - 2\phi_{L1}) + \varphi_{(H-2L2-2L1)}]\}$$

where ξ is the variable, and its subscript is the sideband order. The details of ξ are as follow.

$$\xi_{(H+L1)} = \sqrt{\frac{25c^2 + 4x^2(\omega_H + \omega_{L1})^2}{c^2}}$$

$$\xi_{(H-L1)} = \sqrt{\frac{25c^2 + 4x^2(\omega_H - \omega_{L1})^2}{c^2}}$$

$$\xi_{(H+2L2)} = \sqrt{\frac{25c^2 + 4x^2(\omega_H + 2\omega_{L2})^2}{c^2}}$$

$$\xi_{(H-2L2)} = \sqrt{\frac{25c^2 + 4x^2(\omega_H - 2\omega_{L2})^2}{c^2}}$$

$$\xi_{(H+2L1)} = \sqrt{\frac{25c^2 + 4x^2(\omega_H + 2\omega_{L1})^2}{c^2}} \quad \text{(5-A11)}$$

$$\xi_{(H-2L1)} = \sqrt{\frac{25c^2 + 4x^2(\omega_H - 2\omega_{L1})^2}{c^2}}$$

$$\xi_{(H+2L2+L1)} = \sqrt{\frac{25c^2 + 4x^2(\omega_H + 2\omega_{L2} + \omega_{L1})^2}{c^2}}$$

$$\xi_{(H+2L2-L1)} = \sqrt{\frac{25c^2 + 4x^2(\omega_H + 2\omega_{L2} - \omega_{L1})^2}{c^2}}$$

$$\xi_{(H-2L2+L1)} = \sqrt{\frac{25c^2 + 4x^2(\omega_H - 2\omega_{L2} + \omega_{L1})^2}{c^2}}$$

$$\xi_{(H-2L2-L1)} = \sqrt{\frac{25c^2 + 4x^2(\omega_H - 2\omega_{L2} - \omega_{L1})^2}{c^2}}$$

$$\xi_{(H+2L2+2L1)} = \sqrt{\frac{25c^2 + 4x^2(\omega_H + 2\omega_{L2} + 2\omega_{L1})^2}{c^2}}$$

$$\xi_{(H+2L2-2L1)} = \sqrt{\frac{25c^2 + 4x^2(\omega_H + 2\omega_{L2} - 2\omega_{L1})^2}{c^2}}$$

$$\xi_{(H-2L2+2L1)} = \sqrt{\frac{25c^2 + 4x^2(\omega_H - 2\omega_{L2} + 2\omega_{L1})^2}{c^2}}$$

$$\xi_{(H-2L2-2L1)} = \sqrt{\frac{25c^2 + 4x^2(\omega_H - 2\omega_{L2} - 2\omega_{L1})^2}{c^2}}$$

Chapter 6 Conclusions and Works in Future

1. Conclusions

In this thesis, theoretical and experimental investigations on improving vibro-acoustic techniques for damage detection, particularly on early-damage detection of cement-based materials, have been carried out. The studies in the literature review reported that linear NDT and SHM techniques are limited to detecting damage that has reached a macro-scale but are not capable of evaluating early damage below that size. The vibro-acoustic technique is a promising NDT and SHM technique, which utilizes a low-frequency excitation and a high-frequency signal. When the monitored structure is not ideal, nonlinear phenomena, sidebands, can be observed from the frequency domain of the measured signals. Furthermore, the number and amplitude of sidebands can be used to assess the damages quantitatively. Vibro-acoustic techniques have two major approaches: impact-modulation (IM) and vibro-modulation (VM) methods. In the IM method, the monitoring structure is struck with an impactor, and the resonant vibration is used as the source of low-frequency signal, while VM method utilizes an electro-mechanical driving unit to emit the low-frequency signal. However, it is difficult to identify sidebands using IM method because the resonant frequency is not isolated, which causes the sidebands to interact with each other. In addition, IM method is easy to be affected by environmental noises. VM method utilizing a mechanical driving unit can provide strong and stable low-frequency excitation. Nevertheless, the frequency of pump wave should be carefully selected. When the frequency of pump wave is relatively low, it makes significant burdens to the mechanical driving unit, such as the electromagnetic shaker, particularly for long-term SHM. While the frequency of pump wave is relatively higher, the intervals between sidebands are large, resulting in sidebands distributed evenly in a large frequency range. However, the receiving instrument, such as transducers or PZT, is narrow-band. Hence, it is

easy to omit the sidebands far away from the central frequency of the receiving instrument due to their instrumental limitation. Thus, there is a powerful incentive to improve the vibro-acoustic technique, and the works presented in this thesis attempt to address the critical issues in the existing vibro-acoustic techniques, and the key outcomes are as follows.

i) A robust procedure of amplitude-modulated vibro-acoustic technique is developed. The amplitude-modulated pump wave is generated by combining an ultra-low-frequency f_{L1} and low-frequency f_{L2} continuous signal. This amplitude-modulated pump wave was successfully used to achieve the effect that the mechanical driving unit is emitting a signal at f_{L2} while f_{L1} also can be transmitted to reduce the burden on the mechanical driving unit. It can solve the problem that the ultra-low single-frequency pump wave puts a larger burden on the emitting unit, which is beneficial for long-term SHM. In Chapter 4, the studies of energy consumption between conventional and amplitude-modulated vibro-acoustic techniques were conducted. The results showed that the proposed amplitude-modulated vibro-acoustic technique uses only around half the energy of the conventional vibro-acoustic technique.

ii) Different amplitude-modulated methods were proposed and investigated, including pure amplitude-modulated (PAM), suppressive amplitude-modulated (SAM), and transmitted amplitude-modulated (TAM) methods. Comprehensive experiments were conducted to compare the conventional, PAM, SAM, and TAM vibro-acoustic techniques from the aspects of the energy-consumption, feasibility, and sensitivity.

iii) A continuous model for waves of the proposed amplitude-modulated vibro-acoustic techniques propagating in homogeneous and isotropic elastic material was established. Furthermore, a new third-order solution was derived, which includes higher-order sidebands generated by intrinsic and acquired nonlinearities. In

addition, the nonlinear parameters related to the sidebands and fundamental waves were defined to describe damages caused by material nonlinearity.

iv) A non-continuous model for waves of the proposed amplitude-modulated vibro-acoustic techniques propagating through contacting rough surfaces was developed, while the nonlinear parameter based on the non-continuous model was established to characterize damages caused by contact nonlinearity.

v) The proposed amplitude-modulated vibro-acoustic technique, including PAM, SAM, and TAM methods, were applied to evaluate different types of damages, e.g., bending and thermal damages, in various cement-based materials, e.g., UHP-FRC and pristine graphene mortar. The accuracy, feasibility, and sensitivity of the proposed approaches were demonstrated.

2. Recommendations for future work

The work conducted in this thesis aims at developing the vibro-acoustic technique for damage characterization on cement-based materials. By applying the amplitude-modulated pump wave, the proposed amplitude-modulated vibro-acoustic technique has lower power consumption, versatility, and high sensitivity compared to the conventional vibro-acoustic technique, which was verified by theoretical and experimental studies. For further investigations in this research area, recommended research directions are as follows.

i) The amplitude-modulated vibro-acoustic technique proposed in this thesis utilizes the bulk amplitude-modulated low-frequency pump wave and high-frequency probe wave, which are emitted and received by the contact transducers. Many NDT methods are commercially available for damage detection and evaluation, but they are not well-suited for SHM due to integration and cost issues. One of the development trends of SHM is to scan the entire inspected areas but not in time-consuming or limited access

to hard-to-access areas. Therefore, the non-contact amplitude-modulated vibro-acoustic techniques are potential to be investigated. One of the potential methods is to utilize the vibration of structures (e.g., vibration due to vehicle running or human action) as the source of LF excitation, and air-couple transducer to emit HF wave and to receive the signal.

ii) The guided wave is a mechanical stress wave that propagates along the structure, guided by its boundaries. They propagate at high speed and can be transmitted from a remote and accessible transducer location across the inspection area. Therefore, to take advantage of the guided wave, the vibro-acoustic technique can combine the guided wave with bulk wave excitation, in which the bulk wave excitation can afford an intensive displacement field to perturb the defects and cracks, while the guided wave can quickly scan the defects and cracks.

iii) Previous theoretical works, including establishing the nonlinear parameter based on material nonlinearity and contact nonlinearity, were both based on one-dimensional theories. In the current work, the amplitude-modulated low-frequency pump wave and high-frequency probing wave were both bulk waves. The one-dimensional theory of longitudinal wave motion, which denotes the longitudinal displacement of an infinitesimal element of a solid in the propagation direction, can describe the interactions between pump wave and probing wave, hence, establishing the nonlinear parameters. However, as mentioned above, the guided wave is one of the alternative trends. Therefore, two-dimensional or three-dimensional theory should be considered, in which waves propagate in two or three spatial directions. Therefore, the theoretical work can be expanded from one-dimensional to two-dimensional to establish the nonlinear parameters suitable for the vibro-acoustic technique combined with guided waves.